

# Design of a Very High Frequency dc-dc Boost Converter

by

Anthony Sagneri

B.S., Rensselaer Polytechnic Institute (1999)

Submitted to the Department of Electrical Engineering and Computer  
Science

in partial fulfillment of the requirements for the degree of

Master of Science

at the

MASSACHUSETTS INSTITUTE OF TECHNOLOGY

February 2007

© Massachusetts Institute of Technology, MMVII. All rights reserved.

Author \_\_\_\_\_  
Department of Electrical Engineering and Computer Science  
February 2, 2007

Certified by \_\_\_\_\_  
David J. Perreault  
Associate Professor of Electrical Engineering  
Thesis Supervisor

Accepted by \_\_\_\_\_  
Arthur C. Smith  
Chairman, Department Committee on Graduate Students



# Design of a Very High Frequency dc-dc Boost Converter

by  
Anthony Sagneri

Submitted to the Department of Electrical Engineering and Computer Science  
on February 2, 2007, in partial fulfillment of the  
requirements for the degree of  
Master of Science

## Abstract

Passive component volume is a perennial concern in power conversion. With new circuit architectures operating at extreme high frequencies it becomes possible to miniaturize the passive components needed for a power converter, and to achieve dramatic improvements in converter transient performance. This thesis focuses on the development of a Very High Frequency (VHF, 30 - 300 MHz) dc-dc boost converter using a MOSFET fabricated from a typical power process.

Modeling and design studies reveal the possibility of building VHF dc-dc converters operable over the full automotive input voltage range (8 - 18 V) with transistors in a 50 V power process, through use of newly-developed resonant circuit topologies designed to minimize transistor voltage stress. Based on this, a study of the design of automotive boost converters was undertaken (e.g., for LED headlamp drivers at output voltages in the range of 22 - 33 V.)

Two VHF boost converter prototypes using a  $\Phi_2$  resonant boost topology were developed. The first design used an off the shelf RF power MOSFET, while the second uses a MOSFET fabricated in a BCD process with no special modifications. Soft switching and soft gating of the devices are employed to achieve efficient operation at a switching frequencies of 75 MHz in the first case and 50 MHz in the latter.

In the 75 MHz case, efficiency ranges to 82%. The 50 MHz converter, has efficiencies in the high 70% range. Of note is low energy storage requirement of this topology. In the case of the 50 MHz converter, in particular, the largest inductor is 56 nH. Finally, closed-loop control is implemented and an evaluation of the transient characteristics reveals excellent performance.

Thesis Supervisor: David J. Perreault  
Title: Associate Professor of Electrical Engineering



# Acknowledgements

---

My thanks are due to the National Science Foundation, National Semiconductor, and the MIT EECS department for sponsorship. To Prof. Dave Perreault, my research advisor, and tacit instructor in all things power electronics, who somehow always seems to stay grounded. To Juan Rivas, also a tremendous source of knowledge, and emissary of laboratory shenanigans along with Jackie Hu and Grace who help to keep the atmosphere light. To Draper Dave, whose ability to warp space-time with his mere presence very nearly caused me to miss yet another degree cycle. To Olivia, Yehui, and Robert who have been helpful at various times over the course of things (and John Ranson who measured some stuff for me), and Brandon Pierquet, without whom I probably never would have found LEES. The rest of LEES also has my thanks, including the giant cockroaches and sewer rats in 10-082, for making things what they are.

I can't help but acknowledge the USAF (United States Air Force or you non-separated military folk), as I probably wouldn't be here if it weren't for the collusion of a whole lot of things that happened there. My fellow MSI cadre: Jeff Painter (also a groomsman, thanks!), Lupe Sabala, Gary Ayers, Dee Melendez, and even Dean, who shared many thrashings, triumphs, and curse words (like, "those !bleeps! at INYR"). It's doubtful I would be here if I didn't have you guys as a team to make me look good to the admissions folks. I still think that Hanscom SRGH should report to MGH for a cleaning. Is 10.2 up and running yet?

Of course, all my friends from other places who have helped me over the years deserve explicit thanks: Lester Pangilinan, my best man, Abe Chayya (charlie india), Manger, Christie, Deano Busch, George, Monica, Matt, Bill, Jess, Jerry Wilson, everyone who is married to one of these people, unless I don't know you, and everybody I forgot...you know who you are.

To Wendy, my wife, who has been a great help when I need distraction, I love you. Thanks!

To Mom and Dad who managed (by dumb luck!) to bring me into the world, and then (not by dumb luck) helped me find my way all the way here (which is about 4.5 hours from where I started). Thanks! Oh, and to my brothers and sisters, who have been useful at times.



# Contents

---

<b>1</b>	<b>Introduction</b>	<b>17</b>
1.1	Losses in hard switched converters . . . . .	18
1.2	Resonant Power Conversion . . . . .	24
1.3	Contributions and Organization of the Thesis . . . . .	27
<b>2</b>	<b>The <math>\Phi_2</math> Inverter</b>	<b>31</b>
2.1	The class $\Phi$ Inverter . . . . .	31
2.2	The class $\Phi_2$ Inverter . . . . .	35
2.2.1	Basic Operating Principles . . . . .	37
2.2.2	Tuning the $\Phi_2$ Inverter . . . . .	43
2.2.3	Nonlinear Capacitance Effects on the $\Phi_2$ Inverter . . . . .	57
<b>3</b>	<b>The <math>\Phi_2</math> <i>dc-dc</i> Converter</b>	<b>59</b>
3.1	A Resonant Rectifier . . . . .	60
3.2	The Power Stage . . . . .	67
3.2.1	Important Device Characteristics . . . . .	68
3.2.2	Linking the Inverter and Rectifier . . . . .	72
<b>4</b>	<b>Converter Prototypes</b>	<b>79</b>
4.1	The First Prototype . . . . .	79
4.2	A Second Prototype . . . . .	89

<b>5</b>	<b>Closed-Loop Operation</b>	<b>99</b>
5.1	Control Scheme . . . . .	99
5.2	A Resonant Gate Drive . . . . .	101
5.3	The Controller . . . . .	106
5.4	Closing the Loop . . . . .	108
<b>6</b>	<b>Conclusion</b>	<b>115</b>
6.1	Thesis Summary . . . . .	115
6.2	Thesis Conclusions . . . . .	116
6.3	Future Work . . . . .	117
<b>A</b>	<b>SPICE DECKS AND COMPONENT VALUES</b>	<b>119</b>
A.1	Chapter 1 Data . . . . .	119
A.1.1	Fig. 1.4 data: . . . . .	119
A.2	Chapter 2 Data . . . . .	121
A.2.1	Fig. 2.3 data: . . . . .	121
A.2.2	Fig. 2.4 data: . . . . .	122
A.2.3	Fig. 2.7 data: . . . . .	123
A.2.4	Fig. 2.11 data: . . . . .	124
A.2.5	Fig. 2.13 data: . . . . .	126
A.2.6	Fig. 2.14 data: . . . . .	128
A.2.7	Fig. 2.15 data: . . . . .	129
A.2.8	Fig. 2.17 data: . . . . .	132
A.2.9	Fig. 2.19 data: . . . . .	134
A.3	Chapter 3 Data . . . . .	136
A.3.1	Fig. 3.4 data: . . . . .	136
A.3.2	Fig. 3.5 data: . . . . .	137
A.3.3	Fig. 3.6 data: . . . . .	138



A.4 Chapter 4 Data . . . . .	139
A.4.1 ST Converter Final Spice Deck . . . . .	139
A.4.2 50MHz Converter Final Spice Deck . . . . .	145
A.4.3 SPICE Model Libraries . . . . .	151
<b>B PCB Layout Masks and Schematics</b>	<b>159</b>
<b>Bibliography</b>	<b>167</b>

# List of Figures

---

1.1	Synchronous Buck Converter Active vs. Passive Volume . . . . .	19
1.2	Buck-Boost Converter Illustrating Energy Storage Requirements . . . . .	20
1.3	MOSFET Model . . . . .	22
1.4	Class E Inverter Performance vs. Load Resistance . . . . .	25
1.5	VHF Converter Under On-Off Modulation . . . . .	26
2.1	Shorted quarter-wave line . . . . .	32
2.2	Half-wave symmetry/repetition . . . . .	33
2.3	Class- $\Phi$ Inverter and waveforms . . . . .	34
2.4	$\Phi$ Waveforms when inverter is purposefully detuned . . . . .	35
2.5	The $\Phi_2$ Input network and its bode plot . . . . .	36
2.6	The $\Phi_2$ Inverter . . . . .	37
2.7	$\Phi_2$ Inverter waveforms . . . . .	38
2.8	$\Phi_2$ and transmission line responses . . . . .	39
2.9	Block diagram of source substitution method . . . . .	40
2.10	$\Phi_2$ inverter split for harmonic balance analysis . . . . .	40
2.11	$\Phi_2$ network response to initial conditions . . . . .	42
2.12	Duty ratio vs. harmonic composition . . . . .	44
2.13	$\Phi_2$ drain-source impedance effects on drain voltage . . . . .	47
2.14	Tuning sequence to increase peakiness . . . . .	48
2.15	Tuning characteristic impedance . . . . .	49
2.16	Controlling power in $\Phi_2$ inverter . . . . .	50
2.17	Loss vs. tuning in $\Phi_2$ . . . . .	52

2.18 Efficiency vs. tuning in $\Phi_2$ . . . . .	53
2.19 Tuning vs. transient response . . . . .	54
2.20 Efficiency vs. characteristic impedance . . . . .	56
2.21 $\Phi_2$ inverter with nonlinear capacitance . . . . .	58
3.1 Series-loaded resonant rectifier . . . . .	60
3.2 $\Phi_2$ boost converter . . . . .	61
3.3 Series-loaded resonant rectifier in SPICE . . . . .	62
3.4 Rectifier waveforms . . . . .	63
3.5 AC-DC power split in rectifier . . . . .	64
3.6 Tuning rectifier by controlling $F_C$ and $Z_O$ . . . . .	66
3.7 MOSFET parasitic mechanisms . . . . .	68
3.8 Measurement Setup for $R_{DS-ON}$ vs. $V_{GS}$ and Temperature . . . . .	70
3.9 Temperature dependence of MOSFET channel resistance . . . . .	71
3.10 Capacitance Measurement Setup . . . . .	72
3.11 Device capacitance models compared to measurement . . . . .	73
3.12 Rectifier waveforms . . . . .	74
3.13 Inverter and Converter Waveform Overlay . . . . .	75
3.14 Inverter and Converter Waveform Overlay . . . . .	77
4.1 Ranking of devices based on class-E performance . . . . .	80
4.2 $\Phi_2$ converter schematic . . . . .	82
4.3 Diode current ringing around $C_{REC}$ -diode loop . . . . .	83
4.4 ST PD57060 $\Phi_2$ converter simulation results . . . . .	85
4.5 Simulated and measured impedance match . . . . .	86
4.6 ST PD57060 $\Phi_2$ converter measurements . . . . .	87
4.7 ST PD57060 $\Phi_2$ converter experimental waveforms compared to simulation . . . . .	88
4.8 50MHz $\Phi_2$ converter simulation results . . . . .	90

## List of Figures

---

4.9	$\Phi_2$ schematic with component values for BCD process . . . . .	91
4.10	Breakdown of important loss mechanisms for each prototype (simulated)	92
4.11	Experimental waveforms for the 50MHz converter . . . . .	94
4.12	Experimental output power and efficiency . . . . .	95
4.13	Converter photographs . . . . .	96
5.1	VHF Converter Under On-Off Modulation . . . . .	100
5.2	Basic resonant gate drive . . . . .	102
5.3	Gate drive with shunt leg . . . . .	103
5.4	Final gate drive circuit . . . . .	104
5.5	Converter start-up transient . . . . .	105
5.6	Converter shut-down transient . . . . .	106
5.7	Converter efficiency vs. on-off modulation . . . . .	107
5.8	Gate drive power vs. output power . . . . .	108
5.9	Controller Schematic Diagram . . . . .	109
5.10	Closed Loop Operation . . . . .	110
5.11	Modulation frequency dependence on load and $V_{IN}$ . . . . .	111
5.12	Schematic of load for load-step test . . . . .	111
5.13	Transient response to a load step . . . . .	112
5.14	Closed-loop efficiency measurements . . . . .	113
B.1	Schematic of $\Phi_2$ converter with ST part . . . . .	159
B.2	$\Phi_2$ schematic with component values for BCD process . . . . .	160
B.3	Complete gate drive schematic . . . . .	161
B.4	Complete controller schematic . . . . .	162
B.5	ST board layout masks . . . . .	163
B.6	ST board layout masks . . . . .	164
B.7	BCD board layout masks . . . . .	165
B.8	BCD board layout masks . . . . .	166



# List of Tables

---

3.1	Phase Shift differs for the ideal and non-ideal rectifiers when input bias voltage and amplitude are adjusted separately. Opposing effects of the junction capacitance cancel for the case when both bias voltage and amplitude are adjusted simultaneously. . . . .	67
3.2	The components of the dc-dc converter examples are listed in this table. More detailed information including the full spice models and values of parasitic inductances may be found in appendix A	76
4.1	MOSFET parameters . . . . .	81
4.2	Faichild S310, 100V, 3A Schottky diode parameters . . . . .	81
5.1	Hard gating requires more than twice as much power for the custom MOSFET even when the larger gate drive amplitude is accounted for. . . . .	102
B.1	Component values and part numbers for ST-based $\Phi_2$ boost converter . . . . .	160
B.2	Component values and part numbers for Custom-MOSFET-based $\Phi_2$ boost converter . . . . .	160
B.3	Component values and part numbers for gate drive circuit . . . .	161
B.4	Component values and part numbers for controller circuit . . . .	162







# *Introduction*

---

MINIATURIZATION has become the pursuit of modern technology. Ubiquitous use of the term “nano-”, while often cloying, underscores the importance attached to the search for the smaller. The integrated circuit stands as the benchmark to the nano-world, a stark example of how economic power can be harnessed through control of the tiny. While seedling ICs were analog circuits, the shrinking of digital systems occurred much more rapidly as a relentless march on Moore’s law <sup>1</sup>. Today, a common theme in analog circuit design is the development of circuit topologies and techniques that allow the realization of traditional analog building blocks—op-amps, comparators, and the like—on the ever-shrinking CMOS processes. To the extent that more functionality can be realized by adding analog systems to a digital substrate or shrinking analog systems in general, there is money to be made. Take as an example the cellular telephone. The integration of the RF power amplifier along with a host of digital front-end signal processing has fueled the explosion of cell phone usage. While the goal is to have everything on a single chip realizing cost, reliability, performance, and functionality enhancements, some systems are challenging to integrate.

One particular area where integration remains largely a stymied endeavor is power conversion. Here, the issue centers around energy storage. Most switched mode power converters will use inductors and capacitors to fulfill the requirement. The amount of energy storage, and therefore the numerical values of the inductors and capacitors, is a function of the power processed, the switching frequency, and the details of the power processing scheme [1]. Typical converters like the boost or buck converter operating at a few tens of watts require too much energy storage to be integrated given current process constraints. While the statement may seem cavalier, consider that typical inductor and capacitor values for dc-dc converters on the scale of a few tens of watts

---

<sup>1</sup>Moore’s law is mentioned only casually here. The fact is that analog circuits require fewer devices and benefit more from larger feature sizes and the better transistor parameters they engender. Digital circuits, however, rely on massive numbers of iterated structures that switch as rapidly as possible. The result has been an emphasis on shrinking the digital transistor to improve density.

are measured in microhenries and microfarads, whereas integrated inductances and capacitances are more likely to be measured in nanohenries and picofarads. Assuming that three orders of magnitude in energy storage cannot be absorbed in an arbitrarily small volume, and that the techniques that are the subject matter of this thesis are not operating, the assertion is safe.

Typical inductors that might be realized on chip are in the range of a few 10s of nanohenries and capacitors in the 10s of picofarads. The main roadblock to achieving such small values with a conventional converter is loss. The balance of this thesis will explore converter designs intended to circumvent typical loss mechanisms in a manner compatible with integration and co-packaging.

### **1.1 Losses in hard switched converters**

A switched mode power converter constructed of ideal elements has no intrinsic loss mechanism. Rather, they arise inevitably from the use of real components. These losses, distributed among the active and passive components constrain not only the efficiency of the SMPS (switched mode power supply), but the size, cost, form-factor, and even converter responsiveness. Finding ways to beat these losses is, in a sense, tantamount to miniaturization.

On considering a typical dc-dc converter, one fact that becomes obvious is that the bulk of the system, that is its weight and volume, comprises the passive energy storage elements. Semiconductor devices, having benefited from tremendous improvement since their inception, occupy only a small fraction of a typical converter footprint. This is made clear in figure 1.1 showing a common implementation of a synchronous buck converter where switches, gate drives, controller, startup and protection circuits, and the housekeeping power systems are integrated onto a die and placed in a QFN (quad flat-pack, no-lead) package. The remainder of the components are the energy storage devices which require roughly an additional four times the board area (not accounting for interconnect) and nearly *six* times the volume. It is not surprising, then, that techniques to reduce converter footprint might be aimed at minimizing or eliminating passive energy storage.

Where the goal is to reduce the size of the energy storage components, there are two primary ways to proceed. Either energy density may be increased or total converter

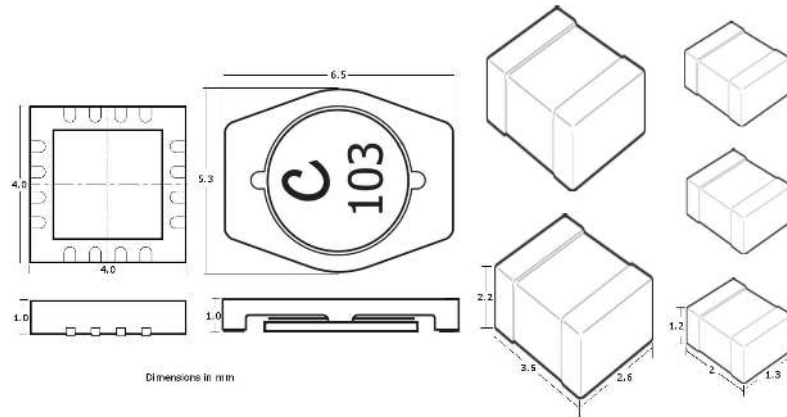


Figure 1.1: The synchronous buck converter components pictured will supply 7.5 W into 5 V. The QFN on the left encompasses the active switches, gate drive, control, and housekeeping functions. The remaining passive elements require 4 times the board area and 6 times the volume, not accounting for board interconnect.

energy storage reduced. Increasing the energy density implies shrinking a device for a constant amount of storage. Even if this can be accomplished, given the physical constraints imposed by power dissipation, the increased losses that result often cannot be reconciled with good converter performance. Considering a solenoidal inductor, it is demonstrated in [2] that fundamental scaling between linear dimensions and flux- or current-carrying area causes inductor  $Q$  to decrease as  $\alpha^2$  where  $\alpha < 1$  is a constant scaling each linear dimension. Similar relationships are enumerated in [3] for other geometries. In the case of capacitors, analogous problems arise. Where a given dielectric material is available, a lower bound exists on the capacitor plate separation for a set working voltage. Further, plate resistance also increases as plate thickness is decreased or plate area is increased, both are necessary to improve energy density. These conditions imply that the capacitor  $Q$  will become unacceptably low with continued scaling at a constant capacitance. Thus a host of factors —  $Q$ , dielectric breakdown, and dissipation — impose a maximum energy density on passive components. Unfortunately, practical densities leave something to be desired for converter size.

With very limited leeway to increase energy density, we turn our attention to reducing the required energy storage. The classic solution is to raise the switching frequency [1], thereby reducing the amount of energy processed per cycle, a condition that leads directly to smaller numerical values of inductance and capacitance. The buck-

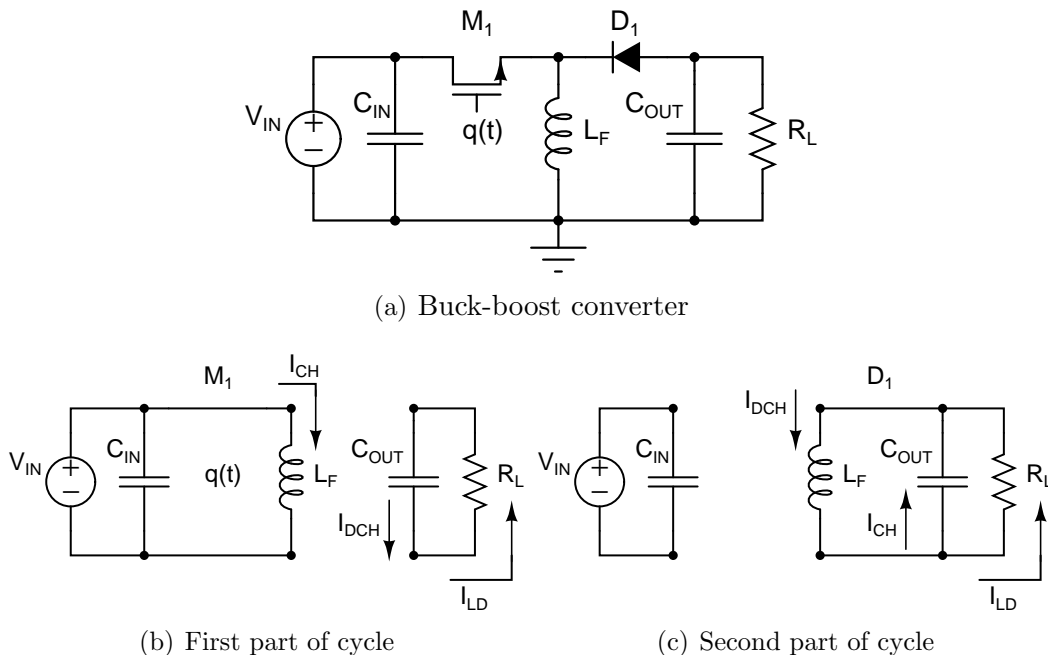


Figure 1.2: In the buck-boost converter,  $L_F$  acts as temporary storage. In the first part of the cycle  $L_F$  is charged by current  $I_{CH}$  while  $C_{OUT}$  holds up the output. In the second portion of the cycle  $L_F$  discharges into the load while replenishing  $C_{OUT}$ .

boost converter in figure 1.2 is a convenient means to an explanation. The buck-boost converter is an indirect converter. This type of converter transfers energy from the source to intermediate storage in the first portion of a cycle and then from intermediate storage to the load in the second portion of the cycle. The intermediate storage in the buck-boost converter is the inductor,  $L_F$ . As the switching frequency is increased and the amount of energy processed each cycle gets smaller, the numerical value of  $L_F$  can be reduced and the inductor made physically smaller for constant energy density. The same applies to the capacitors  $C_{IN}$  and  $C_{OUT}$ . For instance,  $C_{OUT}$  must hold up the output voltage during the half of the cycle when  $L_F$  is charging. The holdup time is inversely proportional to frequency as is the associated  $RC$  time constant for a constant droop in output voltage. Another way to see that  $C_{OUT}$  can be reduced is to consider that  $R_L$  and  $C_{OUT}$  form a low-pass filter which attenuates the switching ripple. As the switching frequency increases the low-pass corner frequency moves up for a given attenuation, relaxing the capacitance requirement.

Though increased switching frequency attends less energy storage, it is not a tech-

nique that may be used haphazardly: A cohort of loss mechanisms arise rapidly to place limits on the operating frequency. While not necessarily the largest of these, important frequency dependent losses in passive elements are limited almost exclusively to inductors and their magnetic materials. Most magnetic materials, used to increase inductance per unit volume, operate well at low frequency but have losses that rise rapidly otherwise. The basic trend is captured by the Steinmetz equation:

$$\overline{P_v(t)} = k f^\alpha B^\beta \tag{1.1}$$

where  $\overline{P_v(t)}$  is the time-average loss per unit volume [ $kW/m^2$ ],  $B$  is the peak ac flux amplitude [Gauss],  $f$  is the frequency of sinusoidal excitation [Hz], and the constants  $k$ ,  $\alpha$ , and  $\beta$  are found by curve fitting. Examining 1.1 it is clear that for  $\alpha$  greater than one (it's often in the range of 1-3) that the loss will rise briskly with frequency. Another important implication is that the core volume may be increased to reduce the flux density, trading increased size for higher frequency—the opposite of the desired effect<sup>2</sup>. In truth, the Steinmetz equation is only valid in a narrow range of situations, primarily where the excitation is sinusoidal and relatively low frequency. At high frequencies and under the non-sinusoidal excitation typical of power converters, the losses tend to be greater than predicted in the Steinmetz model and many different modeling approaches have been undertaken to get a more accurate prediction (for instance, [4]). The upshot, however, is that most bulk magnetic materials are not suitable for operation at frequencies much higher than a few megahertz.

One way of avoiding magnetic core losses is to do away with the magnetic core. The lower energy density demands even higher operating frequencies, but to the extent that the frequency can be increased, the magnetic loss picture looks much better. For a simple air core inductor, the inductance and resistance are determined primarily by geometry and the choice of conductor. Inductor quality factor  $Q$  is:

$$Q = \frac{\omega L}{R} \tag{1.2}$$

In this simple relationship, expressing the ratio of energy stored to energy lost per

---

<sup>2</sup>Often loss becomes the limiting factor at high frequency and flux derating is necessary to avoid excessive heat build up. Thus at high frequency cored inductors can actually get *larger*.

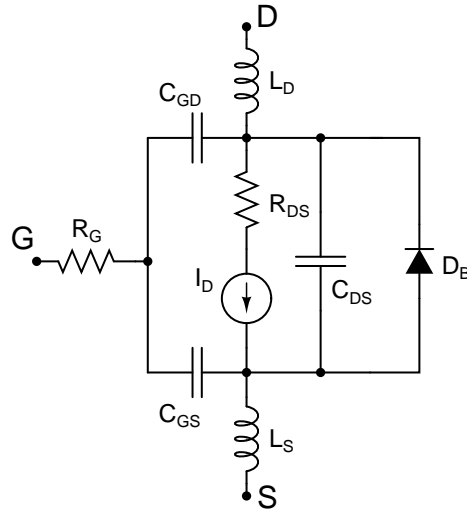


Figure 1.3: A MOSFET including parasitic elements usually important in hard switched dc-dc converter design

cycle,  $Q$  increases with reactance and decreases with resistance. The frequency dependence of  $R$  and  $L$  are very difficult to calculate for any geometry other than isolated straight wires. In general, skin effect, proximity effect, and interwinding capacitance affect both  $L$  and  $R$  [3]. If the proximity effect and the interwinding capacitance are ignored, the skin effect results in approximately a square-root increase in resistance with frequency. Since reactance rises linearly under these assumptions, then  $Q$  will increase  $\propto \sqrt{f}$ . Measurements of inductor  $Q$  and information available from manufacturers of air-core RF inductors indeed show that  $Q$  increases with frequency as a general trend.

The seemingly synergistic effect of increasing  $Q$  with frequency for air-core inductors is only advantageous provided that the other frequency dependent loss factors are dealt with. These losses are associated with active semiconductor devices. Semiconductor losses can be divided into three main mechanisms for MOSFETs: conduction loss, switching loss, and gating loss. A MOSFET model including the parasitic elements usually considered in dc-dc converter design is shown in fig. 1.3.

Conduction loss, due to the effective resistance of the channel, the lightly doped drain region (LDD), and metal/bondwire resistance, is only slightly frequency dependent<sup>3</sup>. Switching loss, however, depends significantly on frequency. It is helpful

---

<sup>3</sup>At typical operating frequencies the quasistatic assumptions for MOSFETs are valid, so the

to further divide switching loss into overlap loss and losses resulting from discharge of the drain-source capacitance,  $C_{DS}$ . Overlap loss refers to the condition where the MOSFET supports simultaneous voltage and current at its drain-source port and thereby dissipates power. This condition arises from the need to charge or discharge the device channel through finite source impedance (whether this impedance arises externally or as a result of device parasitic resistance and inductance) which imposes a minimum on switch transition times. Simplified models of overlap loss parameterized in converter nominal voltage ( $V_O$ ) and current ( $I_O$ ), and MOSFET rise ( $\tau_r$ ) and fall ( $\tau_f$ ) times are readily available [5, 1]:

$$E_r + E_f = kV_O I_O (\tau_r + \tau_f) \quad (1.3)$$

The constant  $k$  reflects the circuit in which the device is used and varies between 1/6 and 1/2 depending on whether the load is purely resistive or clamped inductive. Since this result is basically fixed once the device and circuit are chosen, the energy per transition ( $E_r + E_f$ ) is also fixed. Therefore, as switching frequency rises, so does overlap loss.

The loss due to  $C_{DS}$  occurs at device turn on, when the energy stored on the output capacitance is dumped into the switch yielding a loss that can be roughly approximated as:  $\frac{1}{2}C_{DS}V_{DS-PK}^2 f$ . This effect can be significant even at frequencies well below a megahertz— $C_{DS}$  is usually fully charged just before turn-off.

Gating loss results from charging and discharging the input capacitance,  $C_{ISS} = C_{GS} + C_{GD}$ . Calculating the gating loss is somewhat complicated by the presence of  $C_{GD}$  which is multiplied according to the Miller effect during transitions. In lateral MOSFETs where  $C_{GD}$  tends to be very small and its effects can be ignored, the gating loss is approximately expressed as:

$$P_{GATE} = C_{GS} V_{GATE-PK}^2 f \quad (1.4)$$

This reflects that the loss is associated with the loss of charging a capacitor from a dc voltage through a resistor,  $\frac{1}{2}CV^2$ , and the subsequent dumping of the stored energy

---

channel and LDD components of  $R_{DS-ON}$  are constant. Bondwire resistance is usually a small enough component that skin effect only accounts for a small change in the total  $R_{DS-ON}$ .

once per cycle. In other types of MOSFETs, such as vertical DMOS and even some lateral devices,  $C_{GD}$  is a significant portion of  $C_{ISS}$  and the effects can't be ignored. Then the gate power is usually expressed in terms of the total charge required per cycle to enhance the device:

$$P_{GATE} = Q_G V_{GATE_{PK}} f \quad (1.5)$$

In both cases the frequency dependence is clearly linear. This mechanism becomes important at switching frequencies of a few megahertz and beyond where gating loss for typical devices can range from hundreds of milliwatts to several watts.

Diodes also account for a fraction of the converter loss budget. All diodes have an associated forward voltage drop,  $V_F$ , that combines with the forward current,  $I_F$ , and resistive losses in the bulk regions to result in diode conduction loss. This mechanism is not explicitly frequency dependent. PN-junction diodes and PIN diodes, however, do have a frequency dependent loss mechanism - reverse recovery. Reverse recovery names the process in which stored minority carriers are removed during commutation. During the reverse recovery time,  $\tau_{RR}$ , the carriers are extracted across a constant voltage. Since this time is related to the amount of stored charge and the impedance of the external circuit,  $\tau_{RR}$  is fixed for a given configuration. Therefore, the energy wasted per cycle to reverse recovery is constant implying frequency dependence. Schottky diodes, which are formed as metal-semiconductor junctions are majority carrier devices. They do not suffer heavily from reverse recovery losses, but are only available with breakdown voltages below about 120 volts.

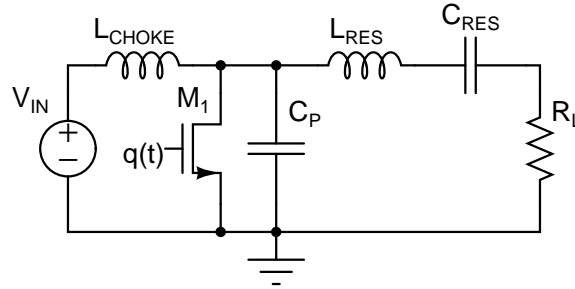
## 1.2 Resonant Power Conversion

Resonance, usually ascribed to systems with complex poles displaying oscillatory behavior, is of some significance in power conversion. In filtering, for example, it plays a role to develop large immittance in comparatively little volume<sup>4</sup>. Here we look at resonance as a means to push back converter loss mechanisms and realize operation

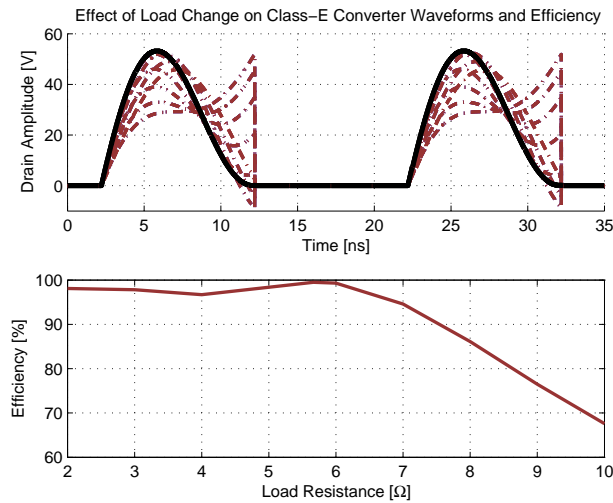
---

<sup>4</sup>Series and parallel resonant filters can be used to shunt or block ripple in power converters. It was demonstrated in [6] that by using resonance, filter element volume could be reduced by better than a factor of three.





(a) Class E inverter



(b) 50 MHz Class E drain voltage waveforms

Figure 1.4: **Resonant topologies often suffer from limited load range in power conversion applications. Here, the Class E inverter waveforms are pictured as the load is varied from  $\frac{1}{2}R$  to  $2R$ . The properly tuned waveform is displayed in heavy black. The loss of ZVS and negative impact on efficiency are evident.**

in the very high frequency regime (VHF, 30 MHz - 300 MHz).

A number of converter topologies exist that draw from RF amplifier techniques to achieve efficient energy conversion [7, 8, 9, 10, 11, 12, 13, 14, 15] at high frequencies. These designs rely on reactive networks to shape the switch voltage and current and reduce switching loss. The class E converter, fig. 1.4(a), is a widely practiced topology whose network enforces a zero-voltage switching (ZVS) opportunity at turn-on. Its basic operation can be classified as indirect. The inductor  $L_{CHOKE}$  is an open at the switching frequency, ensuring that only dc current flows from the source. With no dc path to the load, energy from the source must first be stored on the switch shunt

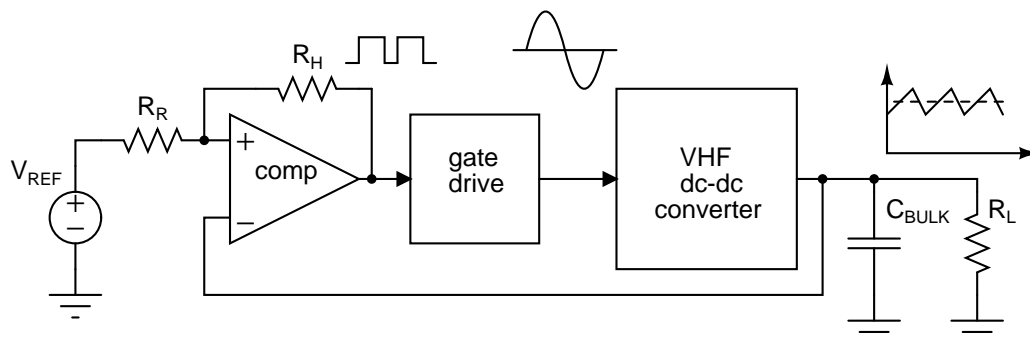


Figure 1.5: **Schematic depiction of VHF converter under on-off modulation. The closed-loop system keeps output voltage constant allowing the converter to deliver a constant power (effectively it sees a constant load) at it's most efficient point. Actual power delivered to the load depends on the duty ratio of the control signal.**

capacitor  $C_P$ . The energy stored in  $C_P$  then rings towards the load in a cycle that is determined by the switching function,  $q(t)$ , and the resonant tank formed by the load,  $L_{RES}$ , and  $C_{RES}$ . It functions by ringing the energy on  $C_{DS}$  to the load once per cycle. When these components are tuned according to [7, 8], the drain voltage will naturally return to zero as the energy in  $C_P$  rings toward the load. At this point, the switch may be turned on with minimal loss. This mode of operation avoids the losses usually ascribed to the switch drain-source capacitance and largely avoids overlap loss, as well.

In practice, the drawbacks of such resonant topologies have prevented them from seeing widespread use. To begin with, the load range is severely restricted when compared with the 100:1 or better range achievable with conventional converters. Resonating losses from circulating reactive currents become significant as the load is reduced, hurting efficiency. The situation is made worse in the many cases where the load is an integral part of the resonance. Then, any change in load disrupts the ZVS condition and switching loss inevitably arises. This situation is depicted in fig. 1.4(b). Further difficulty arises because duty ratio control is often not possible. Instead, control is achieved by varying the switching frequency. The resulting poor dynamics worsen with frequency and place an artificial upper bound on practically achievable switching speed. Many resonant converters also suffer from high peak switch stresses. The class E converter, in particular, has peak drain voltages rising as high as 4.4 times the dc input voltage [16]. This is particularly troublesome where integration is concerned because integrated devices tend to have lower breakdown

voltages.

Several of these issues can be resolved by partitioning the energy storage and control functions [17, 18, 19]. Instead of controlling the output by varying the switching frequency, on-off modulation of the converter determines the fraction of output power delivered (see fig. 1.5). When the converter is on, it delivers a fixed power maintaining ZVS and maximum efficiency. When off, no power is delivered and there are no associated resonating losses. Under these conditions the load range is a function of the minimum achievable modulation index. Such operation allows the network to be tuned to enforce ZVS at one particular operating point. The result is maximum efficiency, better dynamics, and higher achievable operating frequency. The fact that this mode of operation allows much higher switching frequency is self-reinforcing—high frequency means less energy storage so the converter can be started and stopped more rapidly and achieve a wider load range.

## 1.3 Contributions and Organization of the Thesis

Raising the switching frequency is a well known means of reducing required energy storage in power converters. It is precisely this reduction that can put inductor and capacitor values into the range that they might be considered for integration. For inductors, in particular, VHF operation allows magnetic materials to be set aside, avoiding the difficulty and expense of incorporating them on chip. Even so, it is not clear that current techniques, like the planar spiral inductor, can offer high enough  $Q$  or reasonable area. Generally, integrated inductors achieve  $Q$ 's of ten or below with inductance in the neighborhood of 10-20 nH [20, 21]. While the techniques discussed in this thesis result in small value inductors, the  $Q$  needs to be at least 50 or better. Capacitors are also a challenge. Typical CMOS processes achieve about  $1 \text{ fF}/\mu\text{m}^2$  metal to metal capacitance. Higher density requires the use of inherently non-linear (and potentially lossy) gate capacitance. Yet these considerations are secondary to the question of whether or not devices available on the existing power processes are suitable to high frequency operation. The exploration and development of techniques that permit this answer to be “yes” is the primary contribution of this thesis.

Breakdown voltage is a key aspect in determining integrated process suitability. While adopting resonant circuit techniques permits low loss and high frequency, it also poses very high switch stresses. The class E converter, for instance, has an idealized peak

voltage stress of 3.6 ranging up to 4.4 in practice. Since integrated processes do not enjoy the luxury of high breakdown voltage, attempting to implement a topology like the class E would significantly limit the input voltage range. Some RF amplifiers like the class F are able to reduce the peak stress by waveshaping [22, 23, 24], but at the expense of relatively high component count. In chapter 2 a new inverter we call class  $\Phi_2$  is introduced along with a tuning method that permits low peak voltage stress. The low voltage stress achieved (2 in simulation, 2.4 in experiment) is critical to implementing a converter with an input voltage up to 18 V on a 50 V power process, which for instance is not possible with a class E topology. The  $\Phi_2$  also has a low component count and eliminates the need for an RF choke. With the few inductors resonant and small, the  $\Phi_2$  has excellent dynamics and makes a good candidate for integration.

Efficient rectification compatible with integration is introduced alongside the  $\Phi_2$  dc-dc converter in chapter 3. Many resonant rectifier topologies exist for RF inverters [13, 25, 26, 27, 28]. The particular topology set forth here offers a low component count. When mated with the inverter the result is a resonant boost converter that transfers power at ac and dc. The dc portion varies with the boost ratio and is advantageous because it does not suffer resonating losses. Almost all the power delivered at ac is delivered at the fundamental, where the rectifier is tuned to appear resistive. Significantly, the rectifier tuning changes with the dc input voltage causing the output power to vary nearly linearly with input voltage. Though this complicates design, it offers an additional degree of freedom to tailor the desired converter behavior.

Device characterization and selection are critical. At VHF frequencies, the parasitic components must be embraced rather than avoided. This is a key strength of the  $\Phi_2$ , which can absorb the switch output capacitance as part of the wave shaping network. Both the magnitudes and distribution of the parasitic capacitance, inductance, and resistance are important considerations. Chapter 3 also discusses these particular aspects, and lays out the techniques used in measuring and modeling them.

Chapter 4 presents the design and experimental results of two dc-dc converter power stages. The first converter uses an off-the-shelf power LDMOS normally used in RF power amplifiers. The other converter uses an LDMOS device fabricated in a conventional silicon power process. Comparisons between the converters are drawn that help illustrate the effects of different tuning choices at design time.

The gate drive and closed-loop performance are discussed in chapter 5. In the VHF

regime the gate drive is not a trivial ancillary issue. Hard gating with a totem-pole driver is out of the question. Even ignoring direct path losses in such a circuit, hard gating loss is too high. For that reason a resonant design was employed. The two key factors for a gate drive in this architecture are efficiency and startup time. Resonant schemes will naturally benefit over hard gating where efficiency is considered because some portion of the gate energy is recovered each cycle. On the other hand, direct control of duty ratio and dynamic response are compromised. A topology and specific tuning techniques are discussed that attempt to find the best trade offs.

Closed-loop performance is a prerequisite for having a converter, per se. In chapter 5 a voltage-mode hysteretic controller closes the loop. The hysteresis band determines the converter peak to peak voltage ripple. A bulk capacitance in conjunction with the load sets the modulation frequency limits. Dynamic performance is excellent as the bandwidth is determined not by the modulation frequency, but by the delay through the controller and the power stage dynamics, both of which are much faster.

Resonant power conversion with the  $\Phi_2$  resonant boost converter can be accomplished with transistors built from a standard power process. VHF frequencies keep energy storage at a minimum yielding small component values and excellent dynamic performance. This and a discussion of future directions for related work are presented in chapter 6, the conclusion.



# *The $\Phi_2$ Inverter*

---

CHAPTER 1 laid out the basic considerations for conversion at VHF switching frequencies and the attendant miniaturization advantages. While resonant conversion techniques are compelling in this regard, several key aspects make them difficult to integrate. At the top of the list is peak switch voltage stress. In practical implementations of the class E converter, for instance, the main switch must endure peak voltages up to 4.4 times the input voltage. This alone is enough to break an integrated implementation. Designs like the class F converter use wave shaping techniques to reduce the switch stress, but the result is a large component count. Many such converters also suffer from the need for a bulk inductor to function as an rf choke at the input. This limits dynamic performance and poses yet another challenge to integration. While variants like the second harmonic class E converter avoid this problem, no topology yet presented offers the combination of low switch stress, low component count, and minimal energy storage. Such a converter does exist and it is called the  $\Phi_2$  converter.

## **2.1 The class $\Phi$ Inverter**

As an aid to our understanding of the  $\Phi_2$  inverter's operation, we briefly digress to examine its progenitor, the class  $\Phi$  inverter [2, 24]. This inverter exploits the symmetrizing properties of a shorted quarter-wave transmission line in order to realize efficient high frequency conversion. The impedance characteristic of such a line is plotted in fig. 2.1 where the poles appear at the odd integral multiples of the fundamental and zeros obtain at the even integral multiples. The symmetrizing properties are exposed naturally on considering the effect of driving the line with a finite-impedance voltage source periodic in the fundamental. High impedance at the odd harmonics blocks current, permitting the source to impress odd harmonic voltages without ef-

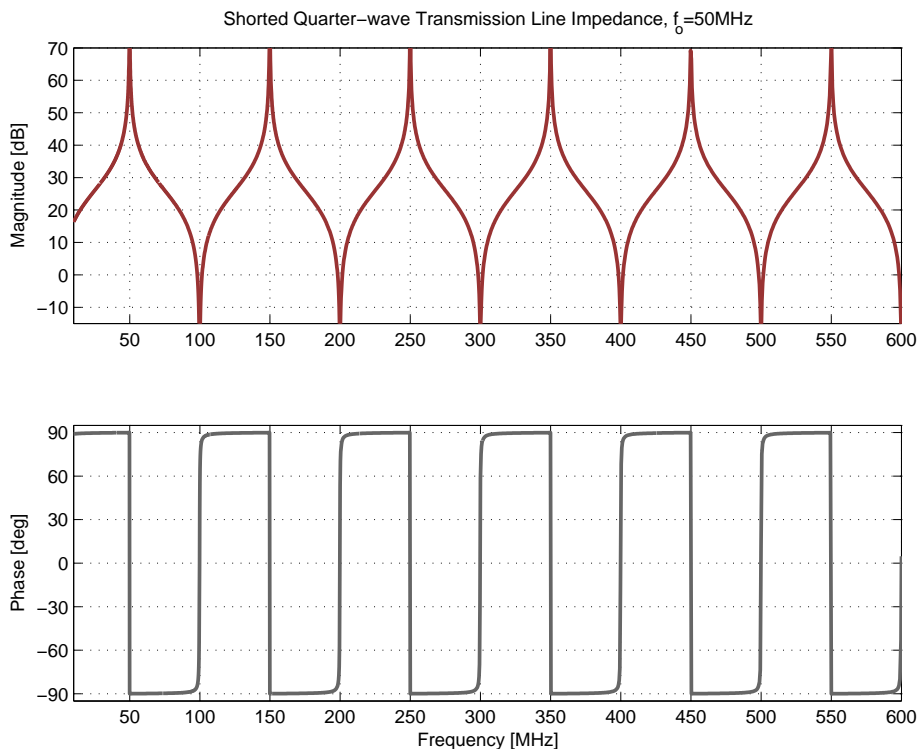


Figure 2.1: **Impedance characteristic of a shorted quarter-wave transmission line.**

fort. The situation is reversed for even harmonics—the line demands large currents, nulling the source voltage. Under these conditions the periodic steady state voltage at the driven port of the line will consist exclusively of odd harmonic components and the current even harmonic components. The signals will then be half-wave symmetric and half-wave repeating respectively, a fundamental result of Fourier analysis. By way of illustration, two signals are constructed with arbitrary combinations of even and odd components in fig. 2.2. In each plot the sum is depicted by the heavy line. The sum in the top plot, composed exclusively of odd components is half-wave symmetric. In the bottom plot, the even components result in a half-wave repeating sum.

The  $\Phi$  inverter, fig. 2.3(a), consists of a shorted quarter-wave transmission line terminating at the drain-source port of its switch and a resonant output tank. While the quarter-wave line enforces drain voltage symmetry in periodic steady state, it is the interaction of the tank with the shunt capacitance,  $C_P$  (usually device parasitic capacitance, although external shunt capacitance may be added), that ultimately



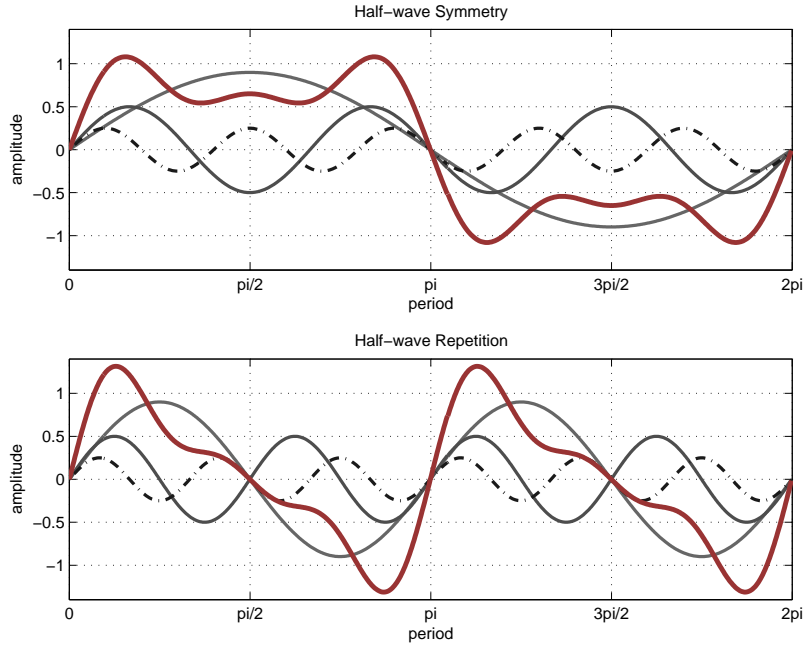
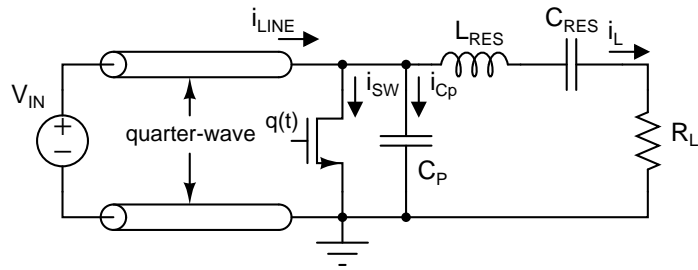


Figure 2.2: **Half-wave symmetric and half-wave repeating waveforms.**

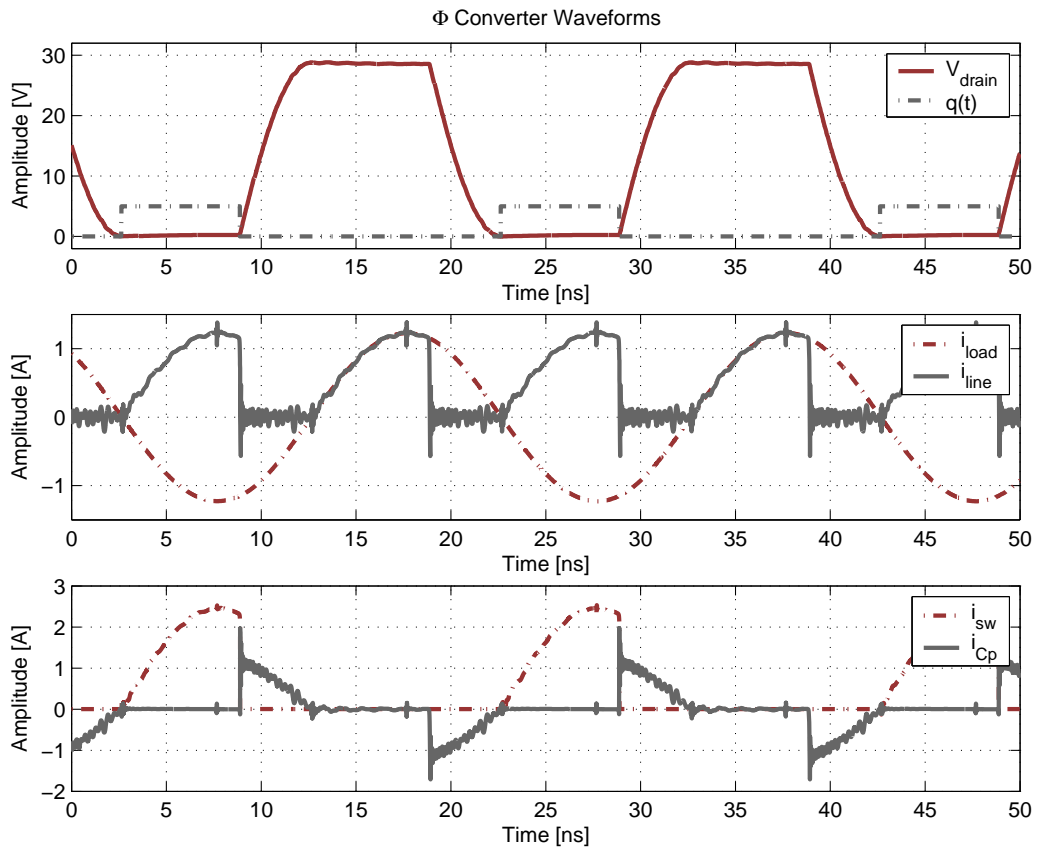
creates ZVS and high efficiency. Considering the waveforms in fig. 2.3(b) the drain voltage is clearly half-wave symmetric. It has a dc average component equal to the source voltage, a condition of achieving periodic steady state, which also serves as the axis of symmetry. The switch holds the drain node at ground for a portion of the cycle defined by  $q(t)$ . When the switch turns off, the line current falls abruptly to zero and the load current charges  $C_P$  to the peak drain voltage,  $2V_{IN}$ , a value that results from reflection about the DC average<sup>1</sup>. Once  $C_P$  has charged to  $2V_{IN}$ , the line current again equals the load current, and the drain voltage remains constant. After a period equal to the switch on-time, the line current falls to zero and the load current discharges  $C_P$ , ringing the drain to zero and creating an opportunity for the switch to turn on without loss.

It is important to note that the symmetry in drain voltage does not guarantee ZVS. For instance the waveforms in fig. 2.4 show what would happen if the value of  $C_P$  is halved. The load network draws too much charge out of the capacitor and the

<sup>1</sup>One can also consider that the switch effectively launches a voltage wave of  $-V_{IN}$  down the line which must return a half cycle later inverted to satisfy the boundary conditions established by the short. With a dc average of  $V_{IN}$  the additional  $V_{IN}$  from the returning wave adds to the peak voltage,  $2V_{IN}$ .



(a) Class  $\Phi$  Inverter



(b) 50 MHz Class  $\Phi$  Inverter Waveforms

Figure 2.3: The class  $\Phi$  inverter tuned for soft switching at 50 MHz. The shorted quarter-wave line ensures the drain voltage is half-wave symmetric. The rising and falling edges of the drain voltage are due to the charging and discharging of  $C_p$  each cycle by the difference between  $i_{line}$  and  $i_{load}$ . Important to note is that the ZVS condition is not guaranteed by half-wave symmetric voltage alone. The load network and switch capacitance must interact so that the drain voltage reaches zero at the appropriate moment. See appendix A for component values and simulation files.

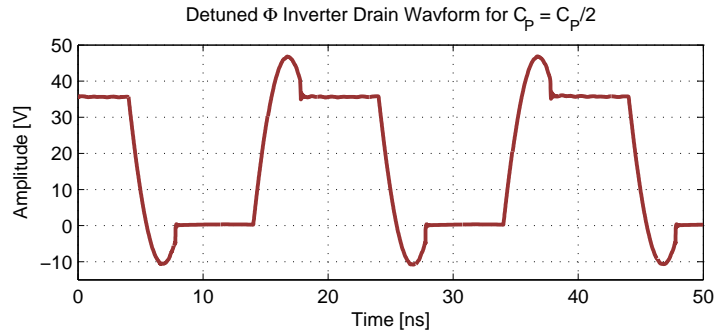


Figure 2.4: In the  $\Phi$  inverter, the transmission line enforces half-wave symmetry. When the load network and shunt capacitance  $C_P$  are unmatched, loss results at both transitions. Component values and simulation files can be found in appendix A

drain voltage undershoots zero. The symmetry enforced by the line then causes a corresponding overshoot one half-cycle later. This operating condition forces the switch to dissipate energy from the capacitor each half-cycle, a lossy proposition.

Limits on power delivered to the load at a given  $C_P$ , frequency, and input voltage naturally arise where all the energy stored on  $C_P$  must come from the load side. In steady state, the load current must be exactly the right value to ring the drain to zero. Once the duty ratio has been constrained, the tank current is fixed, and so is the output power because the load resistance necessarily plays a role in determining the tank current. Since  $C_P$  is smallest when composed exclusively of device parasitic capacitance, there is a minimum power delivered to the load for a given switch, switching frequency, and input voltage. The  $\Phi_2$  inverter, having the ability to absorb device capacitance into either the load network or its source network has greater freedom in this regard.

## 2.2 The class $\Phi_2$ Inverter

The class  $\Phi_2$  inverter, like the  $\Phi$  inverter, exploits waveshaping techniques to realize approximate half-wave symmetry and the related benefits. It diverges on the point of how many harmonic-coincident resonances are employed to achieve the effect. Where the ideal  $\Phi$  inverter relies on an infinite number of harmonics, the  $\Phi_2$  network seeks to control only the first three. The resulting *approximate* half-wave symmetry reaps

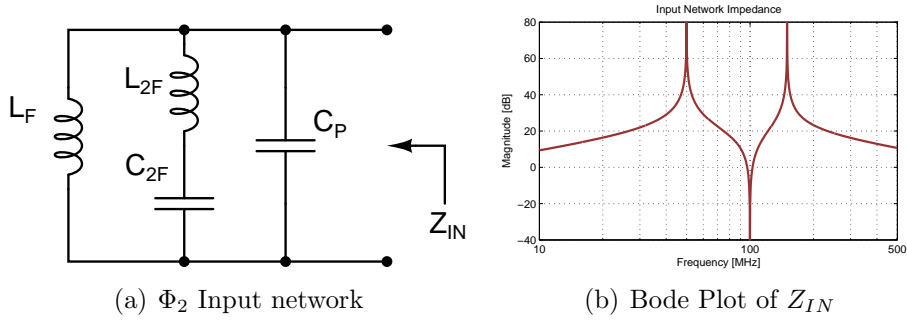


Figure 2.5: **The impedance of the  $\Phi_2$  input network can approximate a shorted quarter-wave transmission line.**

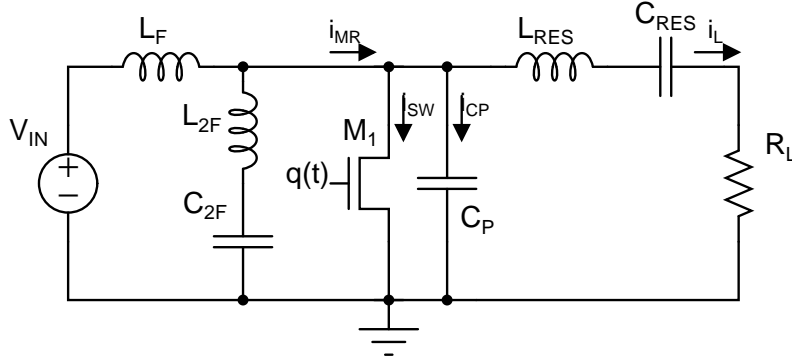
the rewards of ZVS yet allows greater flexibility in establishing the details of the waveform shape while avoiding need for many resonant elements. Key to meeting the requirements of integration, this flexibility also comes with reduced design complexity. Practical implementations of the class  $\Phi$  inverter control perhaps a dozen harmonics [2, 24]. The associated multi-resonant structures require significant design effort, are sensitive to process variation, and difficult to change. In contrast, the  $\Phi_2$  inverter's low-order lumped network can be readily tuned to establish a desired impedance, reducing the design effort.

For instance, the lumped network depicted in fig. 2.5 has an impedance characteristic that is identical to that of the shorted quarter-wave transmission line for the first three harmonics. When the component values are selected according to eqns. 2.1 the poles occur at the fundamental and third harmonic with a second harmonic zero.

$$L_F = \frac{1}{9\pi^2 f_{SW}^2 C_F} \quad L_{2F} = \frac{1}{15\pi^2 f_{SW}^2 C_F} \quad C_{2F} = \frac{15}{16} C_F \quad (2.1)$$

This network can be viewed as a parallel combination of series- and parallel-resonant tanks. The series tank,  $L_{2F}$  and  $C_{2F}$ , is tuned to the second harmonic, creating the zero. The inductor  $L_F$  in the parallel tank provides the low-frequency asymptote and resonates with the other elements to create the peak at the fundamental, and the capacitor  $C_F$  provides the high-frequency asymptote resonating with the other elements to create the peak at the third harmonic.

The addition of a parallel switch and an output tank comprised of  $R_L$ ,  $C_{RES}$ , and  $L_{RES}$  in fig. 2.6 establishes the complete  $\Phi_2$  inverter. Here the transmission line of

Figure 2.6: **The  $\Phi_2$  Inverter.**

the  $\Phi$  inverter is replaced by the lumped network of fig. 2.5(a).  $C_F$  becomes the switch capacitance plus any shunt capacitance added at design time. The output “tank” can be dealt with in several ways. Used as a resonant tank, it may be tuned to look resistive at the fundamental or slightly inductive to aid switching (it could be tuned to look capacitive, but greater circulating currents exacerbate loss). As an alternative, the capacitor  $C_{RES}$  can act as a dc block while  $L_{RES}$  and  $R_L$  function as an impedance divider to control load power.

### 2.2.1 Basic Operating Principles

In the  $\Phi_2$  inverter we have a network with a second harmonic short, and high impedance at the fundamental and third harmonic. Ignoring, for the moment, higher frequency content, the network will support predominantly odd harmonic voltages (fundamental and third) thus sharing the same half-wave symmetric properties as the  $\Phi$  inverter. Each cycle the switch forces the drain voltage to zero for a period  $DT$ , where  $D$  is the duty ratio. At turn off the network rings to roughly twice the dc average voltage at the drain,  $2 \cdot V_{IN}$ , before heading towards zero and the beginning of the next cycle. Under these conditions, zero voltage switching permits efficient operation.

The simulated waveforms in figure 2.7 indicate the true operation is more complicated. The drain voltage peak is not the mirror-image plateau of the  $\Phi$  inverter. Instead, telltale humps arise as they must where the harmonic content is limited. Half-wave symmetry is exposed as approximate by the same, indicating that some even order

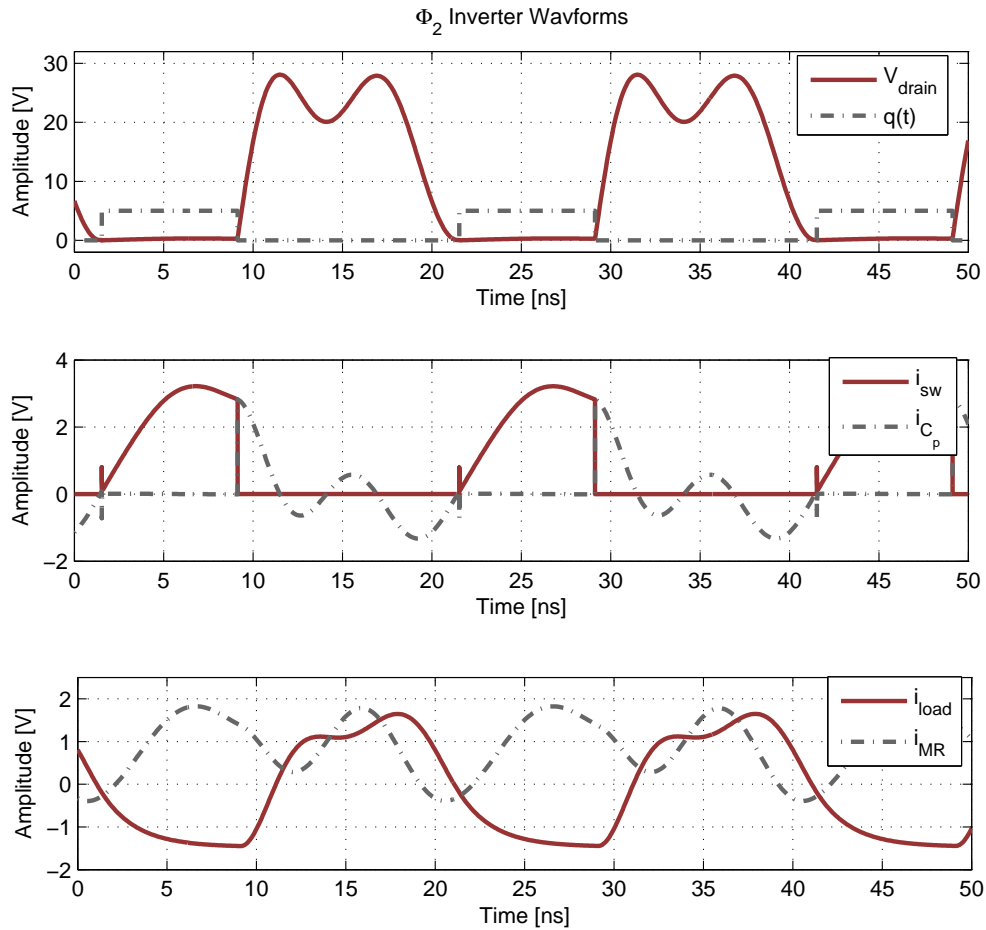


Figure 2.7: The  $\Phi_2$  inverter tuned for operation at 50MHz. The drain voltage displays only approximate half-wave symmetry because the network only controls the first few harmonics. Notice that the switch current is substantially similar to that of the  $\Phi$  inverter (fig. 2.3(b)), but the other currents depart creating the telltale  $\Phi_2$  humps. Component values and simulation files are in appendix A

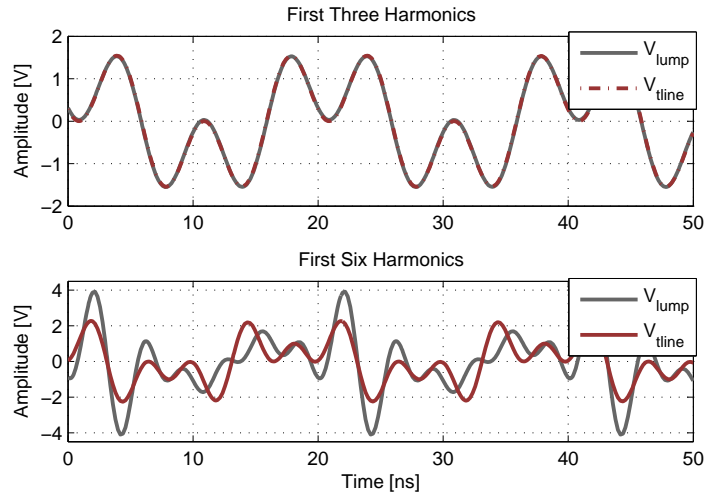


Figure 2.8: In the top plot both an ideal quarter-wave transmission line and the lumped network process the first three harmonics identically. When higher frequency content is added at equal power, the behaviors diverge. The transmission line still enforces half-wave symmetry, but the lumped circuit does not.

harmonics play a role in determining the drain waveform. Nevertheless, the system's behavior is within a stone's throw of what might be expected: there is *approximate* half-wave symmetry.

Figure 2.8 shows how the  $\Phi_2$  input network and a shorted quarter-wave transmission line compare in handling signals of differing harmonic content. When the drive current is composed solely of the first three harmonics, all equal in amplitude, the resulting voltage is exactly half-wave symmetric just as the shorted quarter-wave transmission line case. When equal amplitude components of the first six harmonics are applied, the response differs substantially from the ideal line. If the assumption of approximate half-wave symmetry is to be valid, most of the energy in the drive signal must be in the first few harmonics.

A useful way to define a drive signal in the  $\Phi_2$  inverter is found in methods commonly associated with the harmonic balance technique [29]. The harmonic balance technique, used as a computationally-lightweight means of solving for the steady state response, relies on separating a circuit into a minimum set of linear and nonlinear subcircuits. By then splitting the subcircuits at their common terminals and augmenting them with independent sources, each source can be made to produce a drive signal where all the terminal variables are consistent (by means of an optimization

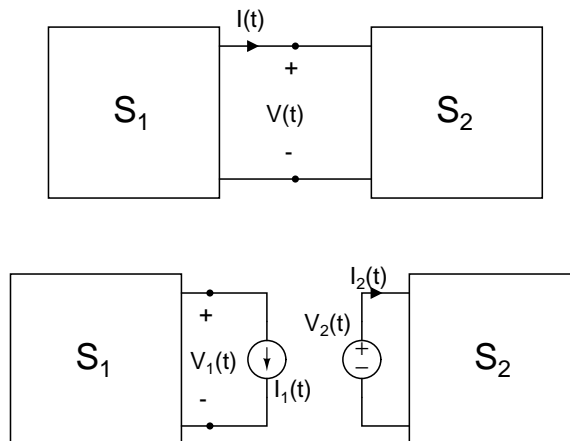


Figure 2.9: **Splitting a circuit into two subcircuits.**

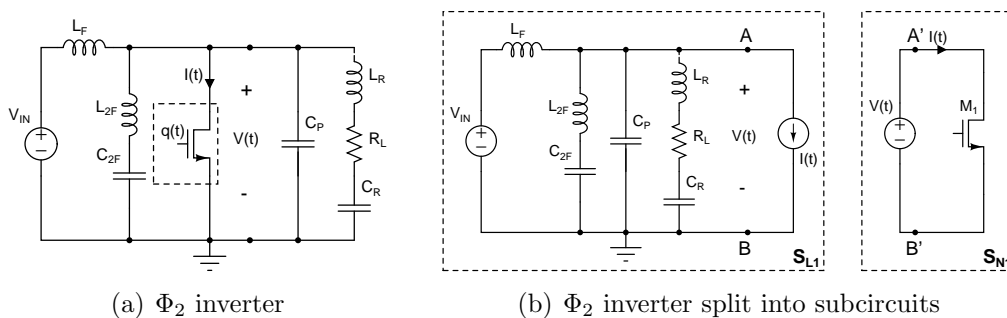


Figure 2.10:  $\Phi_2$  inverter broken down into subnetworks. The network on the left hand side of figure (b) is the complete drain-source network with drain-source impedance  $Z_{AB}$ . The MOSFET is replaced by a linear independent current source,  $I(t)$ .

algorithm, for instance), at which point the solution is known. For example, figure 2.9 depicts a circuit consisting of two sub-circuits,  $S_1$  and  $S_2$  that share the variables  $V(t)$  and  $I(t)$  at their terminals. The network is split as illustrated, where  $S_1$  now has a drive current  $I_1(t)$  and  $S_2$  a drive voltage  $V_2(t)$ . If a unique solution exists among the branch variables of the sub-circuits, when  $I_1(t) = I(t)$  and  $V_2(t) = V(t)$ , then  $I_1(t) = I_2(t) = I(t)$  and  $V_1(t) = V_2(t) = V(t)$ . This amounts to the substitution of sources for subcircuits. In the case where a complete circuit is nonlinear, that portion can be replaced with a linear source and the resulting subcircuit is linear.

When this technique is applied to the  $\Phi_2$  inverter in fig. 2.10, the obvious choice for the nonlinear sub-circuit is the only non-linear element, the MOSFET, outlined in fig 2.10(a). The balance of the circuit forms a completely linear sub-network shown as



$S_{L1}$  in fig. 2.10(b). With the drain voltage as the dependent variable, an independent source  $I(t)$  is chosen to augment  $S_{L1}$ . It is evident that this  $I(t)$  is the switch current, what remains is to determine its harmonic content.

The harmonic balance technique does not require that the switch is substituted with a current source. A voltage source is equally valid and a convenient means of establishing what  $I(t)$  might look like in the frequency domain. Three of the circuit branches contain series inductors and naturally shape a current signal with tapering high-frequency content. Even for a square-wave voltage source equal to the duty ratio (the worst case physically significant source in terms of frequency content) these branches will shape a current with diminishing signal energy above the third harmonic. The capacitor  $C_F$  has an impedance that falls with frequency and will tend to contribute to higher order harmonic currents. However, in any real system the switch will have a finite commutation time, limiting the frequency content. Further, while  $C_F$  may have significant current at higher frequencies, the voltage will be small due to low impedance. The current  $I(t)$  is then the sum of the frequency components of the four branch currents. With a network impedance as described above, having a zero at the second harmonic and falling monotonically above the third, the drain voltage bears out the desired characteristics—dominantly fundamental and third harmonic content and approximate half-wave symmetry.

A time-domain view of the  $\Phi_2$  inverter can also be useful. When the switch is opened, the network is identical to  $S_{L1}$  (minus the current source  $I(t)$ ). Upon switch closure,  $C_P$  is replaced by a short circuit. In each case, the final state of the circuit at the switch transition is passed on as the initial conditions for the next portion of the switching cycle. In periodic steady-state, the switch cycles on to conduct a ramping current through  $L_F$ , the returning load current through  $L_{RES}$ , and current from the second harmonic tank. As the switch opens, the initial conditions established by these currents, along with energy from  $V_{IN}$  causes the network to ring at its modal frequencies, charging and then discharging  $C_P$ . The result is the  $\Phi_2$  drain voltage waveform. In figure 2.11 the complete response of this ringing is identical to the simulated drain voltage waveform for a period  $(1 - D)T$ , at which point the switch is cycled on to reestablish the initial conditions. The zero-state and zero-input responses in the plot show how stored energy and energy from the source,  $V_{IN}$  contribute to the ringing.

At present, determining the exact component values (whether from time or frequency domain considerations) resulting in zero-voltage, zero  $dv/dt$  switching requires nu-

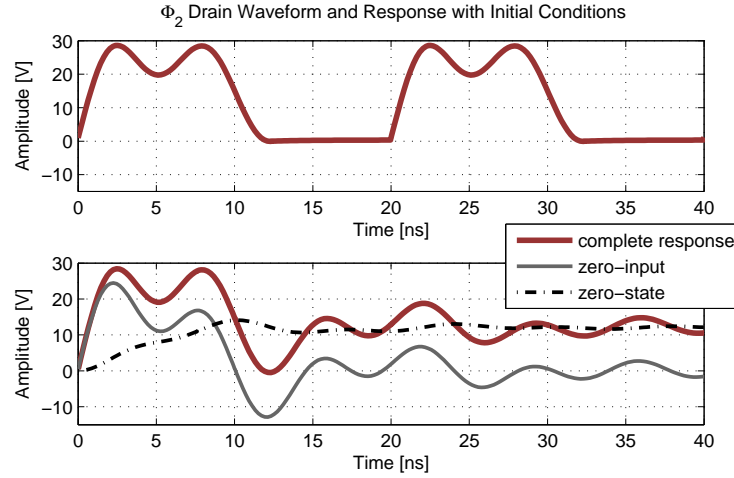


Figure 2.11:  $\Phi_2$  network complete response generated by capturing the initial conditions of each state variable in the circuit of fig 2.6 just before the switch opens. The waveforms are identical over the period the switch is off. Just before departure, the switch closes, reestablishing the initial conditions for the next cycle. Component values and simulation files can be found in appendix A

merical simulation. Great flexibility results from the many tuning solutions given a desired output power, switching frequency, and duty ratio. For instance, selecting the appropriate impedance curve and duty ratio adjusts peak voltage. Aside from allowing the use of lower-voltage processes, the RMS values of switch conduction and displacement currents change. Depending on the particular switch process, geometry, and switching frequency this is a significant tradeoff. Likewise, where inductor values are concerned, a range of characteristic impedances are achievable, and for a given load selection of these components influences efficiency. In fact, assuming a fixed inductor  $Q$ , load, and switch, an optimum characteristic impedance exists. Yet another factor, transient performance, is related to total energy storage.

In a real inverter, the switch non-linearities complicate tuning, pushing an exact solution ever further from reach. While a blind parameter sweep in SPICE will arrive at a working design, a more informed method is desirable. The approach taken here is to tune the inverter to a rough operating point using its impedance characteristics. The final design, when nonlinear elements are included, is achieved by tweaking component values based on a knowledge of the their specific impact on inverter behavior.

### 2.2.2 Tuning the $\Phi_2$ Inverter

Inverter tuning begins with the notion of approximate half-wave symmetry. While the  $\Phi_2$  input network of fig. 2.5(a) can be tuned to have peak immitances at the first three harmonics, this does not result in zero voltage switching. The presence of higher frequency harmonics, both even and odd, requires adjustment to the network in order to achieve ZVS. The load also affects tuning making the total drain-source impedance,  $Z_{AB}$ , from fig. 2.10(b) the parameter of interest. By controlling this impedance it is possible to tune the inverter over a wide range of operating points.

With a drain voltage signal that is necessarily periodic, the continuum of  $Z_{AB}$  can be largely ignored for tuning purposes. Rather, in as much as the drain voltage and switch current can be represented as Fourier series, the discrete points at each harmonic determine inverter operation. Thus the network need not have modal frequencies at the harmonics. Instead, the magnitude and phase of the network impedance at each harmonic, and more specifically at the fundamental and third harmonics, determine the operational characteristics. This assumes that there is a zero at the second harmonic. While it is possible to achieve ZVS and zero  $dv/dt$  when the zero is only *near* the second harmonic, it is not necessarily desired. Over the range of tuning points explored, pinning the second harmonic with a zero obtains the lowest peak voltages for a given RMS conduction current proving beneficial to efficiency.

It is useful to think of the drain waveform as its Fourier series. Temporarily ignoring higher frequencies, and remembering that the drain voltage should have no second harmonic component, the signal is composed of a fundamental and its third harmonic along with a dc offset equal to  $V_{IN}$ . The shape is strictly related to the magnitudes and phases of just these two components. In the top plot of fig. 2.12 a simulated  $\Phi_2$  drain waveform is compared with the sum of its fundamental and third harmonics. It is evident that while not exact, the approximation is reasonable. Immediately below, a series of signals constructed with the fundamental and its third harmonic component with zero phase offset is plotted. For each curve, the magnitude of the third harmonic has been varied resulting in larger peaks as the ratio of the third harmonic component increases. If these curves were to represent  $\Phi_2$  drain waveforms, the switch should be on between the close trough-pairs and off between the more distant pairs, as depicted by the notional gate waveforms. This implies that the required duty ratio (for ZVS) and the ratio between the fundamental and its third harmonic is related, a reasonable result. If the drain waveform was purely fundamental the required duty ratio would

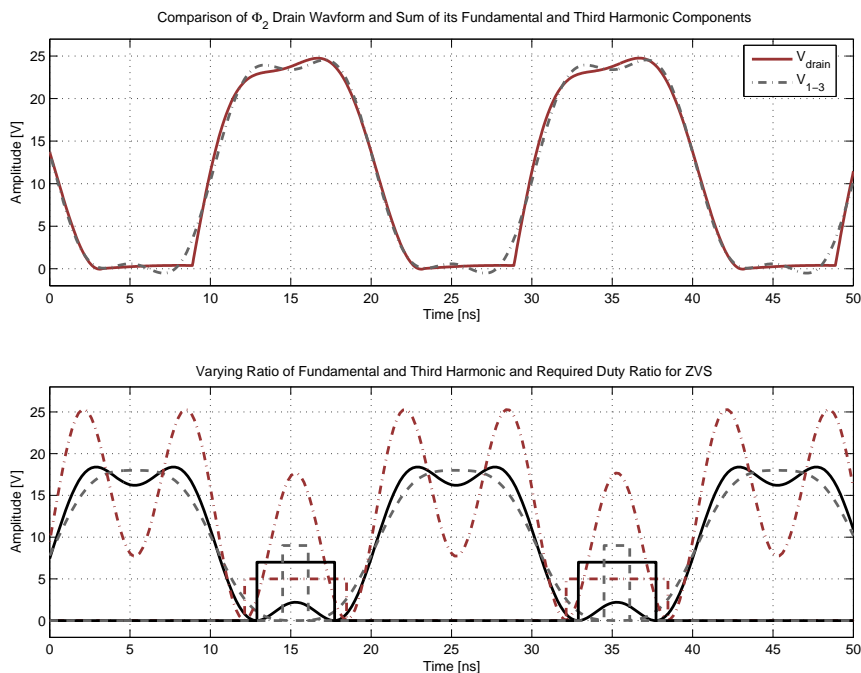


Figure 2.12: The  $\Phi_2$  inverter drain waveform is primarily composed of a fundamental and its third harmonic component as evidenced by the close match in the top plot. The ratio of these components partially determines the duty ratio necessary to achieve ZVS; waveforms with less third harmonic require a lower duty ratio. The pulse trains represent the necessary switching function, the actual value is affected by the presence of higher frequency components, but still follows the general trend.

be zero. For a drain waveform of purely third harmonic the duty ratio is close to 66%. These extremes are not desirable. Achievable duty ratios range perhaps from 0.2 - 0.5. Within this range we find acceptable ZVS operation and gate drive requirements that are not too severe.

The duty ratio is not solely related to the magnitudes of the harmonics, phase offset (primarily between the fundamental and third harmonics) plays a role. Though it adds another degree of freedom, keeping the phase offset near zero results in the lowest peak voltage and more symmetrical waveforms. Higher frequency components in the drain waveform also complicate matters. Clearly the construction of fig. 2.12 does not have ZVS when just the first three harmonics are considered. It is possible, however, to achieve ZVS by an appropriate adjustment to the network impedance.

The resulting magnitude, phase offset, and duty ratio attain slightly different values than otherwise predicted. These values may be divined in a numerical simulator like SPICE and remain valid at various values of characteristic impedance<sup>2</sup>, a fact useful when optimizing efficiency, for instance.

Tuning the  $\Phi_2$  inverter brings to light an array of possible tuning points. Here we consider two main aspects related to the shape of the drain voltage waveform and the drain-source impedance. First, depending on the component values selected, the peak drain voltage can range from just under  $2 \cdot V_{IN}$  to greater than  $4 \cdot V_{IN}$ . The “peakiness” is a very important factor where device breakdown is concerned. In particular, integrated devices tend to have lower breakdown voltages than discrete components, and a factor of two in peak voltage can determine whether or not a design is achievable in a given process. The other issue of primary importance is the characteristic impedance of the network. This can be adjusted up or down within a range while the peak voltage remains constant. The effect is to change the damping of the network. In so doing the resonating losses change, typically reaching a minimum and then increasing as characteristic impedance is further decreased. Component values also change significantly, inductors shrink and capacitors get larger as impedance is lowered. This can be exploited in co-packaging or integrated environments where volume is at a premium. Since capacitors scale better than inductors in terms of Q, trading higher Q capacitance for lower Q inductance is often advantageous where very small size is desired.

Turning first to the question of peakiness highlights a useful relationship mentioned earlier. That is, the peak drain voltage is largely determined by the ratio of the fundamental and third harmonic magnitudes. The more third harmonic present in the drain voltage waveform, the higher the peak voltage for a given  $V_{IN}$ . In turn, the voltage magnitude ratio is roughly dependent on the drain-source impedance magnitude ratio,  $Z_{AB}$ , at the respective harmonics. Lowering the impedance at the third harmonic relative to the fundamental decreases the peak drain voltage because the impedance decreases faster than the rising drive currents. Further, the impedance relationships among the harmonics are deterministic. If the phase at the fundamental and the magnitude ratio between the fundamental and its third harmonic are held

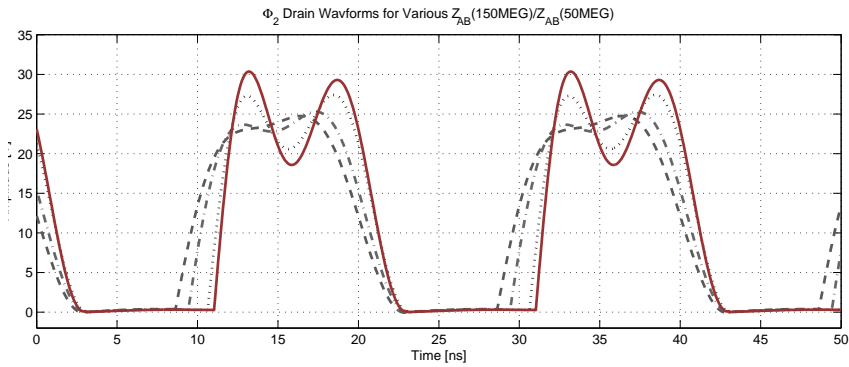
---

<sup>2</sup>The term characteristic impedance is used somewhat loosely here, being only strictly defined for a second order system. In general, in this section it refers to shifting the impedance magnitude up or down, usually by picking the characteristic impedance of the second harmonic leg—where it *is* well defined—and then reestablishing the magnitude-phase relationships at the fundamental and third harmonics necessary for ZVS.

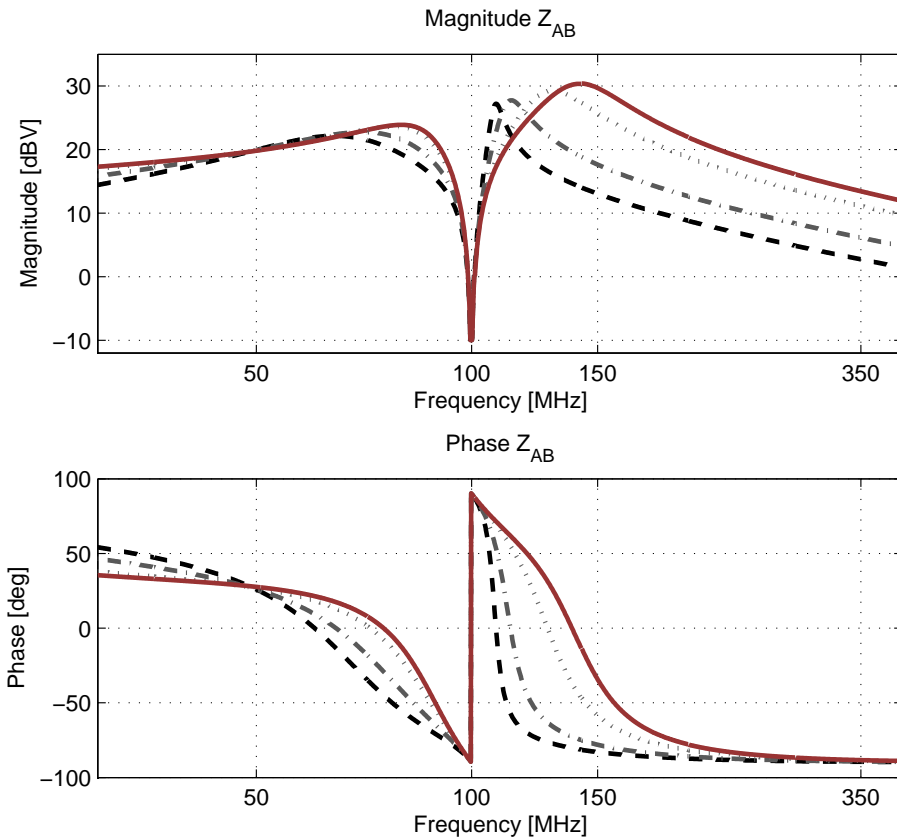
constant, the converter will exhibit the same drain waveform characteristics (i.e. peak voltage and overall shape) for a given duty ratio. It is here that a potential design algorithm begins to emerge. If a set of magnitudes and phases are known that yield acceptable ZVS operation, an impedance curve can be fit that produces a functional converter. While numerical simulation is still required to derive a given set of values, it is rather straight forward to subsequently walk along the locus of solutions and achieve flatter and flatter waveforms. This is precisely the result presented in figure 2.13. After a favorable tuning point is found the converter can be re-tuned by varying only two components,  $L_F$  and  $C_F$ . This does not imply that the other components cannot be varied, rather varying  $L_F$  and  $C_F$  is an effective means of tracing out solutions that achieve different ratios of fundamental and third harmonic.

The procedure is demonstrated in fig. 2.14 starting with a tuned inverter at the top left and proceeding clockwise. The waveform in the first plot exhibits ZVS and zero  $dv/dt$  characteristics. In the second plot, the capacitor,  $C_F$  has been decreased significantly to increase the level of third harmonic.  $L_F$  is then subsequently increased until the drain waveform just reaches zero  $dv/dt$  at zero voltage. In the final plot, the duty ratio has been adjusted (and some slight iteration performed) to get ZVS, zero  $dv/dt$  waveforms. The component values and impedance curve that realize the resulting drain waveform are by no means unique. However, the impedance phase at the fundamental and magnitude ratio between the fundamental and third harmonic along with the duty ratio constitute a set of values that when reproduced result in a properly tuned  $\Phi_2$  inverter. This remains true even as the balance of the impedance curve varies over a wide range. As much is shown in the plots of fig. 2.15. Starting with a tuned inverter, the characteristic impedance of the second harmonic tank is varied. Adjusting  $C_F$  and  $L_F$  reestablishes the desired impedance conditions. The result is a set of identical drain waveforms delivering constant power to the load, yet with a circuit that has widely differing component values.

That constant load power is achieved should come as no surprise. For a given drain voltage the current in the load leg (formed by  $L_R$ ,  $R_L$ , and  $C_R$ ) is fixed. It was demonstrated in [19] that when the drain waveform is known, the power may be estimated by assuming most is delivered at the fundamental. Further approximating the drain as a square wave gives a reasonable estimate of the fundamental amplitude. The load power may then be directly calculated. Changing the load to modulate power, however, necessarily affects  $Z_{AB}$ , ruining ZVS. Retuning then affects the desired load power and iteration is necessary. This dependency can be unwound by using the impedance transfer function (eqn. 2.2) to calculate the required component changes.



(a)  $\Phi_2$  drain waveforms obtained at different impedances



(b)  $\Phi_2$  drain source impedance,  $Z_{AB}$ , realizing waveforms of fig. (a)

Figure 2.13: The drain-source impedance controls the magnitude of fundamental and third harmonic that appears in the drain voltage waveform. Lower drain-source impedance,  $Z_{AB}$  at the third harmonic relative to the fundamental results in flatter waveforms. This is useful in meeting peak voltage stress requirements and minimizing loss. Component values and simulation files may be found in appendix A

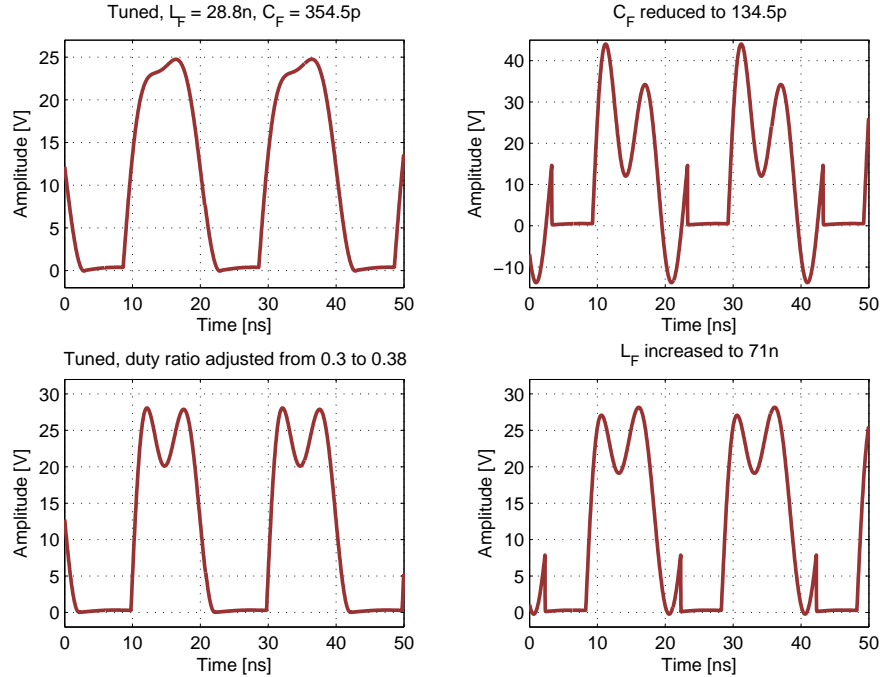


Figure 2.14: **Tuning sequence to increase drain waveform third harmonic component and reduce overall circulating currents. Component values and simulation files may be found in appendix A**

Here a brute-force MATLAB script was used to solve for new component values. By holding the phase angle at the fundamental constant, along with the magnitude ratio between the fundamental and third harmonic, the drain voltage does not change. This leads to a quick method to change the output power of an existing inverter design that avoids iteration. For example, for an existing design, the inductor  $L_R$  was first decreased from  $14.1nH$  to  $10nH$  to increase output power from  $9.5W$  to  $10.8W$ . This change can be calculated a priori given the identical drain voltage. When the new values for  $C_F$  and  $L_F$  ( $440pF$  to  $497.7pF$  and  $21.5nH$  to  $17.343nH$  respectively) are inserted in the circuit, the impedance and drain waveforms are as in fig. 2.16. In the event that a large increase in power is required, the characteristic impedance must be lowered. This adds an additional step to the process, but iteration can be avoided if the load impedance is first compared to the drain-source transfer function. As long as the impedance at the second harmonic is significantly lower than the impedance of the load branch (at least  $20dB$ ), retuning can be accomplished as described above.



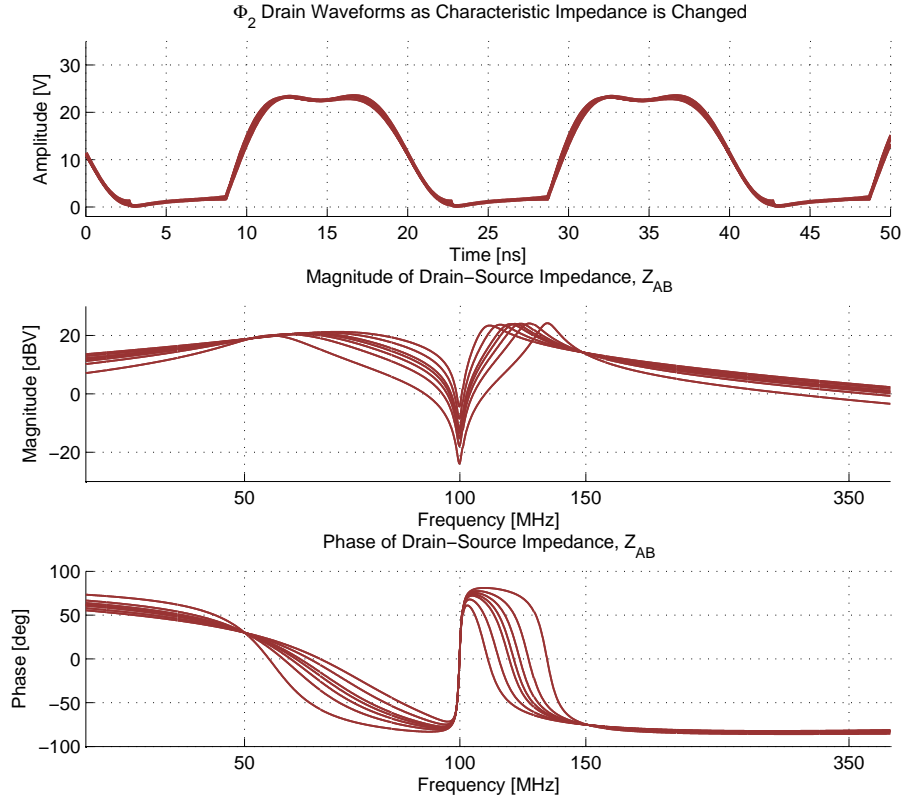


Figure 2.15: Holding the constant the phase at the fundamental and the magnitude ratio between the fundamental and its third harmonic allows characteristic impedance to be changed without changing output power. In this case it varies from  $5\Omega$  to  $50\Omega$ . The component values and simulation files may be found in appendix A

$$\begin{aligned}
 Z_{AB} &= \frac{num}{den} & (2.2) \\
 num &= L_F L_{2F} L_R C_{2F} s^4 + L_F L_{2F} C_{2F} R_L s^3 + L_F L_R s^2 + L_F R_L s \\
 den &= L_F L_{2F} L_R C_F C_{2F} s^5 + L_F L_R C_F C_{2F} R_L s^4 + \\
 &\quad (L_F L_{2F} C_{2F} + L_R (L_F C_F + L_F C_{2F} + L_{2F} C_{2F})) s^3 + \\
 &\quad R_L (L_F C_F + L_F C_{2F} + L_{2F} C_{2F}) s^2 + (L_F L_R) s + R_L
 \end{aligned}$$

Directly calculating component values to achieve certain impedance goals extends

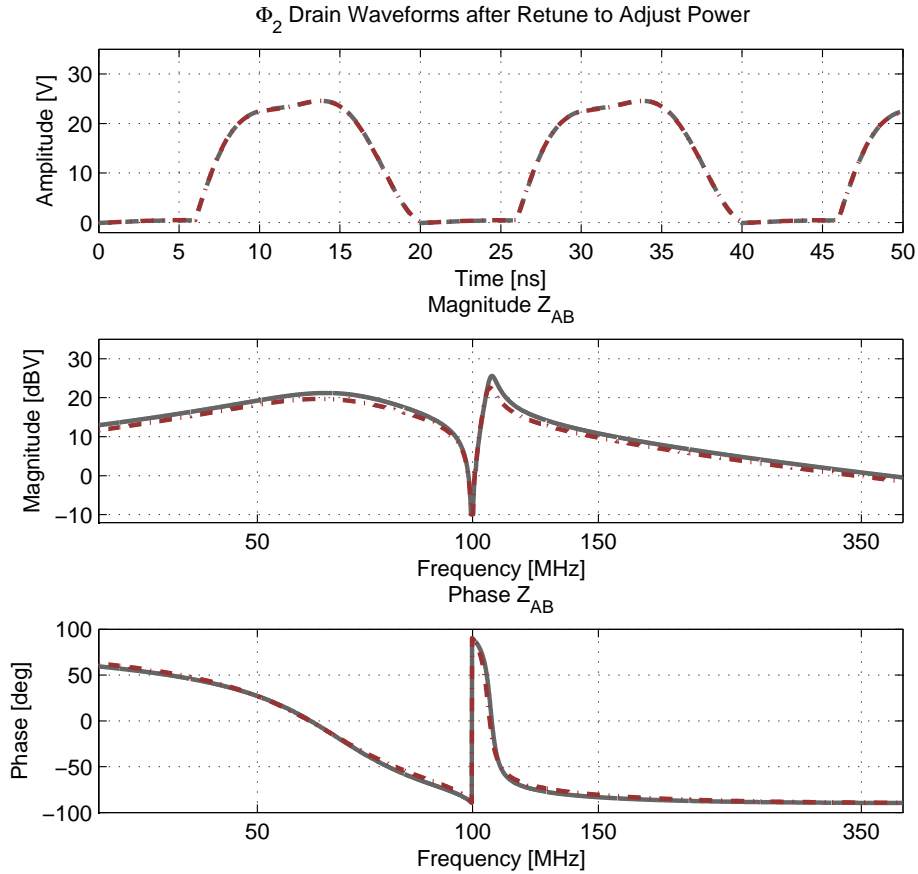


Figure 2.16: Once an operating point is established, power may be controlled by adjusting  $L_R$  using the established drain voltage,  $V_{drain}$ . New values of  $L_F$  and  $C_F$  that are calculated using the open-switch drain source transfer function,  $Z_{AB}$ . The calculation in this case was performed with a MATLAB script that holds constant the phase angle at the fundamental and the magnitude ratio between the fundamental and third harmonics. The resulting identical drain waveform decouples power adjustment and tuning. Here power was increased from  $9.5W$  to  $10.8W$ . For large power increases, the characteristic impedance will need to be lowered.

to other tuning aspects, as well. For instance, the characteristic impedance as was changed in fig. 2.15 this way. First, the characteristic impedance of the second harmonic tank, formed by  $L_{2F}$  and  $C_{2F}$  is raised or lowered, then values of  $L_F$  and  $C_F$  are directly calculated. Since the salient impedance relationships are maintained, the drain waveform stays constant. The utility of such a method is evident—once a working tuning point is known an entire range may be quickly achieved. This gives the  $\Phi_2$  converter a great deal of flexibility in meeting the requirements of a particular design.

The ability to move about the  $\Phi_2$  design space with relative ease, surfaces the question, “Where to go?” In power conversion, in general, and the co-packaged/integrated space, in particular, there are ready compasses. As mentioned earlier, device breakdown voltage is a significant consideration with a resonant topology. Discrete transistors in silicon are available with breakdown voltages of many hundreds of volts<sup>3</sup>. For integrated power processes breakdown voltages above 100V are available, but 50V is closer to the norm. This can be a problem with resonant converters depending on the application. For instance, the “automotive” voltage range is generally considered to be 8-18V. An ideal class E inverter operating over this range will have a peak drain voltage ranging up to 65V, well beyond the typical 50V headroom in a common power process. In contrast, an ideal  $\Phi_2$  inverter tuned to minimize voltage stress has a peak voltage of roughly  $2 \cdot V_{IN}$ , in this case 36V. The practical implementations presented in chap. 3 have realized a factor of 2.5, for a peak voltage of about 45V in the automotive range, still comfortably within the breakdown limits.

The tradeoff associated with varying the peakiness of the drain waveform is complicated by the various converter loss mechanisms. Inductor and capacitor  $Q$  determines an effective resistance which is used to compute loss. That  $Q$  varies with frequency is significant, but the inductors in the  $\Phi_2$  inverter tend to have a dominant frequency component. In the case of  $L_F$  and  $L_R$  the  $Q$  is computed at the fundamental and  $L_{2F}$  is evaluated at the second harmonic. Generally passive losses of significance are constrained to inductors, capacitor  $Q$  being typically more than an order of magnitude better. Yet, the device capacitance,  $C_{OSS}$ , retains significance to inverter loss. A relatively high equivalent series resistance,  $R_{OSS}$ , confers a  $Q$  on par with the inductors.

---

<sup>3</sup>Generally the device on-state resistance goes up as some power factor of the blocking voltage, so in terms of conduction loss it can be advantageous to have lower peak voltage stress

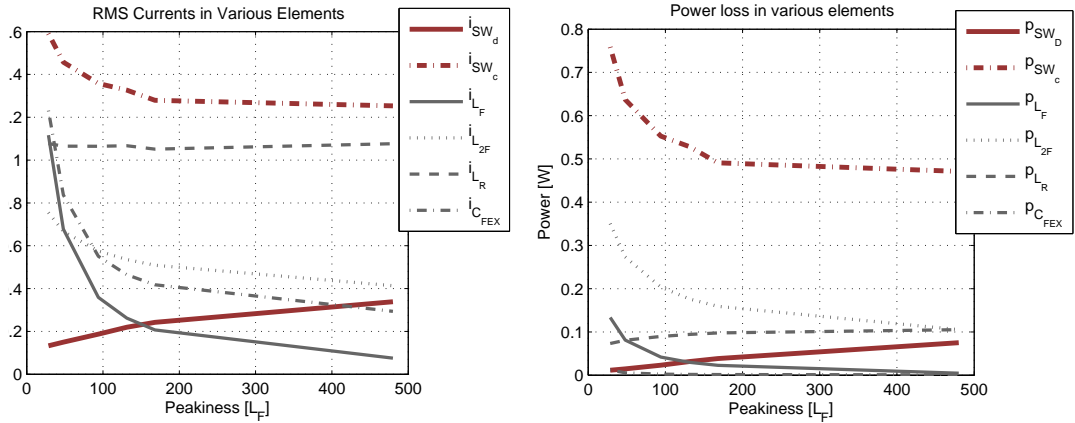


Figure 2.17: **Sharply rising RMS currents as  $Z_o$  is decreased increase overall loss. Switch displacement current,  $i_{SW_d}$  increases for peakier waveforms, but this is outstripped by falling conduction current loss. Component values may be found in appendix A**

Since  $C_{OSS}$  sees the drain voltage during operation, its current is therein uniquely determined. A peakier drain voltage will have a higher RMS current both because of its additional excursion and higher  $dv/dt$ . This becomes an important consideration in light of  $R_{OSS}$ . While this loss is minimized by favoring the flatter curves of fig. 2.13, it may not be the best choice to optimize overall inverter efficiency. The plots of fig. 2.17 suggest as much. The currents and losses are plotted vs. the value of  $L_F$ , of which large values result in more peaky waveforms (for a given characteristic impedance at the second harmonic). We see that the RMS currents in the inverter *increase* for flatter drain voltage waveforms. This is not surprising when one considers how flatter waveforms are obtained. With output power held constant, the shunt capacitance  $C_F$  must increase while  $L_F$  and the duty ratio decrease to maintain ZVS. Both increasing the capacitance and reducing the inductance lower impedance in their respective branches and contribute to larger circulating currents. Since the load power is held constant roughly by constraining the RMS current there, the additional circulating currents have only two places to go: the second harmonic tank and the switch. The increasing circulating current in the switch necessarily means that as the waveforms are flattened, switch conduction loss increases even as displacement loss diminishes. Though this suggests an optimum where the conduction and displacement losses cross, it may not occur in practice. If the displacement loss is significantly smaller than the conduction loss, often the case in practical devices when used in the  $\Phi_2$  inverter, then they may never overlap. In such a case, efficiency will continue to increase for ever peakier waveforms (see fig. 2.18) because the drop in switch conduction and passive

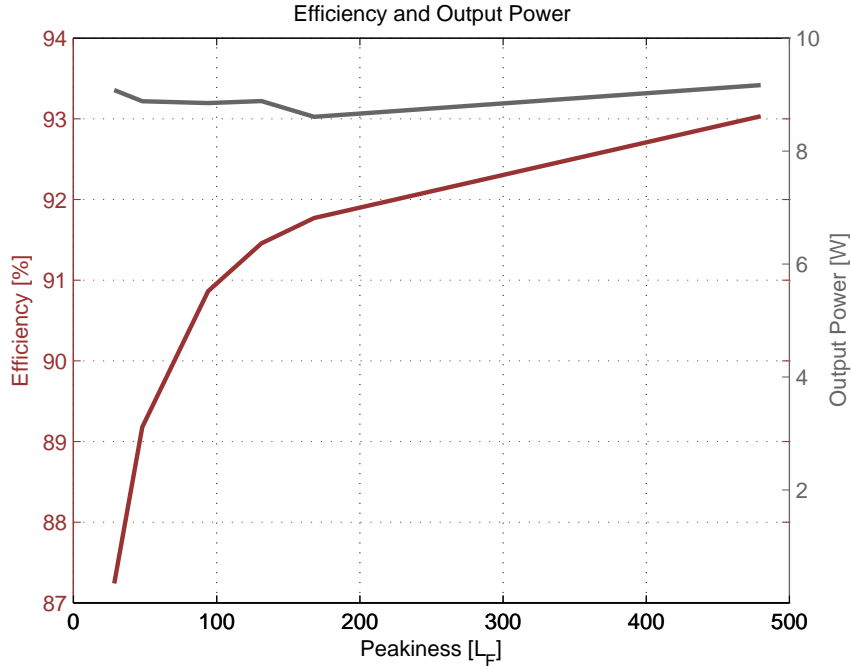


Figure 2.18: **With a fixed switch and constant output power, as the drain waveforms get peakier, the RMS conduction current and associated losses decrease. This contributes to a rising efficiency. If a switch is used at a high enough frequency, or has an unusually high  $R_{OSS}$  an optimum could occur.**

component losses outweigh the increasing displacement loss.

The above discussion leaves out a number of factors that influence the optimum tuning point. To begin with, since peakier waveforms go along with increasing  $L_F$ , operating the inverter in that regime degrades its transient response (see fig. 2.19. This is of particular concern in light of the intended control strategy. Modulating the entire power stage relies on fast transient response to hold modulation losses and bulk energy storage requirements at bay (this will be discussed in some detail in chap. 5). Another important factor is switching frequency. As the frequency increases a given switch will have greater displacement loss, reflecting the fact that a growing portion of  $C_F$  is being substituted with low- $Q$  device capacitance. Under either of these considerations, and depending on the relative magnitude of  $R_{DS-ON}$  and  $R_{OSS} \cdot C_{OSS}^2$ , the optimum point may be different. Further, flatter waveforms require smaller duty ratios, a concern for gate drive design (chap. 5). At VHF frequencies resonant gate drives tend to provide the lowest loss, but most sinusoidal schemes suffer a performance hit for non-50% duty ratios. Other schemes have limited ability

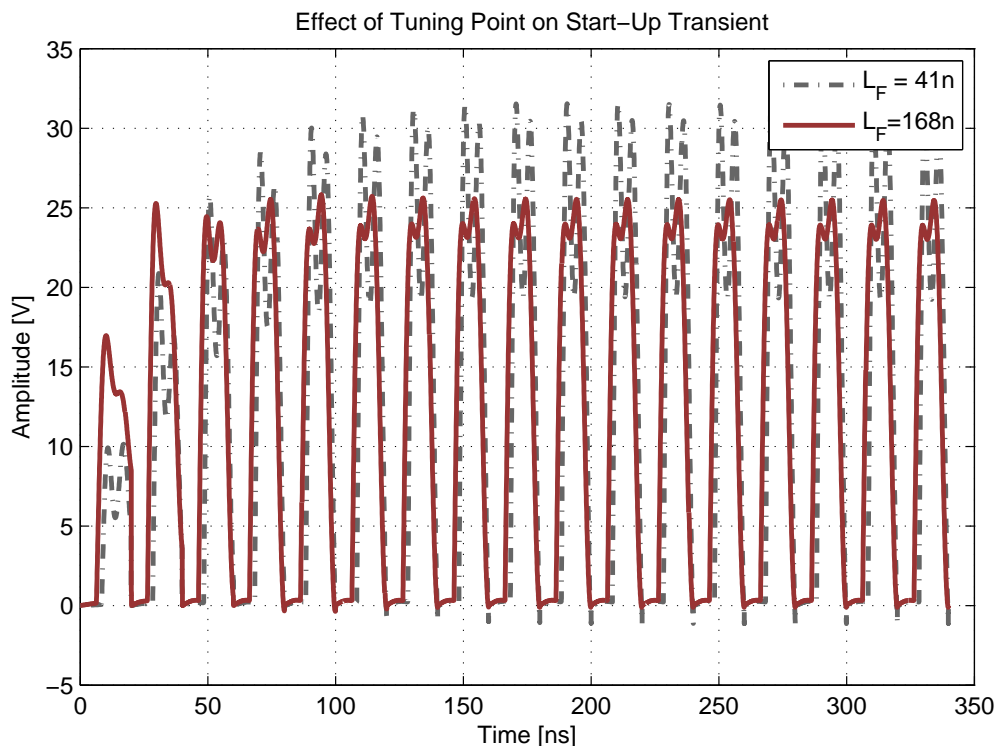


Figure 2.19: Achieving peaky drain waveforms tends to require a large inductor  $L_F$ , slowing the start-up transient. Here  $L_F$  is changed from  $168\text{nH}$  to  $41\text{nH}$  resulting in a faster response. Component values and simulation files may be found in appendix A

to realize a wide range of duty ratios.

Monolithic devices available in an integrated implementation add another degree of freedom. Device geometry influences the distribution of parasitic elements important to loss, but a more direct tradeoff comes from scaling device area. As area is scaled up,  $R_{DS-ON}$  and  $R_{OSS}$  decrease as  $C_{OSS}$  increases. Different than scaling frequency for a fixed device, substituting device capacitance for  $C_F$  now purchases a lower  $R_{DS-ON}$ . If  $R_{OSS}$  drops linearly with area, then as area doubles displacement loss will double. This applies so long as  $C_{OSS}$  is being substituted for discrete capacitance. Conduction loss halves, on the other hand, and total switch loss will arrive at a minimum when both losses are equal. The minimum device loss in this case is for a *given* peakiness. The lowest total loss will still lie where the circulating currents are least, which occurs as the drain waveform becomes more peaky.

In the situation where device capacitance is not replacing external shunt capacitance, the ratio of third harmonic to fundamental will decrease (assuming, as above, that the characteristic impedance of the second harmonic tank is held constant). Therefore displacement loss increases even more slowly, but conduction loss may rise or fall. This depends on whether the incremental reduction in  $R_{DS-ON}$  outweighs the *square* of the increase in conduction current that resulted from the flatter waveforms. If conduction loss does fall, higher efficiency is obtained for less peaky waveforms (i.e. with lower peak voltage than the device breakdown voltage, for instance). For the very peaky tuning points, increasing the device area results in both lower peaks and less total loss. However, the rise in RMS conduction current eventually outstrips the increase in area, and efficiency will fall.

Characteristic impedance provides another means of optimization. For a given output power, changing the characteristic impedance affects the stored energy. This in turn reflects how much loss can be expected from passive components of a given  $Q$ . Using the techniques described above on a  $\Phi_2$  inverter allowed the characteristic impedance to be adjusted from  $5\Omega$  to  $50\Omega$ . In the left-hand plot of figure 2.20 the loss breakdown vs. characteristic impedance is presented. As characteristic impedance increases, the loss in inductor  $L_F$  falls sharply. It then settles into a gradual taper contrasting the behavior of  $L_{2F}$ 's loss. This rise results as  $L_{2F}$  increases in value and its parasitic resistance follows suit. The increase is enough to offset the falling current and results in an optimum efficiency (this would not necessarily be the case if an inductor of sufficiently high  $Q$  was available, but in the VHF regime typical air-core inductor  $Q$ s are around 100). Notice that with nearly identical drain waveforms the switch displacement losses do not change. Similarly, the power dissipated in  $L_R$  also remains constant as its value,  $16.1nH$ , and the load current are identical at each tuning point. The right-hand graph in fig 2.20 offers another view of the system. The right hand axis plots the circulating energy and the left hand axis efficiency. We see that the efficiency peaks close to the point where the circulating energy is a minimum as a result of falling passive losses and lower RMS conduction currents.

The flexibility of the  $\Phi_2$  inverter leads to a bewildering array of design tradeoffs. Arriving at a cut and dried procedure that always hits the best efficiency or any other design metric is unlikely. There are, however, some basic procedures that can help along the way, and these are enumerated below.

1. Constrain input voltage and output power

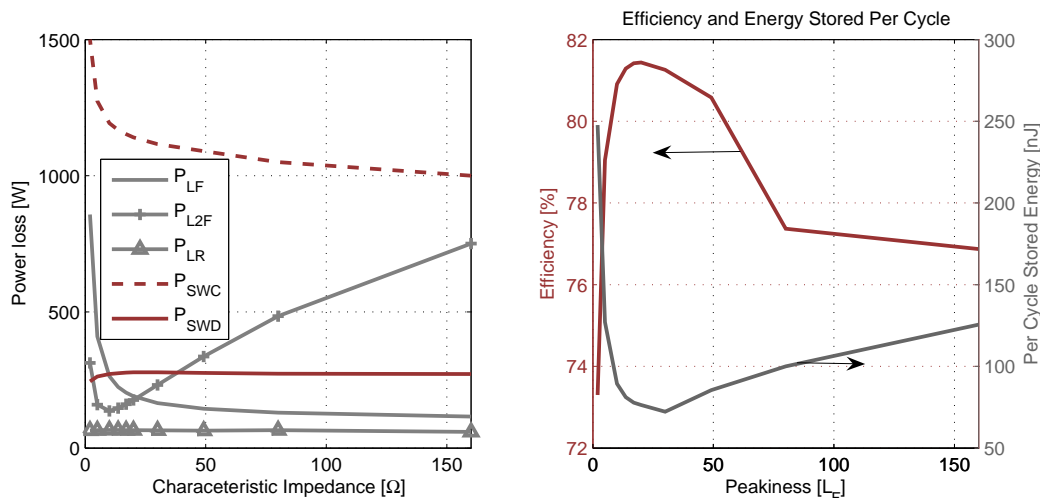


Figure 2.20: The left plot shows the most significant losses in the  $\Phi_2$  inverter. Assumed inductor  $Q$  is 80,  $R_{DS-ON} = 0.4$ , and  $R_{OSS} = 0.8$ . Losses in  $L_{2F}$  dominate for high characteristic impedance,  $L_F$  losses at low  $Z_o$ . The result is the maximum in efficiency shown at the right, which corresponds to the least stored energy.

2. Assume the drain voltage may be modeled as a square wave of amplitude  $\frac{4}{\pi}2V_{IN}$
3. Determine the equivalent load resistance (finding an equivalent load resistance for a resonant rectifier is discussed in chap. 3)
4. Calculate the necessary value of  $L_R$  to arrive at the desired output power
5. Select a characteristic impedance of the second harmonic tank that ensures the zero is much lower than the load impedance and the impedances at the fundamental and third harmonic (at least  $20dB$ )
6. Starting with the switch capacitance, tune  $L_F$  to achieve a desired fundamental and third harmonic phase and magnitude, or calculate a value with the transfer function using predetermined phase and magnitude relationships
7. Adjust  $L_F$  and  $C_F$  (i.e. extra shunt capacitance) to find optimum efficiency, transient performance, or physical size. Note  $C_F$  may be adjusted by increasing device area when possible.
8. Output power may be readjusted by appropriately changing  $L_R$  and calculating new values of  $L_F$  and  $C_F$  using the transfer function



9. Adjust the characteristic impedance of the network for efficiency and component size
10. Iterate as necessary

### 2.2.3 Nonlinear Capacitance Effects on the $\Phi_2$ Inverter

The device capacitance  $C_{OSS}$  is inherently nonlinear. It is primarily composed of a reverse biased PN-junction capacitance that can be roughly modeled as eqn. 2.3

$$C_{OSS}(V) = \frac{C_{JO}}{\left(1 + \frac{V}{\Phi_{bi}}\right)^M} \quad (2.3)$$

where  $C_{JO}$  is the zero bias capacitance,  $\Phi_{bi}$  is the built in voltage,  $V$  is the reverse bias voltage, and  $M$  is the grading coefficient. Since  $C_{OSS}$  is a function of the reverse bias, the behavior of the  $\Phi_2$  inverter now depends on input voltage. As the input voltage increases, the switch capacitance drops. This changes the inverter tuning. However, the effect is not necessarily severe and  $C_{OSS}$  can be approximated for design purposes as its value at  $V_{IN}$ . Adjusting component values (usually just  $L_F$  and  $C_F$ ) is enough to achieve ZVS. Since the inverter will only have perfect ZVS at one input voltage, the tradeoff for maximum efficiency becomes more complicated. The specific effects of the nonlinear capacitance in this regard are difficult to predict, and simulation is necessary to determine the best operating point for a particular application. Figure 2.21 shows drain waveforms for a  $\Phi_2$  inverter that includes a full nonlinear capacitance model. As the input voltage is varied, ZVS is not perfectly maintained, but the effect on efficiency is only moderate. The effects of non-linear capacitance are dealt with more extensively in the dc-dc converter discussions in a later chapter.

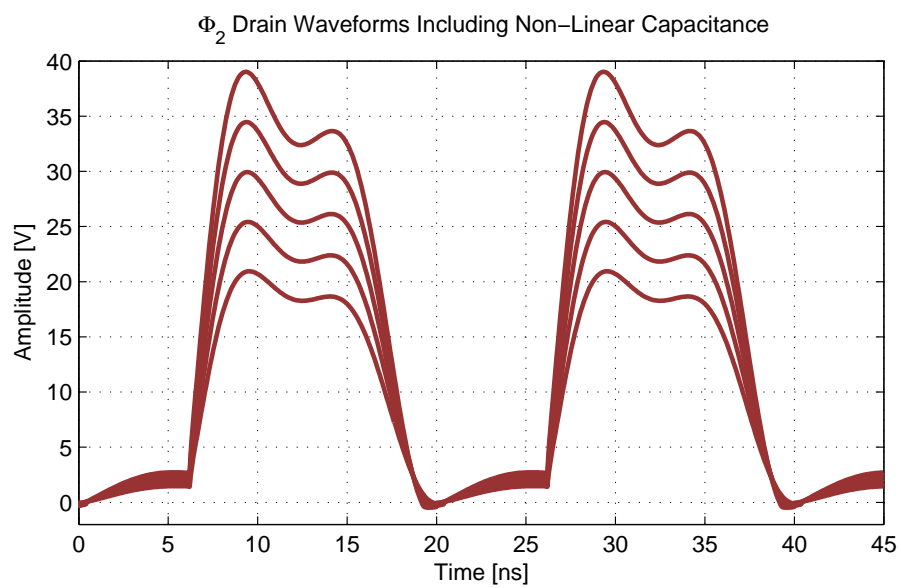


Figure 2.21: The  $\Phi_2$  inverter waveforms shown here were generated with a model including a non-linear drain capacitance. As  $V_{IN}$  is varied, ZVS is not perfectly maintained, but overall efficiency remains roughly constant.

## *The $\Phi_2$ dc-dc Converter*

---

WHILE there are many possible applications for the  $\Phi_2$  inverter, dc-dc conversion is of interest here. Such a scheme requires a suitable means of transformation and rectification as well as regulation of the output. Rectification may take a number of forms, but a practical scheme demands efficiency, low component count, and small size, particularly where the potential for integration is desired. To this end, a resonant rectifier is employed composed of just three components which replace the output tank of the inverter. The resulting resonant dc-dc power stage, under appropriate control, yields efficient operation into the VHF regime. This particular architecture of RF inverter, transformation stage, resonant rectifier was first proposed in [11].

Appropriate control at VHF does not usually include a classic PWM scheme that modulates the switches directly. To begin with, the operation of the  $\Phi_2$  inverter is intimately bound with the duty ratio. As discussed in chapter 2, high efficiency operation occurs only over a very narrow range of duty ratios. Similarly, methods of frequency control often practiced for resonant RF schemes spoil the dynamics as well as the efficiency when control over a wide range is desired. Instead, on/off modulation is relied upon to regulate the output [30, 18, 17]. This technique takes advantage of the excellent transient response of the  $\Phi_2$  converter, a trait gained through VHF operation and minimalist energy storage. Not to be ignored, a classic hard-gating scheme at VHF could be expected to dissipate energy at power levels measured in watts. Where the desired output power is in the range of 10-20W, a more efficient gate drive is in order. It must also include fast start-up and shut-down to fully exploit the benefits of on/off modulation. Such a design is presented in the pages to follow along with a host of ancillary considerations necessary to realize a  $\Phi_2$  dc-dc converter.

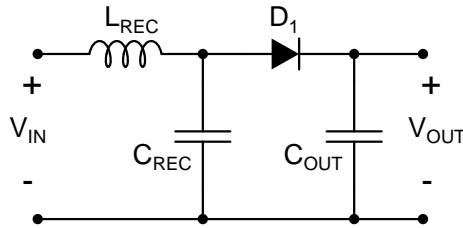


Figure 3.1: The “series-loaded” resonant rectifier.

### 3.1 A Resonant Rectifier

Classic hard-switched (square wave) rectifiers do not scale well in frequency. Finite commutation time and reverse recovery (when diodes are the rectifying element) amount to untenable switching loss. In addition, resonances among parasitic junction capacitance and package inductances are easily excited by the harmonic rich content of a square wave rectifier voltage. Since the parasitic elements are lossy in nature, particularly with rising frequency, the energy dumped into the oscillations counts against rectifier efficiency [28]. Damping legs that work well at lower frequencies to suppress these oscillations are even worse for loss as frequency increases.

A number of resonant rectification schemes have been proposed over the years [28, 11]. For instance, the class-e inverter can be used as a rectifier by replacing the switch with a diode and interchanging the load resistance and source voltage. The result is the time-reversed dual circuit in which power flows in the opposite direction, i.e. from the ac-port to the dc-port, a rectifier. Many variations exist on this theme including full-wave resonant rectifiers and dual output schemes. The particular scheme of interest here was introduced as the “series-loaded” resonant rectifier in [28]. In that presentation a parallel resonant tank was used across the input as a harmonic trap. Here, the tank is dispensed with as the filtering from the combination of the series inductor  $L_{REC}$  and the shunt capacitance  $C_F$  prove adequate. The result is the simple rectifier appearing in figure 3.1.

In chapter 2 the point was made that in the  $\Phi_2$  inverter the lion’s share of the power delivered to the load is at the fundamental. The expected load power is then found by approximating the drain voltage as a square wave and calculating the fundamental amplitude. This method sized the inductor,  $L_R$ , in light of the load resistance,  $R_L$ . Here, we can approximate an appropriately tuned rectifier as the load resistance  $R_L$  and use the same technique. To this end, it is useful to consider the relationship

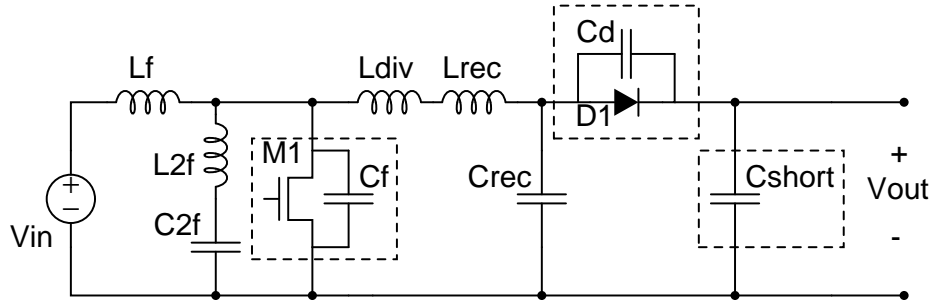


Figure 3.2: The  $\Phi_2$  resonant boost converter.

between the fundamental of the drain voltage and the fundamental of the rectifier current, as these determine the equivalent resistance in a describing function sense.

There is, however, a notable exception to this approach. Figure 3.2 shows the interconnection of the  $\Phi_2$  inverter and the series-loaded rectifier. The output tank of the inverter is replaced by the rectifier which is connected across the drain-source terminals of the switch. It should be apparent that this interconnection provides a dc path from the source to the load in addition to carrying ac power from the inverter. Two important results arise from the existence of the dc path. First, the dc-dc converter as shown is a resonant dc-dc *boost* converter. The output voltage cannot drop below  $V_{IN}$  less a diode drop. Second, the portion of the power delivered at dc avoids the loss mechanisms associated with resonant transfer. Instead, it is subject to parasitic dc resistance, often much lower than the ac loss mechanisms. In terms of establishing converter output power, the dc and ac portions may be treated as roughly orthogonal for design purposes. Equation 3.1 arises from basic conservation of energy considerations and is useful in this regard.

$$\frac{P_{AC}}{P_{DC}} = \frac{V_{OUT}}{V_{IN}} - 1 \quad (3.1)$$

It allows the determination of ac power when the total power and the conversion ratio are known (it also shows that the fraction of ac power increases with the boost ratio, as one would expect). Thus as a basic design procedure for the converter, one would first determine the conversion ratio and the output power. Then having computed the ac power from eqn. 3.1 the design proceeds by determining the equivalent resistance of the rectifier at the fundamental. When the inverter components are sized based on the equivalent resistance, connecting the two halves sees dc and ac power delivery

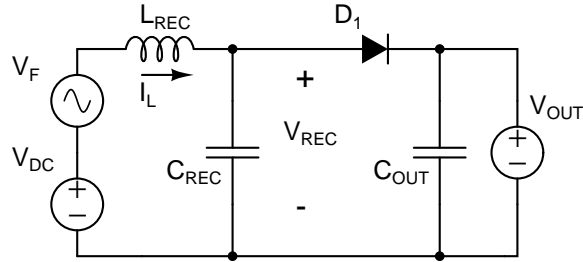


Figure 3.3: **The SPICE scheme for tuning the resonant rectifier**

roughly commensurate to the requirements of the designed total output power. Any deviation can be easily corrected in a final design iteration.

While dc and ac power can be treated separately for purposes of designing the converter as a whole, rectifier design is necessarily coupled to the dc level. The equivalent ac resistance is a function of the dc bias (i.e  $V_{OUT} - V_{IN}$ ) and the ac amplitude. Consider the rectifier in fig. 3.3, the ac input voltage is the fundamental of the drain voltage plus a dc bias as is produced by a  $\Phi_2$  inverter. The output is tied to a fixed voltage source of value  $V_{OUT}$ , accurately representing the situation when the output voltage is controlled via feedback. The time-domain results of a simulation in SPICE are presented in fig. 3.4. The top plot is the voltage at the inductor, capacitor, diode junction under periodic steady state. When the diode is on,  $V_{REC}$  is equal to the output voltage, when the diode is off,  $C_{REC}$  and  $L_{REC}$  ring until  $D_1$  again clamps  $V_{REC}$ . At turn-off there are two established initial conditions, the voltage across the capacitor equals  $V_{OUT}$  and the current in  $L_{REC}$  is zero (see the second plot). Thus, after switch turn-off,  $i_L$  is initially negative, reversing when the voltage on  $C_{REC}$  has reached its minimum.  $i_L$  then increases as  $L_{REC}$  absorbs the energy stored on the capacitor and additional energy from the source. Once  $V_{REC}$  rings up to  $V_{OUT}$  the diode again turns on and  $i_L$  is shunted to the load until it reaches zero and the cycle repeats. DC bias comes into play as it affects the magnitude of applied volt-seconds across  $L_{REC}$  when the diode is on. In general, when the bias is high, it will take longer for the inductor current to reach zero. The opposite is true of a low bias. The relationship however, is a complex one. The dc bias affects duty ratio and how much energy is stored in the tank each cycle. In turn, the shape of the load current changes affecting the amount of power delivered.

As it is difficult to establish a relationship among the many variables with an explicit solution, a more pragmatic approach to tuning is favored. By comparing the voltage and current fundamentals at the rectifier input port in SPICE, the ac power delivered

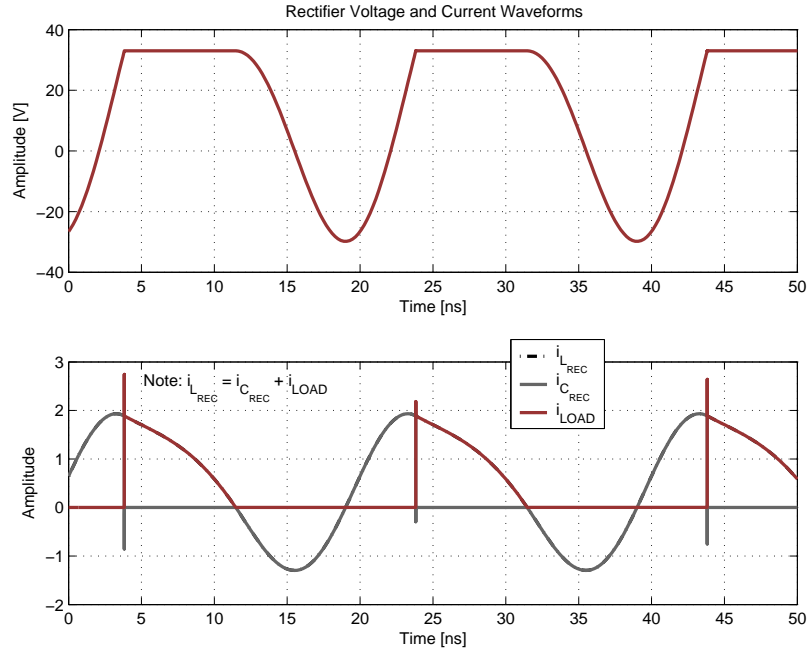


Figure 3.4: **Rectifier waveforms**

can be determined. The total power can be easily computed at the output port which also gives the dc power as the difference between the two. If the fundamental of the inverter voltage driving the rectifier can be assumed (i.e. the rectifier loads the inverter in the same manner as the output tank), the output power is determined on connection of the inverter and rectifier.

In order to make the assumption that the inverter voltage is a given, the rectifier equivalent resistance needs to be determined. As mentioned above, this is readily done by comparing the voltage and current at their fundamentals. If the rectifier in fig. 3.3 is driven with a sinusoid of the appropriate amplitude and dc bias, the voltage and current are in phase and the rectifier appears resistive. However, nonlinear circuit operation means that the relationship is not true everywhere. As the dc bias or the amplitude of the fundamental is increased the phase between the voltage and current fundamentals,  $\Theta_f$ , increases and the rectifier looks increasingly inductive. When  $V_{IN} = V_{OUT}$ ,  $\Theta_f = 90^\circ$  and all power is delivered at dc. This progression is illustrated in the plots of figure 3.5. The phase can also become capacitive if the bias or amplitude is reduced, but the voltage range over which this occurs is narrow. Further, capacitive operation is undesirable because the circulating currents for a given output power tend to be higher than inductive for phase, contributing to

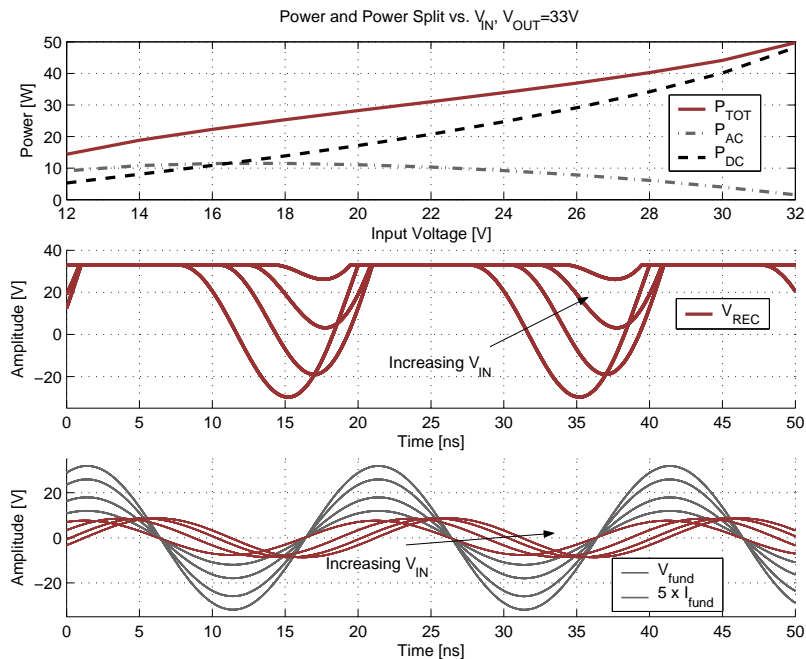


Figure 3.5: Both the total power and the split between ac and dc power delivery depend on the dc bias and ac amplitude at the rectifier input. Component values and simulation files can be found in appendix A

greater loss.

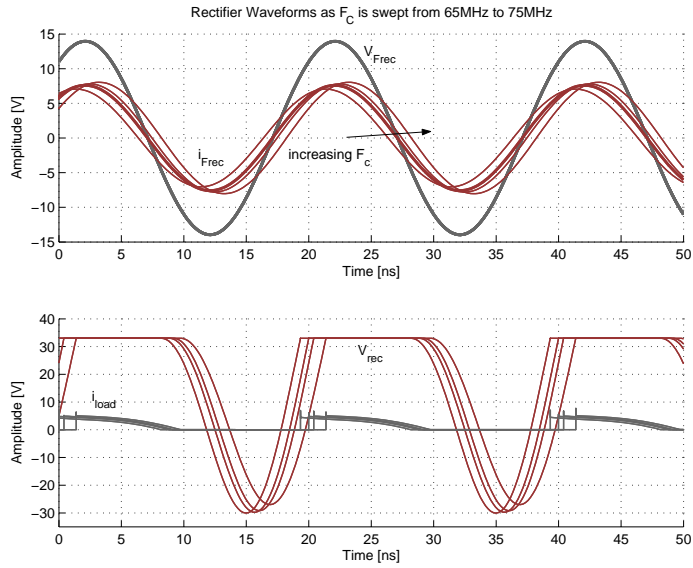
There are several important points to be made about the rectifier behavior as the dc bias and amplitude is swept. To begin with, over a reasonable range of input voltage bias, the output power rises sub-linearly. While the dc power is increasing, ac power falls to zero as the duty ratio limits toward one. This can be advantageous to converter operation because a more gradual change in power with voltage (as opposed to the square-law resulting from a purely resistive load) relaxes the duty ratio requirements for on/off modulation. The effect of dropping ac power delivery on rectifier efficiency is another story. When the rectifier input appears resistive, the total power delivered to the load for a given input voltage amplitude and bias is greatest. As the rectifier becomes more inductive with increasing bias, circulating currents that contribute to loss are not contributing to output power, therefore efficiency drops. One further effect related to the changing rectifier impedance is the loss of perfect ZVS in the dc-dc converter. While a properly tuned inverter will ordinarily maintain ZVS across the input voltage range (assuming an ideal switch capacitance), in the dc-dc converter the rectifier is effectively changing the output tank as dc bias and ac amplitude vary.



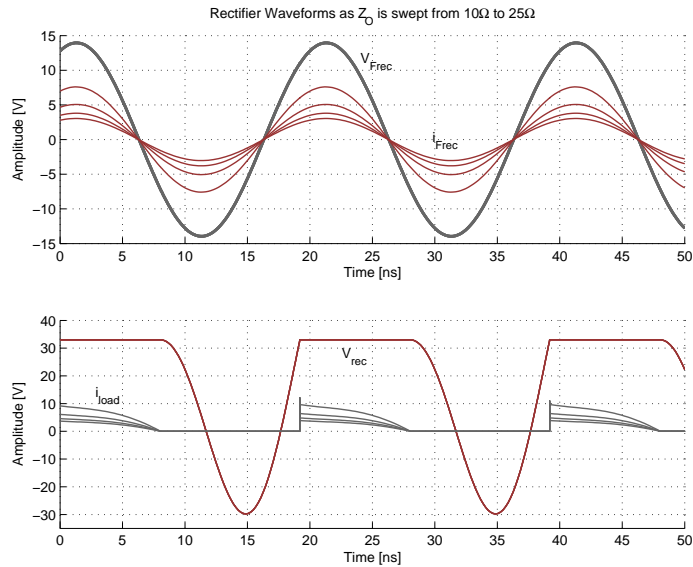
Thus, an inverter coupled with a rectifier will not have ZVS over the input voltage range. Operation without ZVS is detrimental to converter efficiency and interference characteristics. Fortunately, proper tuning can help minimize the effect.

A useful way of tuning a rectifier for a specific resistance at a given dc bias is to choose  $L_{REC}$  and  $C_{REC}$  based on their center frequency and characteristic impedance. Just as in the case of the inverter, the characteristic impedance of the rectifier may be varied while the overall switching behavior remains the same. The larger circulating currents associated with lowering the characteristic impedance delivers more power to the load for a given input voltage, changing the equivalent input resistance. On the other hand, by changing the center frequency the rectifier input can be made to look inductive or capacitive. Since dc bias has the same effect, this handle allows the rectifier to look resistive at a chosen dc bias, a factor that will affect both the peak efficiency and the efficiency vs.  $V_{IN}$  curve of a given dc-dc converter. The plots of fig. 3.6 bear out these dependencies. In the top plot, the center frequency is swept. The rectifier appears resistive at the fundamental when  $F_C$  is  $72MHz$ . This value is then used in the bottom plot where the characteristic impedance is varied from  $10\Omega$  to  $25\Omega$ . Across the range of characteristic impedance, the result is identical switching behavior, but higher circulating currents and therefore lower equivalent resistance.

As another consideration for tuning, the aforementioned variation of rectifier impedance with input voltage is reduced as the rectifier is tuned to look more inductive. Since tuning the rectifier further away from resistive operation decreases efficiency there is potentially a tradeoff between maintaining good ZVS and high efficiency. However, in practical designs high efficiency has tended to outweigh ZVS. Nonlinear device capacitance also has a role to play. One might expect that as  $V_{IN}$  increases, the effective junction capacitance will increase, driving down the resonant frequency of the  $L_{REC}$ - $C_{REC}$  tank. The result should be an even greater shift in the waveforms with bias. This does happen under some circumstances, but the effect may not be pronounced depending on the particular device and voltage range. Comparing a rectifier with an ideal diode and one that uses a diode with a nonlinear junction capacitance (in this case an S310) is illustrative. First, the non-ideal rectifier was tuned to look resistive at  $V_{IN} = V_F = 12V$ . Holding  $L_{REC}$  constant, the ideal rectifier was then tuned to the same conditions (resistive at  $12V$ ) by adjusting  $C_{REC}$ . As the bias is swept from  $12V$  to  $18V$  the resulting phase shift between the two rectifiers differs slightly. In the ideal case, the phase shift is  $25.4^\circ$  whereas the non-ideal rectifier displays a slightly larger shift of  $28.2^\circ$ . The small change in effective capacitance of the diode junction over this voltage range accounts for this small difference. This could be larger for a



(a) Rectifier waveforms as  $F_C$  is swept



(b) Rectifier waveforms for  $Z_O$  sweep

Figure 3.6: The rectifier may be tuned by adjusting  $F_C$  and  $Z_O$ . In fig. (a), the rectifier becomes progressively more inductive for higher  $F_C$ . The bold traces are in phase at  $F_C = 72MHz$ . Fig. (b) shows that changing  $Z_O$  only affects the current (and hence equivalent resistance).  $V_{REC}$  remains unchanged. Tuning the rectifier is easily accomplished by selecting  $F_C$  so the input is resistive at the fundamental and then tuning  $Z_O$  to realize the desired resistance value. Component values and simulation files may be found in appendix A

Case	Ideal Rectifier	Rectifier w/ Junction Capacitance
$\Theta_f$ , Bias Only	25.4°	28.2°
$\Theta_f$ , Amplitude Only	28.2°	25.3°
$\Theta_f$ , Amp. and Bias	43°	43°
$L_{REC}$	59.717nH	59.717nH
$C_{REC}$	98.51pF	50.11pF

Table 3.1: **Phase Shift differs for the ideal and non-ideal rectifiers when input bias voltage and amplitude are adjusted separately. Opposing effects of the junction capacitance cancel for the case when both bias voltage and amplitude are adjusted simultaneously.**

different junction capacitance or over a different voltage range. Interestingly, if the dc bias is held fixed and the amplitude of the fundamental is varied, the behavior is the opposite. The diode effective capacitance decreases with amplitude and this time the nonlinear diode circuit has less phase shift, 25.3° vs. 28.2° than the linear circuit. This is important when both the amplitude and dc bias are changed to mimic the case of an actual inverter as the source. Under these conditions, both rectifiers have an identical phase shift of 43°. The opposing behaviors of the junction capacitance with dc bias and ac amplitude seem to largely cancel over the test range. The results are summarized in table 3.1.

## 3.2 The Power Stage

Having enumerated the salient characteristics of both a  $\Phi_2$  inverter and a candidate rectifier, it remains to connect the two together and arrive at a dc-dc converter. In this case, as discussed in the previous section, when the  $\Phi_2$  inverter is mated with the series-loaded rectifier, the result is a  $\Phi_2$  resonant dc-dc boost converter. The details of interconnection are no more complicated than the substitution of the output tank for the rectifier. Important considerations, however, lie in choosing the appropriate equivalent resistance for the rectifier and at what input voltage it appears resistive. The characteristic impedance of the network also deserves examination, though driven by device selection and operating frequency. Device selection is critical, in the medium power range of 10-20W where prototype converters were constructed, devices dominate the loss budget. Therefore, before proceeding device characteristics of particular importance to the  $\Phi_2$  converter will be examined.

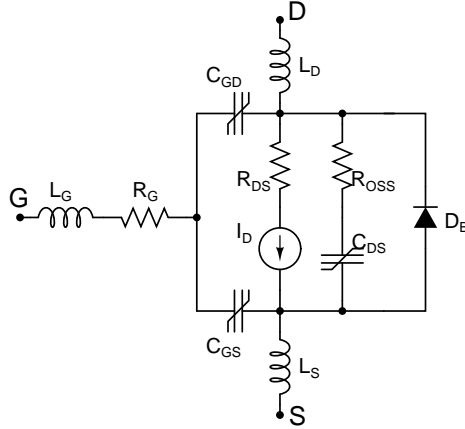


Figure 3.7: The MOSFET parasitic elements important to  $\Phi_2$  converter operation must be accounted for at design time.

### 3.2.1 Important Device Characteristics

Real semiconductor devices include parasitic elements important to the operation of the  $\Phi_2$  converter. Both MOSFETs and diodes used respectively as the active devices in the inverter and rectifier are important in this regard. Figure 3.7 shows a model of a MOSFET. The channel resistance  $R_{DS-ON}$  is of primary importance, and in most suitable devices represents the dominant loss mechanism.  $R_{OSS}$  and  $C_{OSS}$  take a close second. The displacement currents flowing through  $C_{OSS}$  during the drain excursion each cycle amount to significant loss in  $R_{OSS}$ . The value of  $C_{OSS}$  sets this current along with the drain voltage and switching frequency ( $i_{C_{OSS}} = C dv/dt$ ). It also influences the range of characteristic impedance that can be achieved. When  $C_{OSS}$  comprises the entirety of  $C_F$ , the minimum achievable characteristic impedance at a given frequency is reached. This influences both the conduction and displacement currents and the corresponding loss from  $R_{DS-ON}$  and  $R_{OSS}$ . Thus as a figure of merit (ignoring gate drive concerns and assuming dominantly conduction loss) the product  $R_{DS-ON}C_{OSS}^2$  offers a rough indication of device performance in the  $\Phi_2$  converter. The gate resistance  $R_G$  and input capacitance  $C_{ISS}$  are also important. Under sinusoidal resonant drive the gating loss is described by eqn. 3.2,

$$P_{gate} = (\pi C_{ISS} V_{ac} f_{SW})^2 R_G \quad (3.2)$$

where  $V_{ac}$  is the amplitude of the sinewave and  $f_{SW}$  is the fundamental frequency.

Other drive methods exist such as resonant trapezoidal gating which offers lower loss [30], but sinusoidal gating is preferred here for simplicity. From the equation it is evident that the gate loss rises linearly with  $R_G$  and as the square of  $C_{ISS}$ . In the 10-20W power range with typical devices, the gate loss can be several percent of the total power processed, and care must be taken to minimize this loss.

The gate to drain capacitance  $C_{RSS}$  has a significance all its own. Whatever the gate drive scheme selected, the current conducted through  $C_{RSS}$  as the drain transitions must not unduly influence the gate voltage. In terms of device selection this potentially excludes many vertical devices which have much larger  $C_{RSS}$  than the LDMOS devices used for prototyping. It also implies that the impedance looking back from the gate (into the gate drive circuit) must be small enough that the voltage is controlled by the gate drive. In the case of the sinusoidal drive, the resulting drain-gate transfer function was critical in achieving the appropriate operating frequency. This will be discussed in more detail in the chap. 5

The parasitic inductances arising primarily from packaging constraints can be significant to  $\Phi_2$  converter operation. In many cases it is desirable to augment  $C_{OSS}$  with external shunt capacitance (usually to control the peak voltage as discussed in chap. 2). In this case, the loop inductance resulting primarily from  $L_S$  and  $L_D$  can result in ringing that may affect converter behavior, and ultimately increase loss. In addition,  $L_G$  and  $L_S$  can make gating difficult as ringing at the gate may cause the switch to commutate several times per cycle and render a converter design infeasible. Ringing at the gate as well as across the drain source terminals is reduced to an extent by the smooth transitions characteristic of resonant operation. However, the non-linear parasitic capacitances and behavior of the rectifier act to upset ZVS introducing high frequency components that may excite the resonances. As a result the package inductance is best minimized and packaging is sought that achieves this goal. In many cases, devices used in RF applications have special packaging that specifically addresses parasitic inductance and works well in  $\Phi_2$  converter applications. In this work the first converter was constructed with such a device (an STMicroelectronics PD57060 in a POWERSO-10RF package) and follow-on prototypes were built with a custom die in a 20-pin TSSOP package where all 20-pins were used for the three device terminals to minimize inductance. In both cases, loop inductance was held to less than  $1nH$  which was sufficient to prevent interference with converter operation.

Diode parasitics are similarly important. Junction capacitance influences both achievable  $Z_o$  and the circulating currents in the rectifier. The effective resistance of the

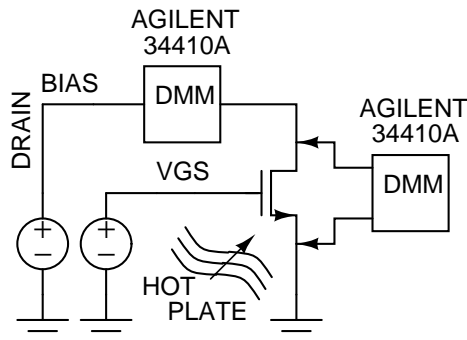


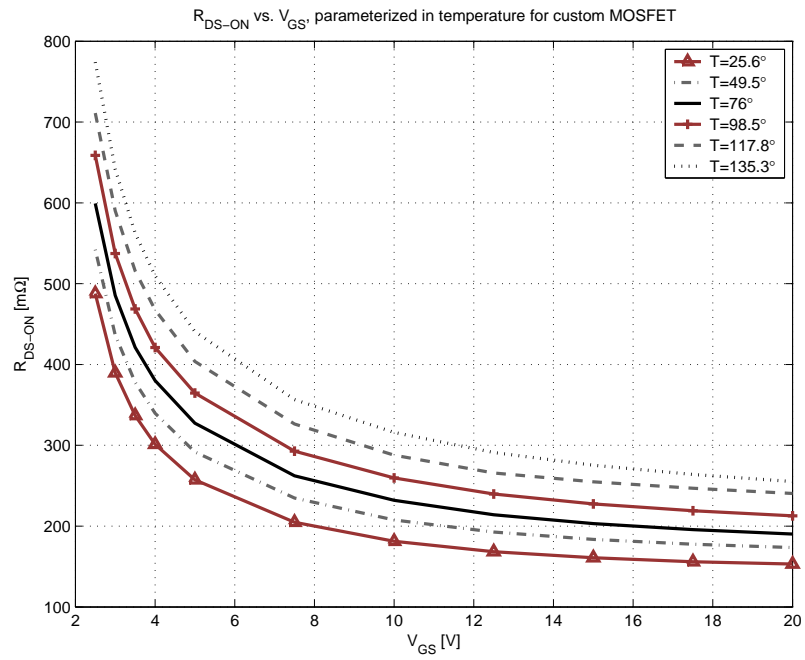
Figure 3.8: **The MOSFET was biased to  $I_D = 1A$  and  $V_{DS}$  measured to determine channel resistance. Temperature is controlled by a hot plate.**

drift region is significant to loss, as is the forward voltage drop. Reverse recovery losses characteristic of minority carrier devices like the conventional P-N junction diode, are largely avoided with Schottky diodes, favoring their use at VHF frequencies. In the prototypes constructed, diode loss was the second biggest loss mechanism underscoring the importance of finding an appropriate device.

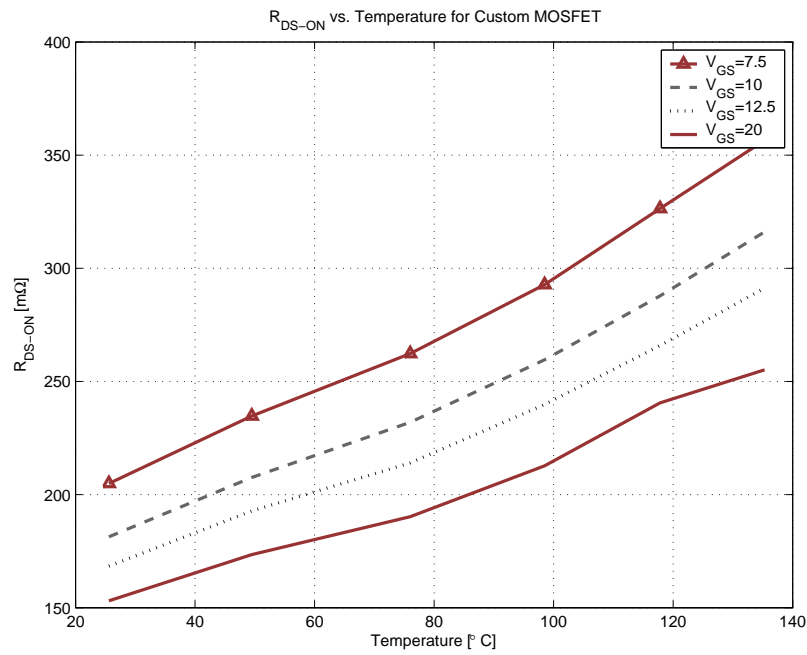
The values of the many parasitic elements were extracted by a variety of measurement techniques. In the case of the MOSFET,  $R_{DS-ON}$  was measured versus  $V_{GS}$  by biasing  $I_d$  to one amp and measuring  $V_{DS}$ . A schematic of the test setup can be found in fig. 3.8. The further dependence of on-resistance with temperature was measured by affixing the devices to a hotplate to get  $V_{DS}$  vs. junction temperature. A similar technique to extract forward drop vs temperature was used on the diodes. The MOSFET data is plotted in fig. 3.9.

Device capacitances were measured using an Agilent 4195A in impedance analyzer mode.  $C_{DS}$ ,  $C_{GS}$  and,  $C_{GD}$  were extracted vs. voltage by taking three sets of two-terminal measurements under bias. The various measurement setups are shown in fig. 3.10. The same measurements were used to obtain  $R_{OSS}$  by taking the impedance at the self-resonant frequency (where  $C_{OSS}$  and the parasitic inductance of the measurement loop are resonant) during measurement A (in fig. 3.10).  $R_{OSS}$  was also measured vs. temperature on a hot plate and it was found to have roughly the same temperature coefficient as  $R_{DS-ON}$ .

The resulting set of small-signal capacitances was used to reconstruct the large signal capacitance behavior by curve-fitting the measurements to the depletion capacitance model mentioned in chap. 2. This approach should remain valid for very high frequen-



(a)  $R_{DS-ON}$  vs.  $V_{GS}$



(b)  $R_{DS-ON}$  vs. Temperature

Figure 3.9: Temperature dependence of the channel resistance of the custom MOSFET used in this thesis

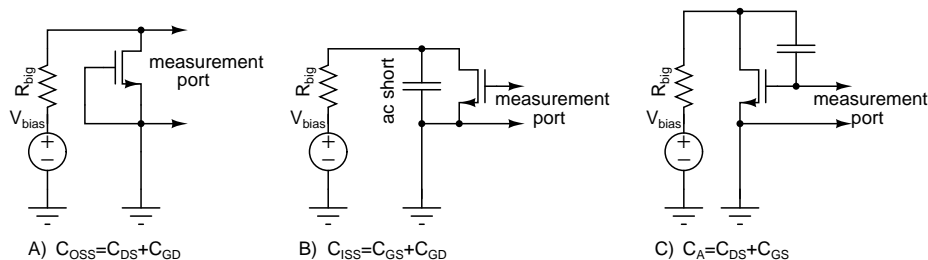


Figure 3.10: **Since the MOSFET capacitances cannot be measured directly, three measurements are required to extract the values. An Agilent 4195A in impedance analyzer mode was used to measure the capacitance at 1MHz.**

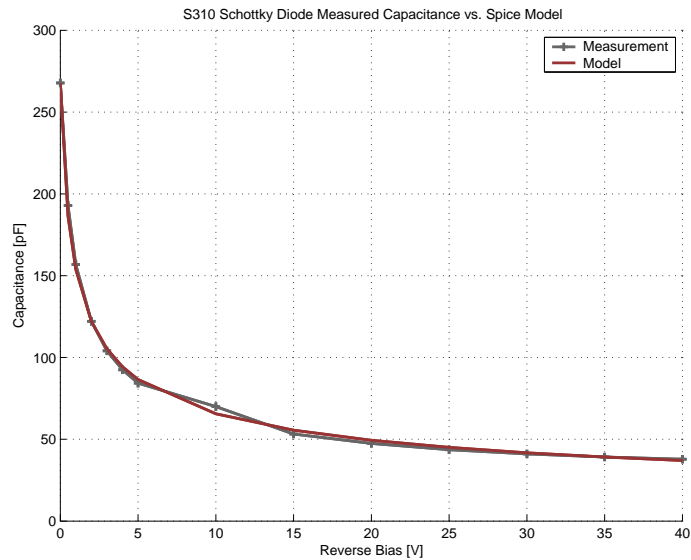
cies as the quasi-static assumption does not break down unless changes take place on the order of the dielectric relaxation time, which is typically much shorter than the switching periods of interest. This is supported by the experimental results of chapter 4. In SPICE both  $C_{GS}$  and  $C_{GD}$  were modeled as linear capacitors.  $C_{OSS}$ , on the other hand, was modeled using a behavioral current source to simulate the nonlinearity. The plots in fig. 3.11 show the match between the spice model and measured results for both diode and MOSFET capacitance.

### 3.2.2 Linking the Inverter and Rectifier

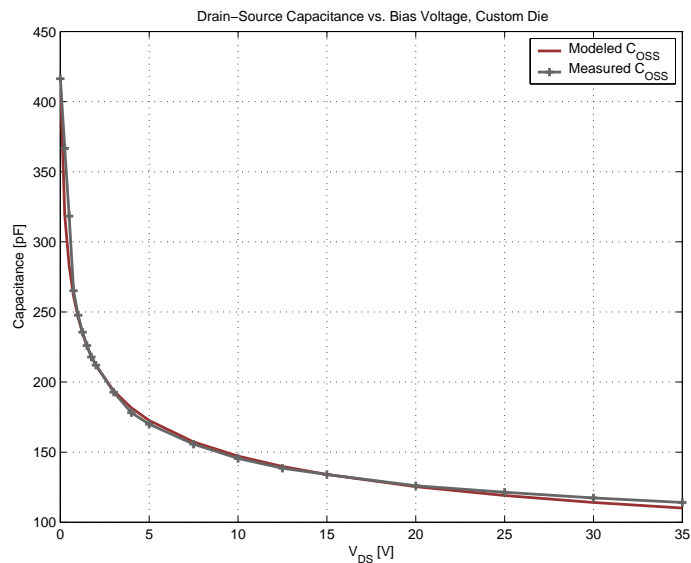
Armed with device models that include parasitic elements, we are now in a position to assemble a dc-dc converter from a rectifier and inverter. The design begins with a rectifier. The desired output power is  $17.3W$ . The rectifier will be tuned to appear resistive at the fundamental when the input voltage is  $14V$  and the output voltage is  $33V$ . To start the design an ideal diode is used with a capacitance equivalent to the diode capacitance at the dc bias,  $19V$ . For this diode with  $C_{JO} = 267.77pF$ ,  $M = 0.42$ , and  $V_J = 0.365$ , the equivalent capacitance is  $50.43pF$ . With the  $50MHz$  sinusoidal input set to a  $14V$  bias and the fundamental amplitude of  $16V^1$  the center frequency  $F_C$  of the  $L_{REC}-C_{REC}$  tank is swept until the fundamental voltage and current are in phase, which occurs at  $F_C = 68MHz$ . At this point, the characteristic impedance can be adjusted until the desired output power is met, this occurs at  $Z_O = 24\Omega$ . The final values for  $L_{REC}$  and  $C_{REC}$  are  $56nH$  and  $47pF$  respectively, after

<sup>1</sup>In this case, the amplitude of the fundamental was determined based on a previous inverter design. Since the aim is to reproduce the impedance characteristics of that inverter to get the same drain voltage waveform, extracting the fundamental beforehand is fine.





(a) Diode Junction Capacitance



(b) MOSFET  $C_{OSS}$

Figure 3.11: Nonlinear device capacitance plots showing measured values vs. the model. The spice model parameters for the diode are as follows:  $C_{JO} = 267.8p$ ,  $M = 0.420$ ,  $V_J = .365$ . The spice model parameters for the MOSFET are:  $C_{JO} = 425.2p$ ,  $M = 0.253$ ,  $V_J = 0.177$ . Detailed device models can be found in appendix A

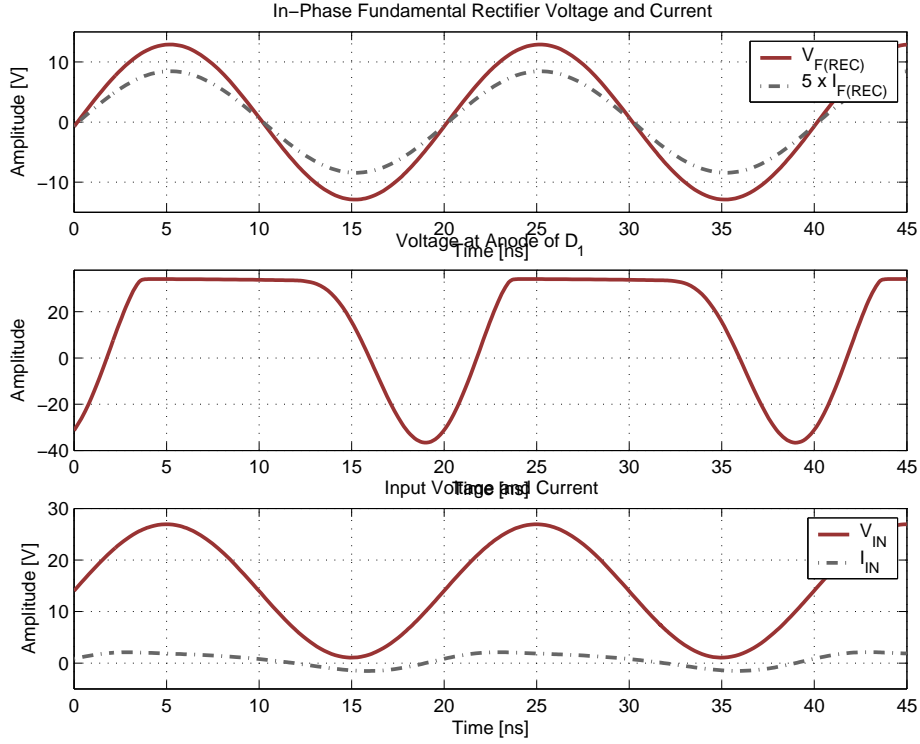


Figure 3.12: The nominal waveforms of a tuned rectifier. Note that the fundamental voltage and current are in phase allowing the rectifier to be represented as a resistor in a describing function sense.

the  $50pF$  equivalent switch capacitance is extracted. When these values are included in a simulation of the rectifier with the full diode model and all parasitic elements (inductor  $Q = 80$  and capacitor  $Q = 5000$ ) the result is an output power quite close to  $17.3W$ . Figure 3.12 shows the rectifier waveforms and the in-phase fundamental voltage and current (rectifier input current is multiplied by 5 for visibility). The next step is to extract the rectifier equivalent resistance, in this case  $V_{F_{REC}}/I_{F_{REC}}$  which gives  $R_{eq} = 7.63\Omega$ .

Under the assumption that the ac and dc power delivered to the load can be treated separately, the ac power that the inverter should deliver can be calculated from eqn. 3.1 as  $10W$ . Using the fundamental of the inverter drain voltage and the equivalent resistance of the rectifier,  $7.63\Omega$ , the value for the divider inductor  $L_{DIV}$  is computed as  $20nH$ . The inverter is then tuned to achieve the desired impedance characteristic. In this case, it is known that ZVS will be achieved for a fundamental phase,  $\Theta_f = 35.818^\circ$  and a drain voltage magnitude ratio fundamental:third

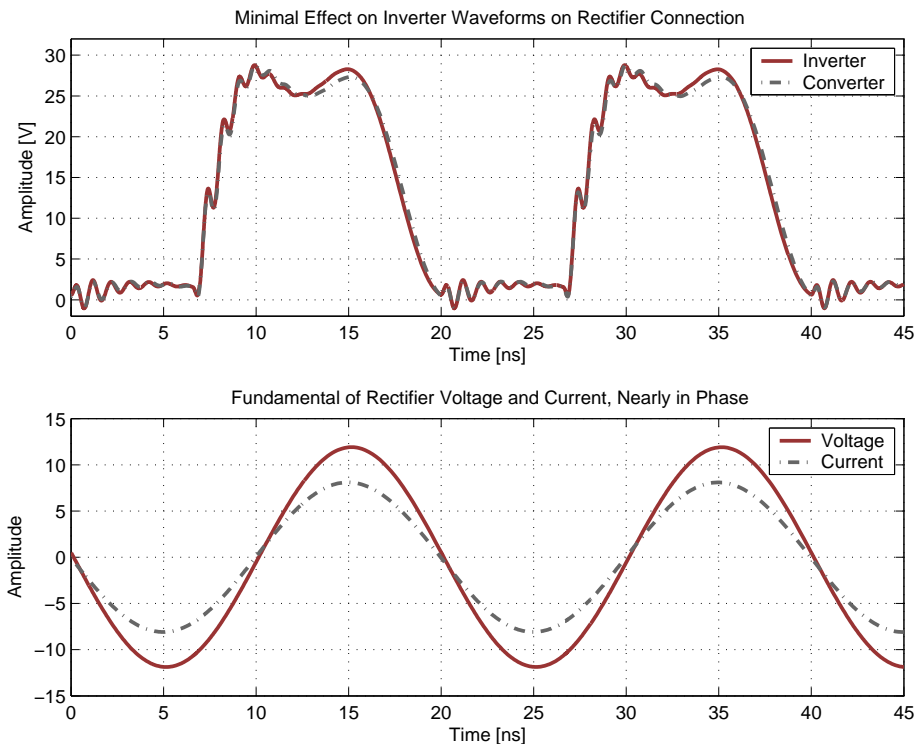


Figure 3.13: Nearly identical drain waveforms between the inverter and converter show the minimal effect connecting the rectifier has on inverter operation. Similarly, the fundamental voltage and current are nearly in phase as is the case when the rectifier is driven solely with a fundamental voltage.

harmonic,  $\Delta_{1-3} = -2.01dB$ . The dc-dc converter components that realize this impedance relationship are listed in table 3.2.2. The output power is  $10W$  as desired.

When the inverter and rectifier are connected, the result should be identical drain waveforms and an output power of  $17.3W$ . While the drain waveforms are almost identical (see fig. 3.13, the output power is only  $15.3W$ , about 11% low. This arises because the rectifier equivalent resistance is a function of both the dc bias and the ac amplitude of its drive voltage. However, correcting the power is relatively straightforward. The inductor  $L_{DIV}$  is adjusted in the dc-dc converter until the desired output power is achieved. The new value is  $L_{DIV} = 13nH$ . ZVS can then be reestablished by again tuning the inverter to meet the same impedance characteristic. The result is a higher inverter output power of  $12.5W$ . When the original rectifier and readjusted inverter are mated, the drain voltage waveforms are almost identical and the output

## The $\Phi_2$ dc-dc Converter

---

Component	Initial dc-dc Converter	Final dc-dc Converter (17.3W)
$L_F$	24.23nH	39.06nH
$C_F$	54.4pF	121pF
$L_{2F}$	78.32nH	78.32nH
$C_{2F}$	32.34p	32.34pF
$L_{DIV}$	20nH	13nH
$L_{REC}$	56nH	56nH
$C_{REC}$	47pF	47pF
Duty Ratio	0.3	0.3
$f_{SW}$	50MHz	50MHz
$V_{IN}$	14V	14V
$V_{OUT}$	33V	33V
$P_{OUT}$	15.3W	17.3W

Table 3.2: The components of the dc-dc converter examples are listed in this table. More detailed information including the full spice models and values of parasitic inductances may be found in appendix A

power is 17.3W as intended. While the procedure requires some iteration, it can be accomplished quickly. The final components values are listed in the second column of table 3.2.2. The final dc-dc converter waveforms are presented in fig. 3.14.

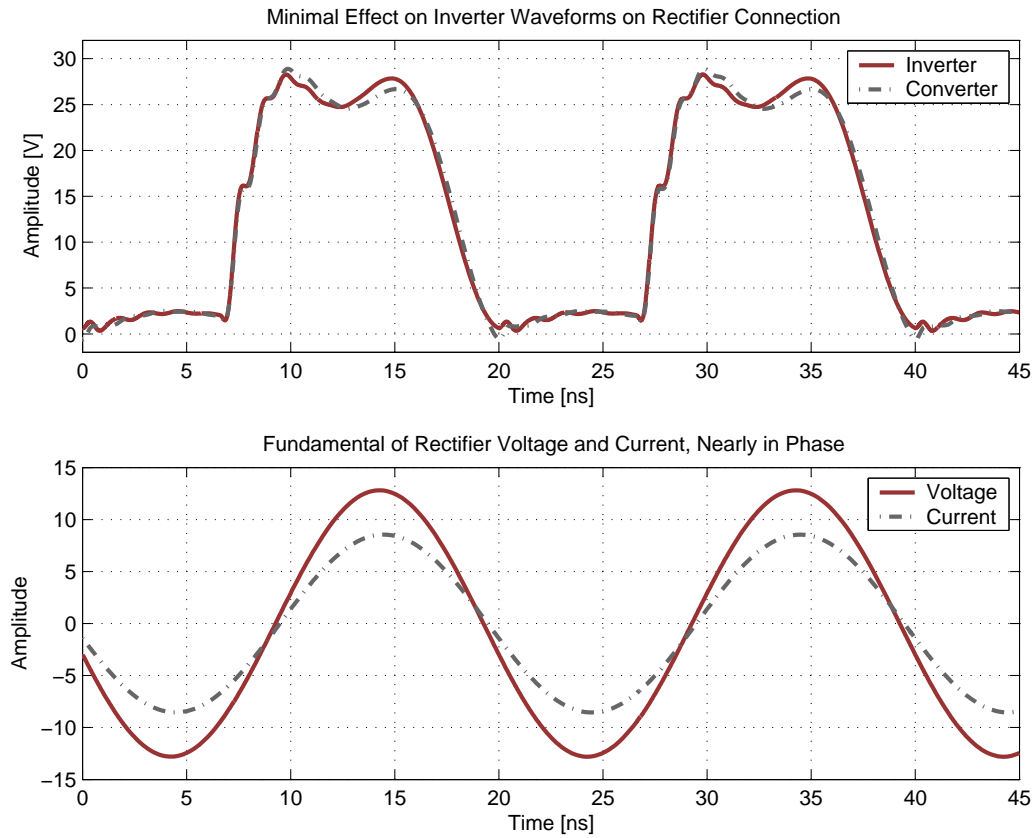


Figure 3.14: After the output power is corrected, the dc-dc converter behaves just as in the initial example. Nearly identical drain waveforms between the inverter and converter and in-phase rectifier voltage and current show the minimal effect connecting the rectifier has on inverter operation.



## *Converter Prototypes*

---

THE following pages present a few prototype converters supporting the augury of the preceding chapters as having some basis in fact. Two designs represent an initial implementation using an off-the-shelf RF power MOSFET and a follow-on built with a custom device. The off-the-shelf component served as the main switch in the first  $\Phi_2$  converter, a proof of concept. The custom device was made in a standard BCD power process and mounted in a 20-pin TSSOP package. Converters constructed with this device are intended to demonstrate the feasibility of using a standard power process to realize a VHF converter in the  $\Phi_2$  topology.

### **4.1 The First Prototype**

As a prelude to constructing a prototype, a target application in the automotive operating range was selected. This includes an input voltage range from 8V-18V with normal operation in the range of 11V-16V. The output voltage dictated by the specific application, in this case LED headlamp drivers, is selectable over a range of 22V - 33V. Nominal output power is about 20W. While this application doesn't require the fast transient response of the  $\Phi_2$  converter, it does require a boost converter. It also makes a good starting point because the input voltage and output power are well matched to the capabilities of a  $\Phi_2$  converter based on the available 50V process device. For instance, a lower input voltage range for the same output power demands higher circulating currents. Since resonating losses rise as the square of the circulating current, an application with a lower input voltage or much higher output power would be an unreasonable target for a first attempt at building the  $\Phi_2$  converter topology.

Choice of operating frequency is subject to the dual constraints of the semiconductor parameters and the existing frequency allocations provided by the FCC. Taking

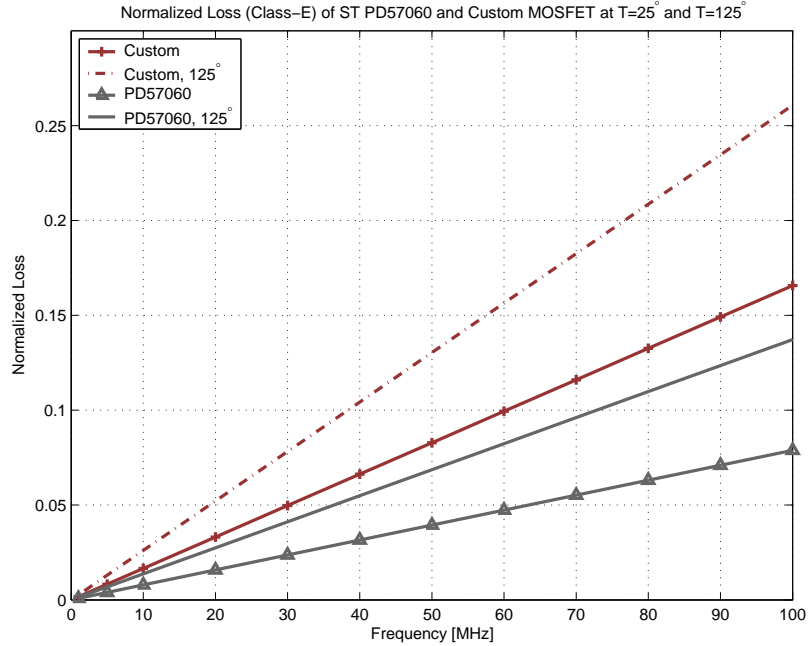


Figure 4.1: Evaluating devices based on their normalized loss in a class-E converter is useful in establishing a baseline. However, it does not provide an absolute measure of performance in the  $\Phi_2$  converter.

semiconductor limits as a starting point, the closed-form design equations available for the class-E inverter allow determination of normalized device loss vs. operating frequency [31]. While this does not quantitatively predict loss in a  $\Phi_2$  converter application, it does suggest a reasonable operating range. It also provides a means to rank devices based on performance in a VHF conversion scenario, under the expectation that relative performance of a set of switches doesn't change across converter topology. A plot of the normalized loss vs. frequency for the ST Microelectronics PD57060 and the custom MOSFET, fabricated in a generic power process, is found in fig. 4.1, while table 4.1 lists relevant MOSFET performance parameters derived from the measurements described in chap. 3. Diode parameters are listed in table 4.1. Two curves are plotted for each device, one at room temperature and the other for a 100°C rise in junction temperature. In the latter case, drain-source resistance is expected to rise by a factor of 1.5 or so (see chapter 3). In looking at the plot of normalized loss and the specific device parameters, it is evident that the part optimized for RF performance has a significant advantage in its lower  $\tau_{GATE}$  and  $R_{DS-ON}C_{OSS}^2$  product. Since the goal is to establish the viability of using a generic power process to substitute for an RF device in what amounts to an RF application, the difference serves merely



Parameter	PD57060	Custom MOSFET
$R_{DS-ON}, T_{NOM}, V_{GS} = 8V$	211m $\Omega$	200m $\Omega$
$R_{DS-ON}, T + 100^\circ C$	350m $\Omega$	350m $\Omega$
$C_{OSS}, V_{DC} = 16V$	68pF	132pF
$R_{DS-ON}C_{OSS}^2$	924 $\Omega pF^2$	3480 $\Omega pF^2$
$C_{ISS}$	100pF	276pF
$R_{GATE}$	195m $\Omega$	1.7 $\Omega$
$\tau_{GATE}$	47ps	469.2ps
$R_{OSS}$	655m $\Omega$	600m $\Omega$
$C_{JO}$	185.2pF	416.3pF
$M$	0.221	0.233
$V_J$	0.168	0.117
$L_{drain}$	400pH	400pH
$L_{source}$	200pH	100pH
$L_{gate}$	400pH	600pH

Table 4.1: MOSFET parameters

$V_{FWD}$	$R_{SER}$	$R_{CJ}$	$C_{JO}$	$V_J$	$M$	$C_{JNOM}$	ESL
0.55V	300m $\Omega$	300m $\Omega$	267.8pF	0.365	0.420	50.4pF	1nH

Table 4.2: Faichild S310, 100V, 3A Schottky diode parameters

to illustrate the point. It ultimately manifests as a set of design tradeoffs made to exploit the different devices.

For the PD57060, assuming a 100 $^\circ C$  temperature rise, the normalized loss tips over 10% right around 75MHz. This makes a convenient design frequency because it falls just below the FM band (88MHz - 108MHz) while still high enough to ensure small passive components. The choice represents a certain amount of judgement as the device loss in the  $\Phi_2$  converter will be different than in a class-E converter.

An initial design was simulated in spice based on a 75MHz switching frequency and the target voltages and power. The resulting component values are indicated on the schematic in fig. 4.2. Several practical issues were exposed during the course of the design. First, additional shunt capacitance intended to reduce the peak drain voltage caused excessive ringing with the package inductance. The 100pF originally added across the switch and the approximately 1nH loop inductance associated with the packages and routing form a resonance with a relatively low characteristic impedance (about 2.5 $\Omega$ ). In this range, damping is out of the question as it would incur too

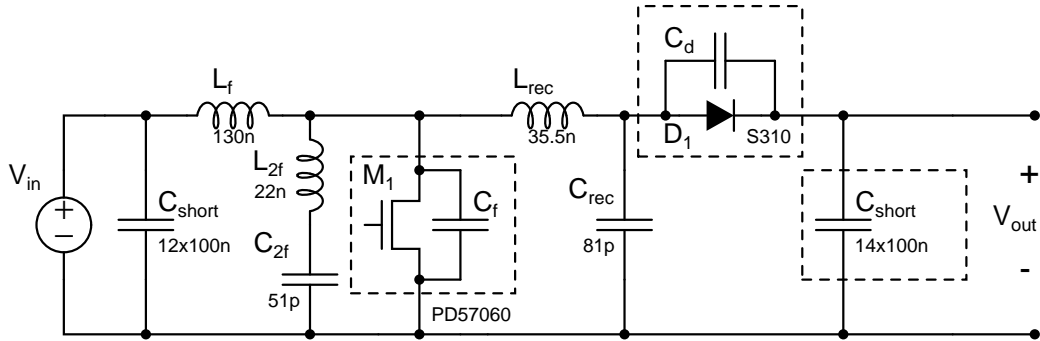


Figure 4.2: **Final component values of  $\Phi_2$  converter implemented with ST PD57060.**

much loss. The alternative, removing additional capacitance, had to be compensated in the design by increasing the value of  $L_F$  from  $28nH$  to  $130nH$ . This became the largest inductor in the design, whose volume increases the difficulty of realizing either a co-packaged or integrated implementation. It also affects the transient response of the converter as in chapter 3, though this is less of a concern because the resulting transient response is still quite good. While not a factor here, another issue that could arise, particularly in an integrated design, is the resulting higher peak voltage stress. This points to the need to either reduce package parasitic inductance to the point where it is no longer a concern, or have continuous control over the device area to control impedance without additional capacitance.

Another design-time choice included tuning the rectifier to look relatively inductive. In this regime, the change between the voltage and current fundamental components as the input voltage changes is reduced. This minimizes the effect of rectifier non-linearity on the ZVS characteristics of the inverter. If this was a critical component of the design, perhaps for minimizing converter emissions, it may be well justified. However, it corresponds to a reduction in efficiency because the ac component of power delivery accompanies larger circulating losses than in the resistive case. Where efficiency is paramount, tuning the rectifier to appear resistive within the operating range is a better option. This was the case in the second prototype, as will be discussed shortly.

Ringing in the loop around the main switch was not the last word in that regard. The series combination of  $C_{REC}$  and the diode junction capacitance also resonate with the parasitic inductance around the  $C_{REC}$ -diode loop. The loop is highlighted in figure 4.3, along with a simulation of the diode current. In simulation, the ringing

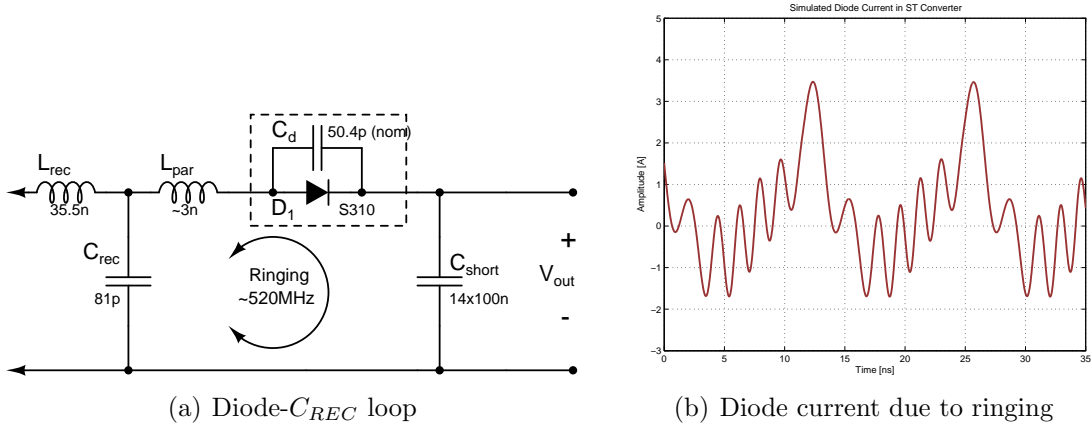


Figure 4.3: **Ringing among the diode capacitance,  $C_{REC}$ , and the parasitic inductance results in increased diode loss due to larger circulating currents.**

results near  $530\text{MHz}$ , consistent with the  $31\text{pF}$  equivalent capacitance in series with the  $3\text{nH}$  loop inductance. The relatively large excursions increase the circulating currents in the diode to the point that its power dissipation limits would be exceeded if left unchecked. To circumvent this problem, converter output power was lowered at the expense of an overall reduction in efficiency.

Similarly to the main switch case, the necessity of an external capacitor  $C_{REC}$  is at the root of the problem. It is essentially in parallel with the diode junction capacitance, and added to achieve the desired characteristic impedance. Since the impedance is dictated by the choice of converter operating point, it is a difficult tradeoff to avoid. Discrete diodes do not offer a continuous range of junction capacitance, and compensating by changing  $L_{REC}$  may not be feasible. On the other hand, when the diode area can be scaled, as in an integrated process, no external capacitance is necessary. This eliminates the loop and ringing. The parasitic inductance around the loop in question as part of  $L_{REC}$ , and scarcely noticed except for an offset in output power provided reasonable care is taken to minimize loop area.

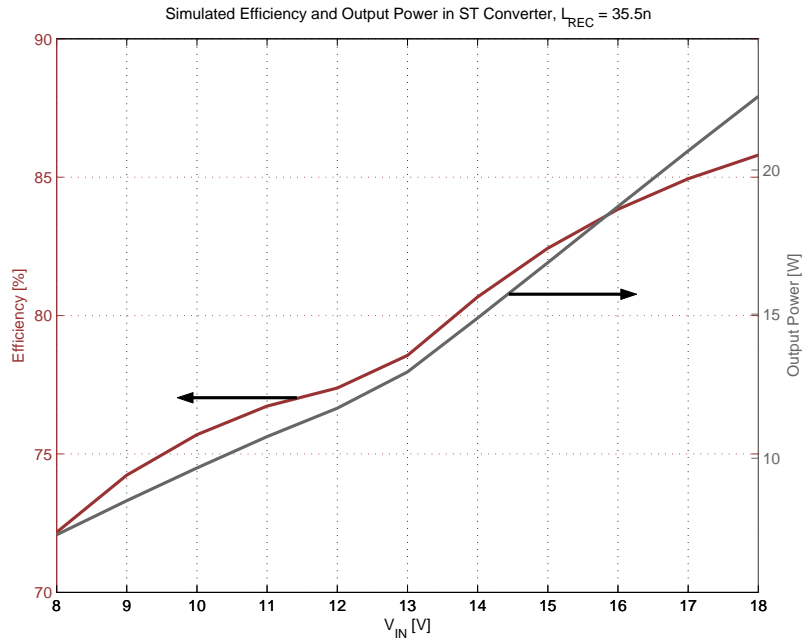
The simulated output power and efficiency vs. input voltage from the resulting design are presented in fig. 4.4(a) where the output voltage was held constant. The same variables are plotted vs.  $V_{OUT}$  in fig. 4.4(b) while  $V_{IN}$  is held at  $14\text{V}$ , automotive nominal. In both plots the efficiency rises monotonically as the amount of dc power delivery increases (dc power delivery increases with decreasing conversion ratio, therefore it is higher for larger  $V_{IN}$  in the first plot and smaller  $V_{OUT}$  in the second). This is an artifact of a rectifier that looks inductive at the fundamental over

the voltage sweep range. Since ac power delivery will be relatively inefficient in this case, increasing the proportion of dc power improves total efficiency. This has the overall effect of reducing the peak efficiency because there is never a situation where ac power delivery is particularly efficient. The situation is different when the rectifier is tuned resistive within the input voltage range, as in the second prototype.

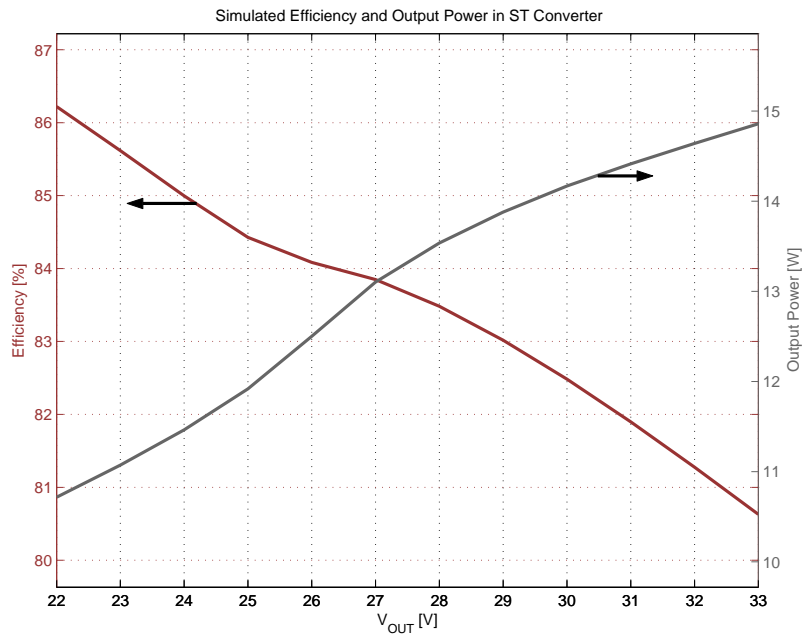
The converter was constructed on a 4-layer PCB. A photograph of the board is shown in fig. 4.13(a) and schematics and PCB artwork are provided in appendix B. The choice of four layers was not due to routing concerns. Rather, the prepreg material that separates the top and bottom copper from the inner layers is very thin, on the order of 10 mils in this case. When the inner layers are used as a ground plane (in fact, three of the four layers were ground in this design), the parasitic inductance is much reduced over what could be expected with a normal 2-layer FR4 board. This makes building the converter easier as fewer board parasitics mean fewer component changes in compensation. It also helps efficiency as trace parasitic inductance tends to be low  $Q$ . In general, parasitic inductance and capacitance must be considered when laying out the board and during construction. Thus, extensive inter-layer vias to ground were used where possible to ensure good ground connections and reduce inductance. Where low inductance was required between components, traces were kept wide and short. At nodes sensitive to capacitance, narrow traces were placed above ground plane notches.

As was established in chapters 2 and 3 converter dynamic performance can be predicted if the desired impedance across the drain-source port of the switch is attained. Thus, the overarching procedure to realize a working converter involves developing a time-domain simulation in SPICE with the desired characteristics and then trying to match its drain-source impedance when building the prototype. Since parasitic components can affect this impedance significantly, they must be accounted for. Rather than explicitly computing board parasitics with a simulator, the design approach involved minimizing the parasitics using the rules of thumb described above, followed by careful measurement during the construction phase. Measurement was accomplished with an Agilent 4195A in impedance analyzer mode. A jig was fabricated to connect the PCB to the analyzer. Besides providing a low-inductance electrical connection, the jig is a mechanically stable platform so measurement to measurement parasitics are consistent.

Construction begins by shorting the drain-source node of the circuit board, then measuring the loop inductance of the jig. The jig is constructed to keep parasitic



(a) Efficiency and power vs.  $V_{IN}$  at  $V_{OUT}=32V$



(b) Efficiency and power vs.  $V_{OUT}$  at  $V_{OUT}=32V$

Figure 4.4: Simulated  $\Phi_2$  converter power and efficiency. Note the monotonic behavior of power with voltage that results from the inductively tuned rectifier.

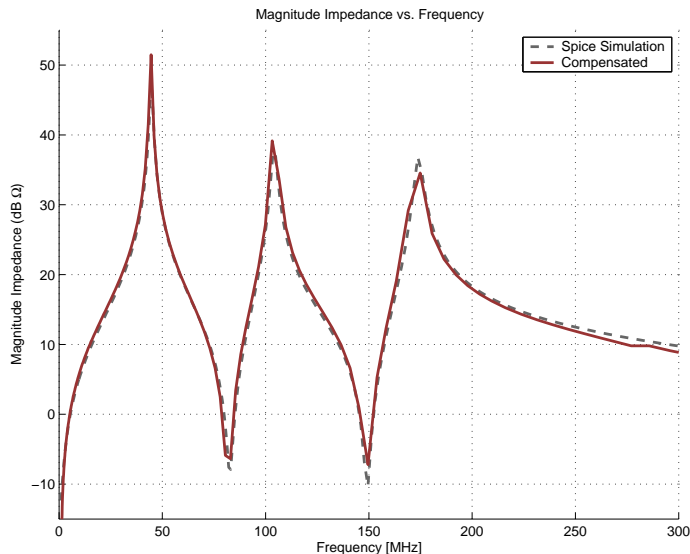
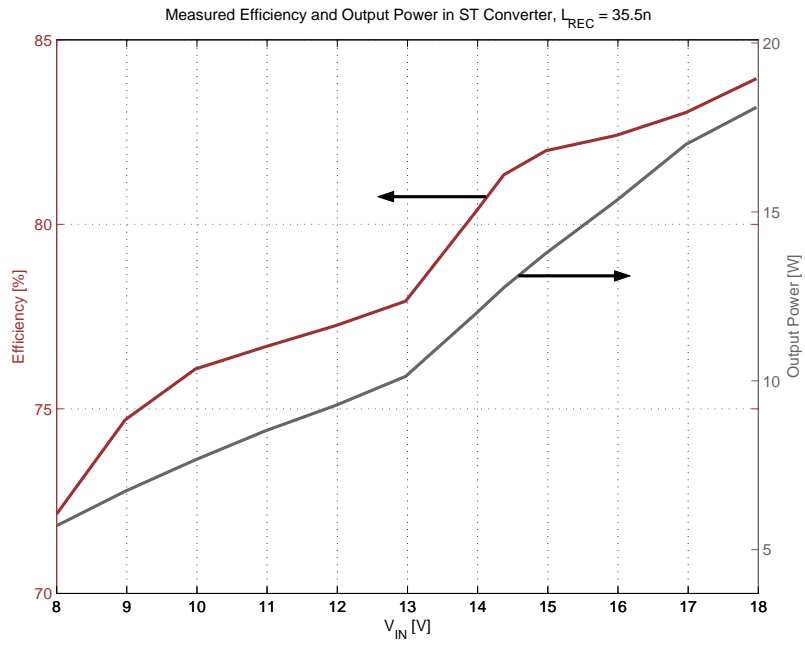


Figure 4.5: **The compensated measurement compares well with the simulated drain-source impedance.**

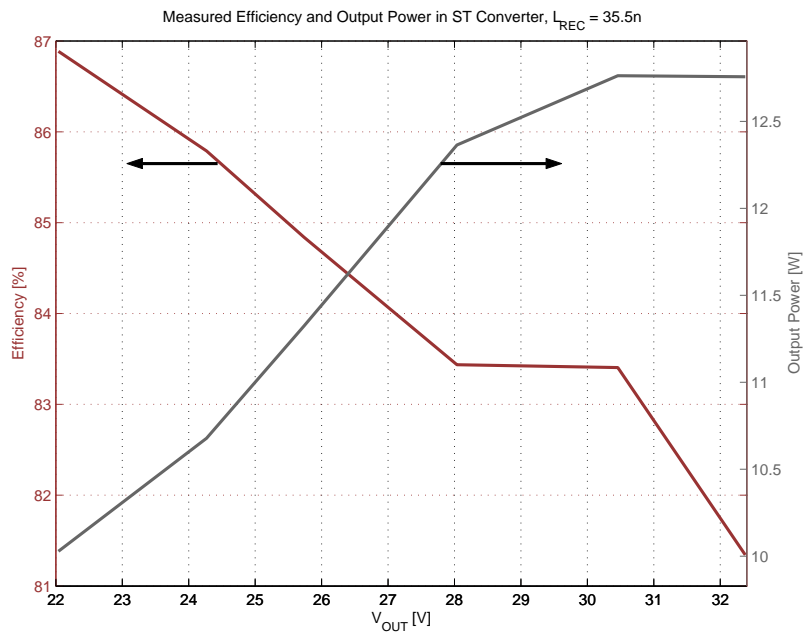
capacitance (and hopefully inductance) to a minimum, but it must be calibrated out. After mounting a board with shorted drain and source nodes, the loop inductance of the jig assembly can be measured. Thus, any remaining parasitic inductance can be subtracted point-by-point from further measurements. The converter is then built up one branch at a time, starting with the second harmonic short. Parasitic elements are either compensated with component changes or accounted for in a SPICE simulation to ensure the effects are minimal. A more detailed discussion of this method can be found in [19]. The final result is a good match between measured and simulated drain-source impedance as displayed in fig 4.5.

Fig. 4.6 plots the measured converter output power and efficiency. The general trends from the simulation of fig. 4.4 are well represented. Specific differences are not easily accounted for, but probably involve thermal effects, among others. There is a significant difference between output power at the upper range of  $V_{IN}$ . This may be partly due to inadequate measurement of parasitic elements, as output power is particularly sensitive to the value of  $L_{REC}$ . On the other hand, the experimental waveforms of fig. 4.7 match simulation rather well.

This converter did not include a gate drive. Instead, the gate of the PD57060 was driven directly from an RF power amplifier (an AR-150A100B) with a  $50\Omega$  output impedance. This worked well for the purposes of verifying the viability of the  $\Phi_2$

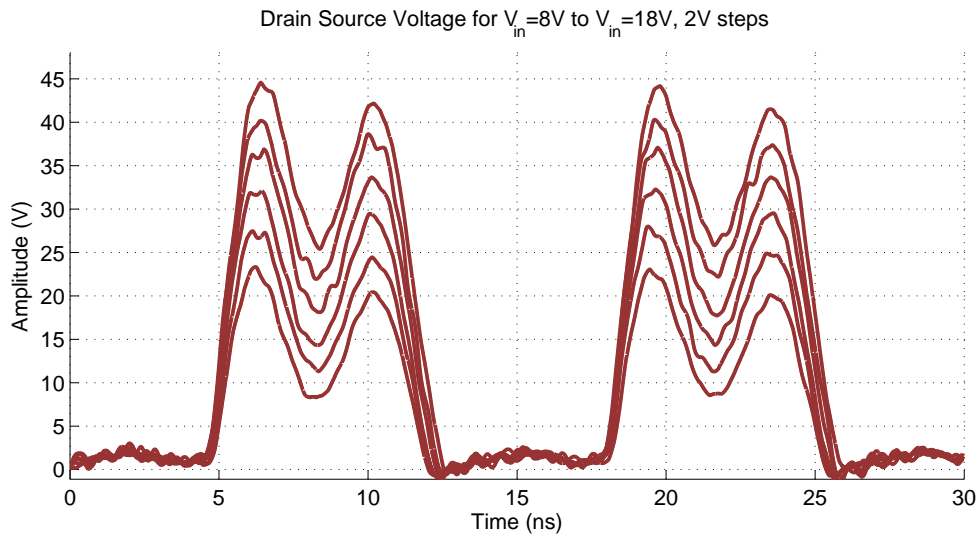


(a) Efficiency and power vs.  $V_{IN}$ ,  $V_{OUT}=32V$

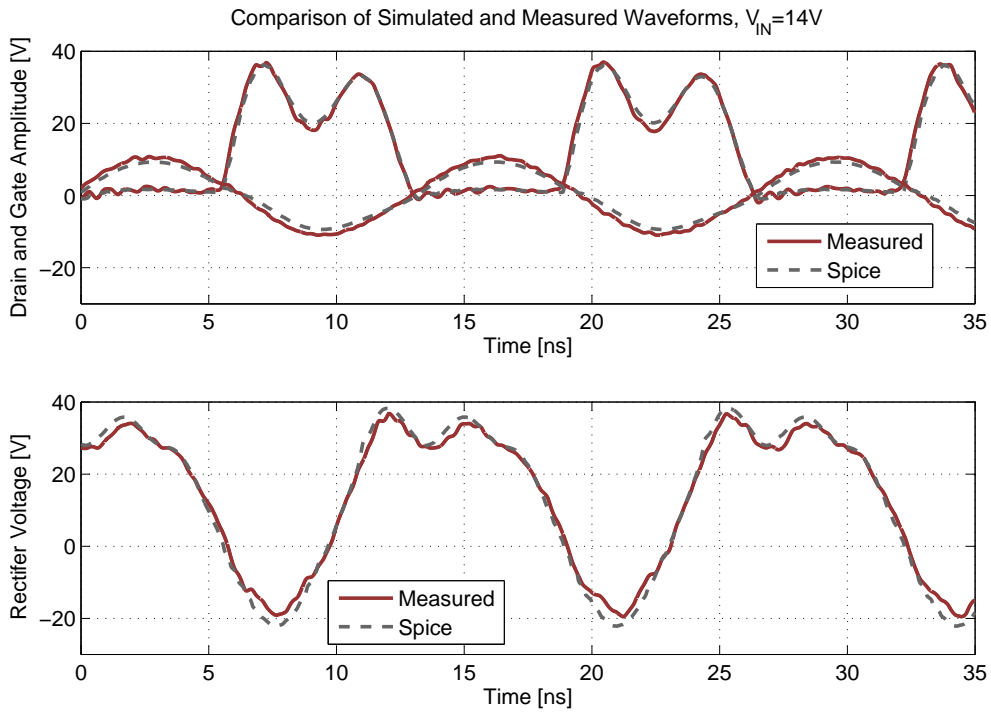


(b) Efficiency and power vs.  $V_{OUT}$ ,  $V_{IN}=14V$

Figure 4.6: The measured output power and efficiency



(a) Drain waveforms plotted over  $V_{IN}$



(b) Comparison between measured and simulated converter waveforms

Figure 4.7: The measured and simulated converter waveforms agree closely as a result of the good impedance match.



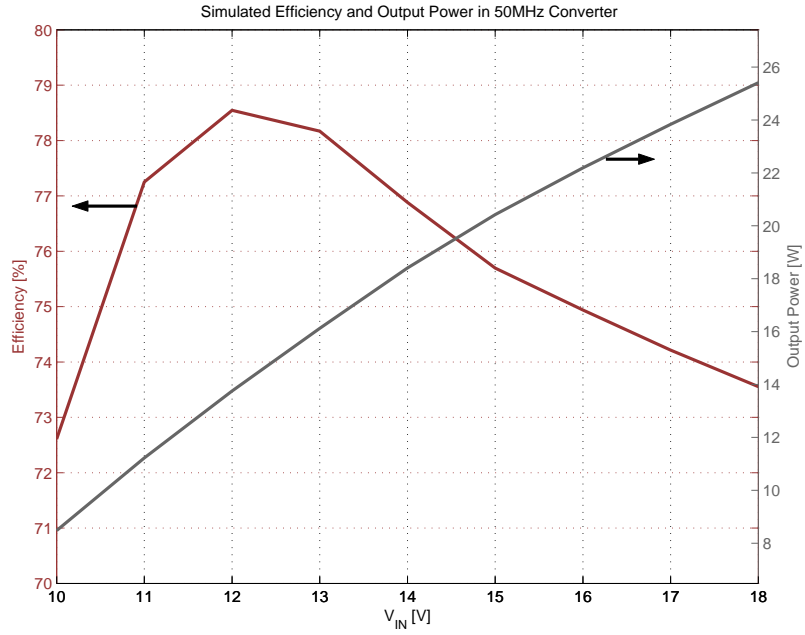
converter as a power stage in this operating regime. However, it also obscured gate losses. These were calculated based on the assumption of sinusoidal resonant gating and accounted for in the experimental efficiency data, a relatively minor effect for the PD57060.

Gating loss is not so easily dismissed in the case of the custom MOSFET. That device has a significantly larger gate time constant (table 4.1). Thus, a converter constructed at  $75\text{MHz}$  is not viable with this device. While the power stage works well, the gating loss is two orders of magnitude larger than the PD57060 at the same frequency, about  $460\text{mW}$ . Coupled with a practical gate drive, this could easily amount to a 5% reduction in efficiency. A significant improvement may be had by scaling the switching frequency to  $50\text{MHz}$ . Then the ideal sinusoidal gating loss is  $204\text{mW}$  and can be expected to cost only 1-2% in efficiency.

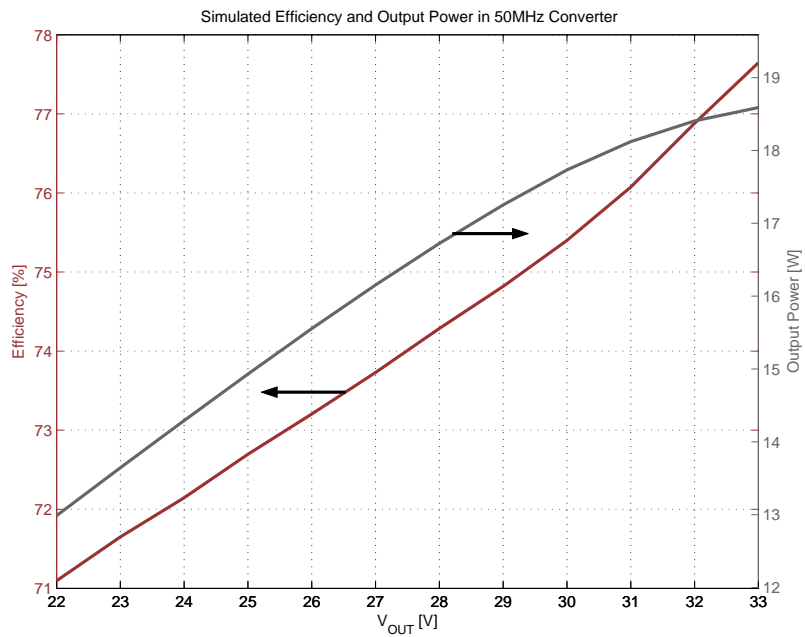
## 4.2 A Second Prototype

The purpose of this prototype is to demonstrate the feasibility of using a conventional power process at VHF frequencies as opposed to a discrete device optimized for RF. Using such a device opens the possibility of a future, completely integrated converter. Besides offering the benefits of low cost and small size, integration can also allow the optimization of a device to a particular converter. Unfortunately, there was no opportunity to optimize or even design the device in question for this implementation. It was a sample provided for the purpose of evaluating the feasibility of using the process. Thus the converter had to be designed around the switch taking into account its various strengths and shortcomings, a process which provides useful contrast with the first prototype. It also establishes the viability of using a power-process device in a VHF converter.

A larger gate time constant is not the only efficiency related consideration for the custom MOSFET. The  $R_{DS-ON}C_{OSS}^2$  product is 3.8 times larger than that of the PD57060. This implies larger device loss for a given output power. Fortunately, in the  $\Phi_2$  converter, the loss and output power is not fixed directly. Rather, a change in tuning point can alter the loss picture. In the first prototype, maintaining ZVS was favored over ultimate efficiency. Here, by tuning the rectifier to be resistive over some portion of the input voltage range, device shortcomings can be overcome to a degree.



(a) Efficiency and power vs.  $V_{IN}$ ,  $V_{OUT}=32V$



(b) Efficiency and power vs.  $V_{OUT}$ ,  $V_{IN}=14V$

Figure 4.8: Simulated power and efficiency.

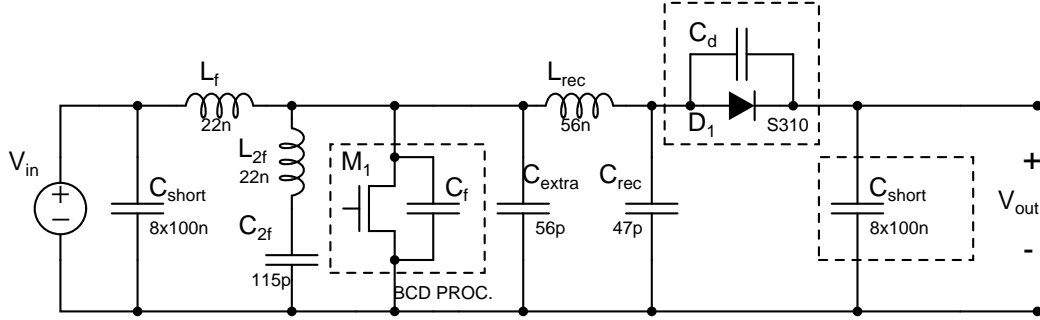
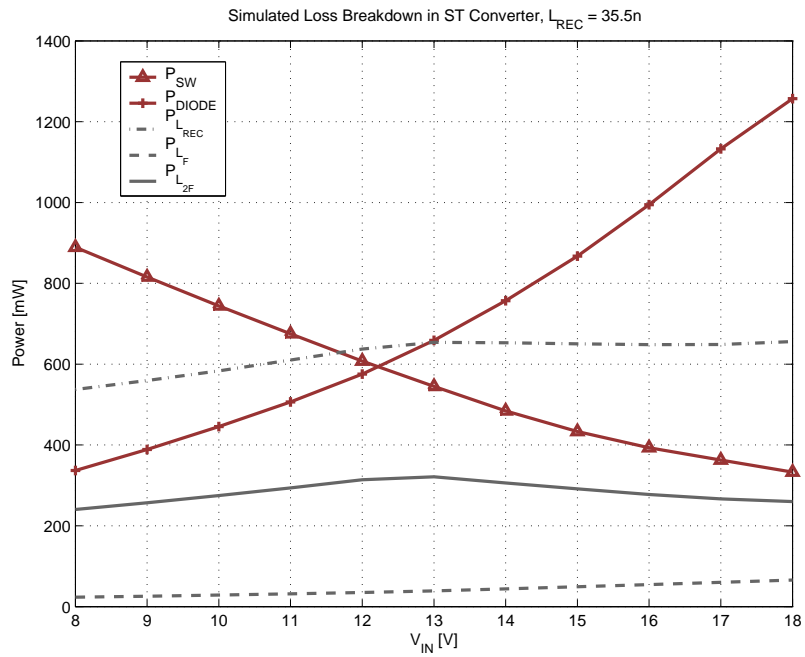


Figure 4.9: Final component values of  $\Phi_2$  inverter implemented with the integrated power process device.

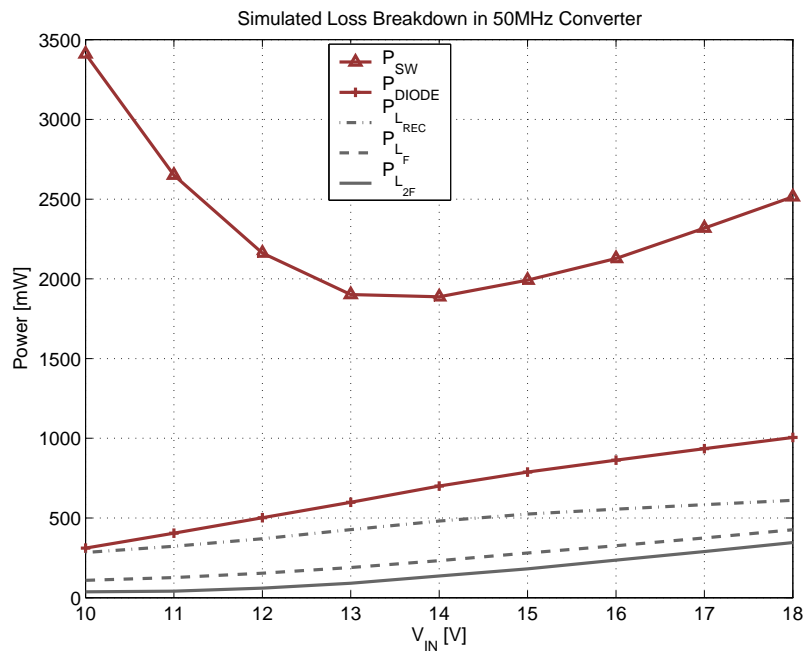
Rather than pursue a different operating point altogether, the converter was designed for the same application, an automotive LED headlamp driver. The input and output voltage ranges are the same,  $8V$ - $18V$  and  $22V$ - $33V$ , respectively and the output power remains in the  $20W$  range. In this particular converter, achieving reasonable efficiency in light of the poorer switch parameters demanded that the rectifier be tuned to look resistive. In this scenario the phase between the voltage and current fundamentals changes rapidly as the input voltage moves around the center voltage<sup>1</sup>. For instance, decreasing the voltage causes rectifier current to lead voltage (at the fundamental) and the rectifier to appear capacitive. This has two important effects. First, as mentioned in chapter 3, operating a rectifier with capacitive phase increases circulating current for a given output power, thus hurting efficiency. Secondly, the rectifier begins to look capacitive because the drive voltage falls off, but only over a narrow range, less than two volts in this case. Dropping the input voltage further actually causes the rectifier to stop functioning. The diode never turns on and converter output power and efficiency collapse.

While it is desirable to pick the nominal input voltage as the center voltage to maximize efficiency there, this will limit the low end of the input range. On the other hand, moving the center voltage too low means that efficiency at the nominal operating point will suffer. Here, with difficult switch parameters, the center voltage was chosen as  $12V$ . This causes a steep drop-off in efficiency at low input voltage and trims one volt off the usable operating range (i.e., input voltage must be greater than  $9V$ ). However, efficiency at the nominal operating point is 2% greater than if

<sup>1</sup>For the purposes of this discussion the term, “center voltage,” refers to the input voltage at which the rectifier fundamental voltage and current are in phase, assuming the nominal output voltage of  $32V$ .



(a) Loss breakdown with PD57060



(b) Loss breakdown with custom MOSFET

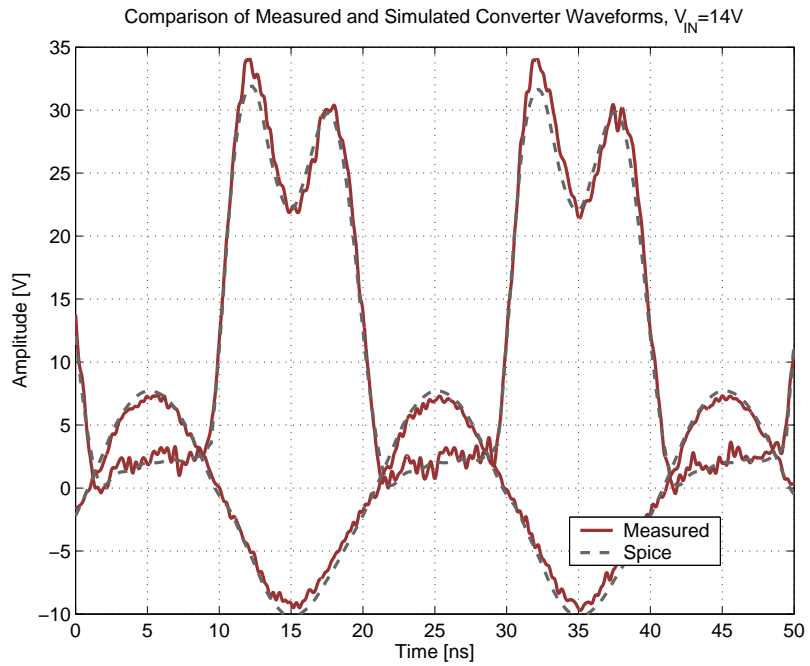
Figure 4.10: Breakdown of important loss mechanisms for each prototype (simulated)

the full input voltage range was maintained. Since  $8V$  is an unusually low bus in an automobile, such a scenario could be dealt with in a contingency fashion.

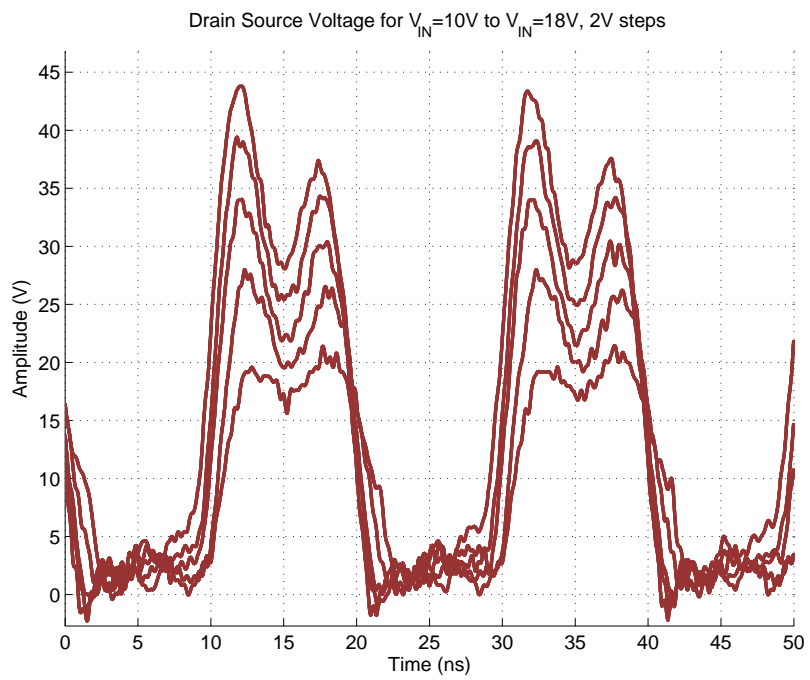
A design undertaken with the above considerations in mind produced the simulated power and efficiency results in fig 4.8. The plot in fig. 4.8(a) is interesting. The efficiency peaks around  $V_{IN} = 12V$  as intended, the point where the rectifier appears resistive. Higher voltage sees a drop in efficiency as the rectifier starts to look inductive and lower voltage sees a steeper drop while the rectifier heads to the capacitive regime. The final design component values are listed on the schematic in figure 4.9. In this design, the largest inductor is  $56nH$ , a significant reduction over the  $130nH$  inductor of the previous design. Also notable, is the much smaller  $L_F = 22nH$ , which is beneficial to transient performance.

A comparison between the loss breakdown of each prototype helps to clarify why the tradeoff between input voltage range and efficiency was necessary in this prototype as compared to the first design. In figure 4.10 one can see just how different the switches are. In the case of the custom small MOSFET, its losses greatly outstrip the others, even at the lower frequency where switch displacement losses should fall and inductor  $Q$ s are relatively poorer. This is in contrast to the converter that uses the PD57060, where the diode loss exceeds the switch loss at high input voltage. The latter is partially due to the larger ringing in the  $75MHz$  converter. In the second prototype, the diode losses are roughly 20% lower despite higher output power. It should be noted that since  $C_{OSS}$  and circulating currents are proportional, the device output capacitance figures into device loss as a square term. The ability to control the device area, which is ordinarily available to an integrated process could improve the picture significantly if the converter operating point is assumed fixed.

The construction technique was the same as the first prototype, a 4-layer board minimizes parasitic inductance. A photograph of this prototype is shown in fig. 4.13(b) and a detailed schematic and PCB artwork are shown in appendix B. In this case, the gate drive and control circuits are located on the board. Their presence does not affect the power stage operation because of extensive use of the ground planes. Detailed information on the gate drive and control circuits is covered in chapter 5. Tuning is performed in identical fashion, with an impedance analyzer to verify the drain-source port impedance match to simulation. The result, when the converter waveforms are plotted next to their SPICE compatriots, is consistent with the good match observed with the previous prototype (see fig. 4.11(a)).

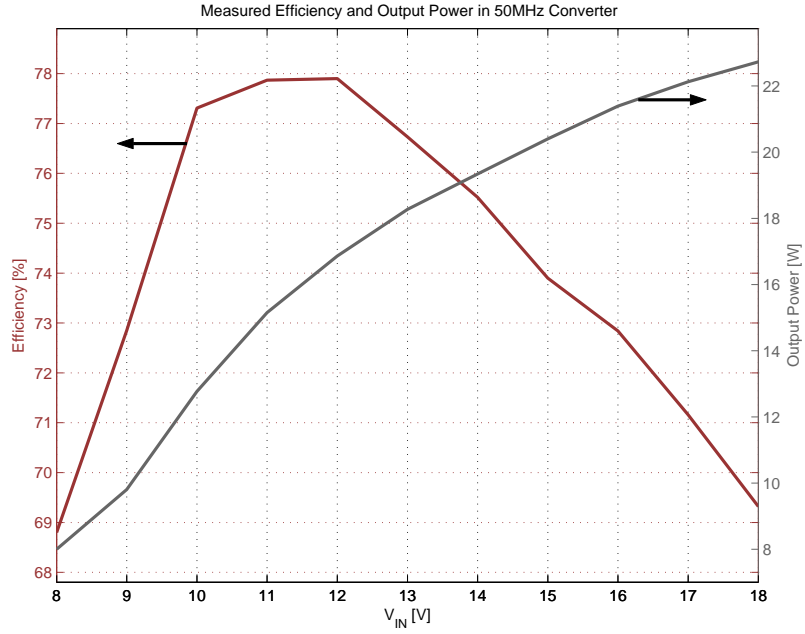


(a) Comparison of measured and simulated waveforms

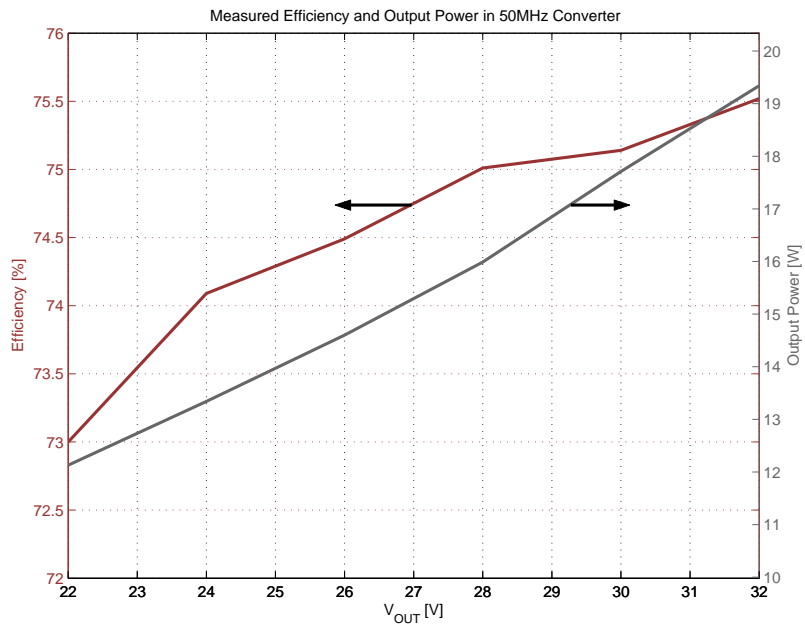


(b) Drain waveform progression with input voltage

Figure 4.11: Experimental waveforms in the 50MHz converter

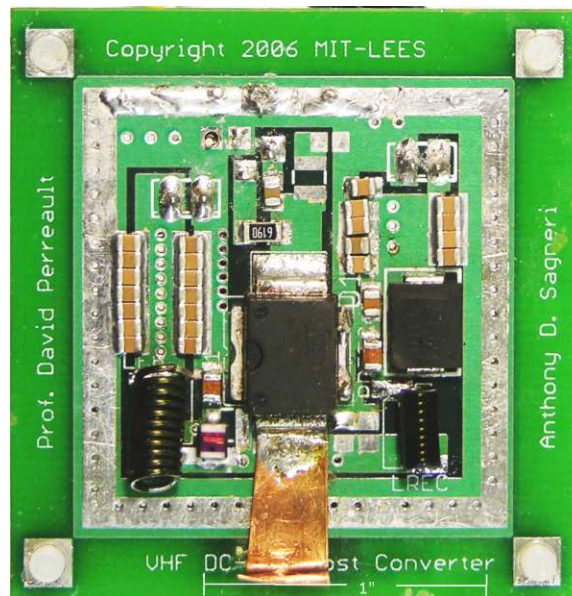


(a) Measured power and efficiency vs.  $V_{IN}$

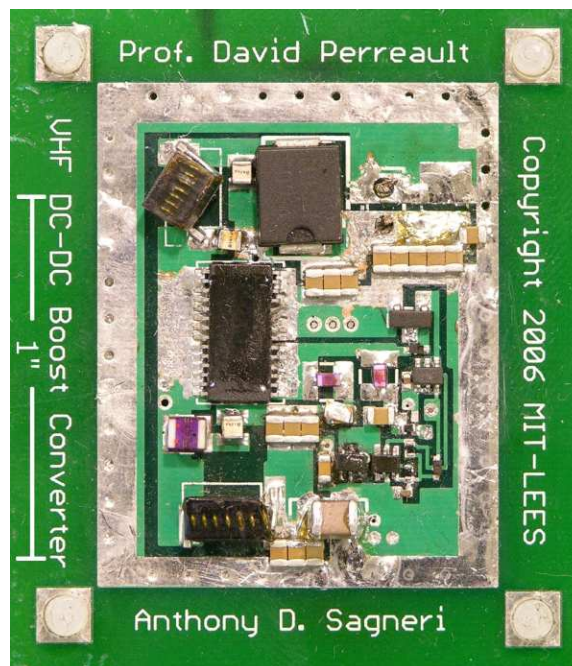


(b) Measured power and efficiency vs.  $V_{OUT}$

Figure 4.12: Experimental output power and efficiency



(a) 75MHz converter with ST PD57060 switch



(b) 50MHz converter with custom MOSFET

Figure 4.13: Converter pictures. Note the calibration marks indicating a dimension of 1". While the images remain rectified, they are scaled relative to one another. The top converter is actually larger, each side corresponding roughly to the long dimension of the converter in fig(b).



The experimental drain waveforms for various input voltages are plotted in fig 4.11(b) followed by the measured output power and efficiency in fig. 4.12. The same characteristic peak in efficiency vs. input voltage is observed. The efficiency at the peak is within 1% of the simulated value, but it occurs at a slightly lower voltage. This means that the actual converter can be operated down to 8V, but the efficiency leaves something to be desired. It also contributes to a 3% lower efficiency at 18V, rather than the 1% observed at the peak. Finally, pictures of both converters are included for requisite ogling.

It's worth noting that both converters using the  $\Phi_2$  topology have peak voltage stresses significantly less than an equivalent class-e design. Stresses below 45V, rather than the 65V<sup>+</sup> expected in a class-e, are advantageous where the use of integrated devices is desired. This matches well with the elimination of bulk inductance characteristic of other resonant designs. This again makes the case for realizing an integrated implementation, particularly in light of the reasonable efficiency obtained with an un-optimized power process device.



## Closed-Loop Operation

---

POWER conversion, in the dc-dc arena at least, almost exclusively demands some form of closed-loop control. The need to impose an output voltage or current under changing load and input conditions assures it. In RF converter topologies including the  $\Phi_2$  converter, this can be a somewhat thorny issue. The requirements for fixed duty ratio and load run counter to the notion of regulation, often a change there is tantamount to poor efficiency. As outlined in chap. 1, separation of the energy storage and regulation functions by choice of control strategy is VHF converter catharsis. In much the same way that soft-switching utilizes parasitics rather than fighting them, control using a “bang-bang” scheme takes advantage of the one thing that a VHF converter with minimal energy storage has in spades; transient response.

### 5.1 Control Scheme

The rough-out of the control scheme introduced in the first chapter is redrawn in fig. 5.1. A  $\Phi_2$  dc-dc converter supplies the load which is shunted with bulk capacitance. The output voltage has a sawtooth ripple characteristic, rising while the power stage is energized and falling otherwise. This, in turn, is subject to the presence of the sinusoidal waveform produced by the gate drive, itself controlled by a logic signal. The logic signal originates at the output of a comparator with hysteresis that determines the output voltage and its excursion (i.e. the ripple).

Under the assumption of small ripple, the converter runs at nearly the same operating point over a modulation cycle, delivering constant power at its output. Thus, bang-bang control modulates power delivered to the load via the fraction of the time that the *converter* is on, rather than the switch (as in a conventional boost). Further, by also avoiding frequency control methods, the energy storage elements can be tuned

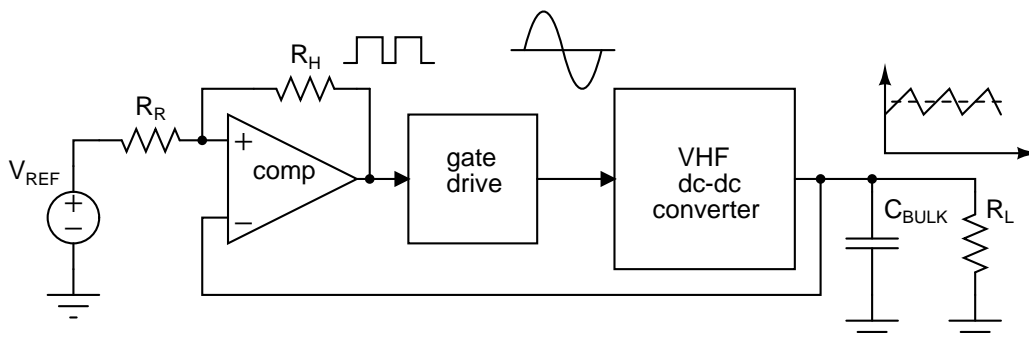


Figure 5.1: **Schematic depiction of VHF converter under on-off modulation. The closed-loop system keeps output voltage constant allowing the converter to deliver a constant power (effectively it sees a constant load) at it's most efficient point. Actual power delivered to the load depends on the duty ratio of the control signal.**

explicitly for maximum efficiency at the desired operating point, rather than needing to account for some control range as well. Another advantage of this scheme is that the load range is enhanced. Since resonating losses don't necessarily scale with output power, the light load performance of many resonant converters suffers. In the bang-bang scheme, the converter spends more time turned off at light load, effectively scaling resonant losses with output power.

Sizing the bulk capacitance demands careful consideration. The load, converter output power, ripple, and bulk capacitance determine the modulation frequency. Increased modulation frequency comes with the penalty of reduced efficiency, but a lower frequency includes a volume penalty as the output capacitance must be increased given the same ripple. Similarly, achieving smaller output voltage ripple increases the modulation frequency and associated losses. The peak modulation frequency occurs when the rising and falling slopes of the output ripple are equal and it falls off at the load extremes. The slopes will be equal when the converter sources twice as much power when it is on as the load uses, or 50% duty ratio. While there are multiple conditions that result in 50% duty ratio, only one set results in the maximum modulation frequency for a given bulk capacitance and ripple. When the load is drawing exactly half the converter's rated output power at maximum input voltage, the duty ratio is 50% and modulation frequency is at a maximum. A further increase in the load slows the rising ramp. The move away from 50% duty ratio cannot be reestablished because the converter is already at maximum output power. Similarly, a lighter load causes the output to ramp down more slowly. If the converter

input voltage is reduced until the duty ratio is 50% once more, then both the rising and falling ramps are slower than the half-load case. Thus once the ripple and load range are known, the maximum modulation frequency can be set by selecting the bulk capacitance at half-load.

The maximum modulation frequency does not necessarily correspond to the greatest loss due to modulation. Instead, conditions where the duty ratio is very small or very large can have higher loss at a given frequency. This arises because over very short periods the converter is spending less time in steady-state operation where its efficiency is greatest. Light-load efficiency may suffer in this regime, for instance. The load range may be extended by ensuring that both the gate driver and the converter have fast transient response so that steady-state operation is reached as quickly as possible.

## 5.2 A Resonant Gate Drive

The constant duty ratio and fixed operating point of the  $\Phi_2$  converter are a good match with a resonant gate drive. At VHF, the latter offers much higher efficiency than the totem pole drivers common at lower frequency. While the power lost to simple hard gating can be estimated as  $P_{gate} = C_{ISS}V_G^2f$ , as in chap. 2, this does not include losses in the driver itself, such as direct path loss caused by overlap at device turn-on, which becomes important at VHF. Even so, under sinusoidal resonant gating, the loss is closer to  $P_{gate} = (\pi C_{ISS}V_{ac}f_{SW})^2R_G$  as in chap. 3 which can be much lower than the hard gating case.

$C_{ISS}$  vs. bias voltage for the custom MOSFET is plotted in fig. 5.2. Since the gate needs to swing to at least 6V to ensure the MOSFET is fully enhanced, the effective  $C_{ISS}$  is 276pF. The equivalent gate resistance is 1.7 $\Omega$  for an approximate gate time constant of 469ps. These values are used in computing the loss for both hard gating and sinusoidal resonant gating in table 5.2. In evaluating the sinusoidal gating loss, a higher voltage amplitude was used, 8V, as this is necessary to achieve the proper duty ratio. Even with the higher drive amplitude, the total loss with resonant gating is 204mW, about 2/5 of the hard gating loss. At output power levels around 15W, this amounts to about a 2% improvement in converter efficiency.

Besides high efficiency, there are several other constraints on gate drive operation.

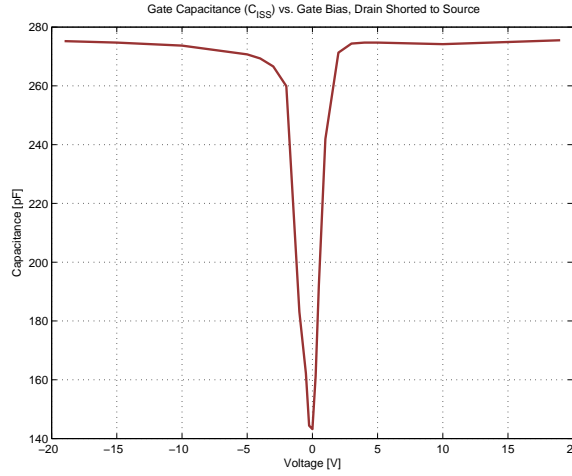


Figure 5.2: A basic resonant gate drive.

Component	Hard Gating	Sinusoidal Resonant Gating
$f_{SW}$	50MHz	50MHz
$C_{ISS}$	276pF	276pF
$V_{Gate}$	6V	8V
$R_{Gate}$	N/A	1.7 $\Omega$
Power	497mW	204mW

Table 5.1: **Hard gating requires more than twice as much power for the custom MOSFET even when the larger gate drive amplitude is accounted for.**

First, it must start rapidly to be compatible with the control scheme. Any additional delay introduced by the gate drive in start-up or shut-down will narrow the load range hurting light-load performance. Where integration is the focus, the scheme should use a minimum number of components or use components that can be readily integrated. For instance, while inductors will be difficult to integrate, transistors that implement basic logic functions are readily fit on die.

One potential resonant scheme is shown in fig. 5.3(a). The minimal component count, a single inductor and a totem pole driver, should offer the least challenge to integration. However, efficiency is a problem. Since all of the resonating current must pass through the totem pole driver, the channel resistance of those devices is important. If the totem pole driver is modeled as a voltage source and equivalent output resistance, then the gate loss becomes  $P_{gate} = (\pi C_{ISS} V_{ac} f_{SW})^2 (R_G + R_I)$ . Since the totem pole devices must be small to avoid *their* gating loss,  $R_I$  tends to be several times  $R_G$ , and the total loss quickly exceeds that of the hard gating case.

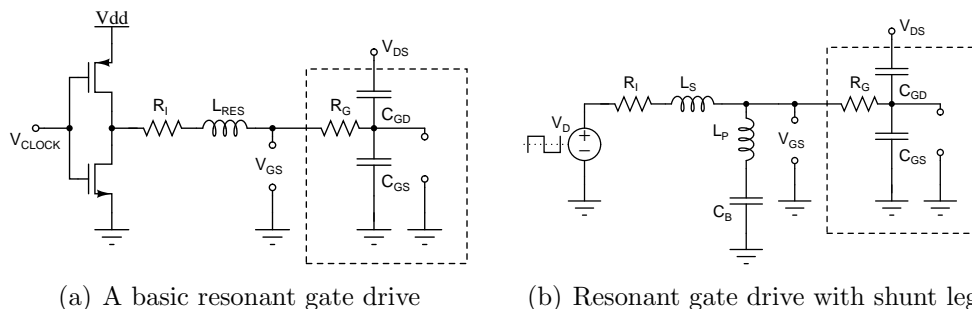


Figure 5.3: **The affect of  $R_I$  on gate drive efficiency can be reduced by introducing a shunt leg to conduct some of the resonating current.**

The scheme of fig. 5.3(b) first presented in [32] diminishes this problem. Instead of a single inductor, an additional shunt branch including  $L_P$  and a blocking capacitor  $C_P$ , carries a portion of the resonating current, reducing the loss in  $R_I$ .  $R_I$  and the voltage source  $V_D$  represent a parallel bank of CMOS inverters. Their much smaller input capacitance can be hard-gated with minimal loss. The output voltage from the inverter bank is limited to  $V_{dd}$ , but this is not a problem because the resonant circuit is tuned to provide gain at the fundamental. In [32] tuning was accomplished by choosing  $L_P$  to be resonant with  $C_{ISS}$  below  $f_s$ , effectively reducing the equivalent gate capacitance. The transfer function from the drivers to the gate could then be set by choice of  $L_S$ . In this scheme better efficiency is realized for a larger series inductance provided the necessary gain from the driver to the gate could be achieved. One additional constraint requires that the drain to gate transfer function be minimized to ensure the circuit can be shut off. If it is too large, drain voltage fed back through  $C_{GD}$  can result in sustained oscillations.

Essentially the same tuning method was applied to the  $\Phi_2$  converter gate drive. However, a pull-down switch added in parallel to the main gate ensures the main switch cannot self-oscillate when a shutdown command is issued. Freedom from this concern allows a wider exploration of the tuning regime. By tuning the system so the drain to gate transfer function has a phase close to  $180^\circ$ , it was found that efficiency could be improved. This is because feedback from the drain helps to sustain the oscillation. It cannot, however, sustain it completely because the gain is not large enough. There are some important limitations that arise in this scheme. First, while better efficiency is achieved by increasing the series inductor  $L_S$  and reducing  $L_P$ , this slows the gate drive startup. Since slow startup can reduce the closed-loop efficiency of the overall system, it must be considered carefully. Another result of straying too far towards a

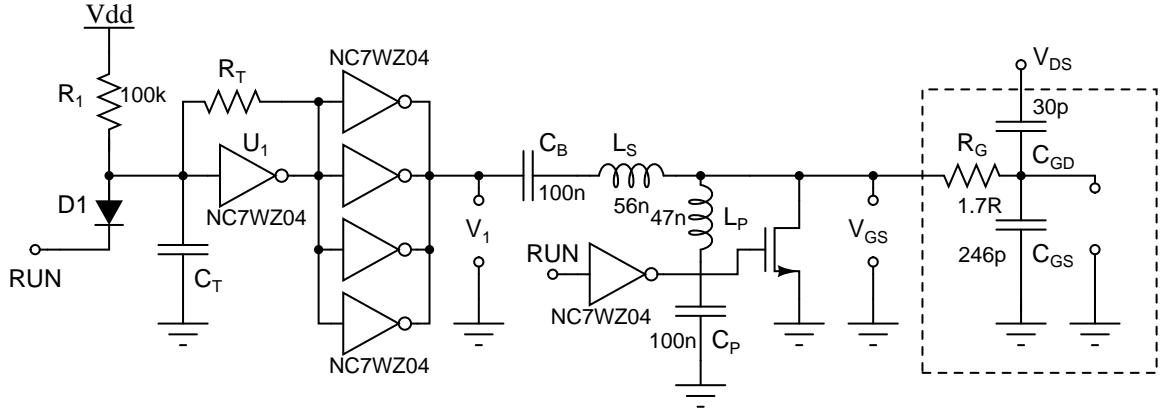


Figure 5.4: **The final gate drive circuit.**

large series inductor is that the CMOS drivers can actually be overwhelmed by feedback from the drain. When this happens, the oscillation frequency is not dictated by the ring oscillator.

The final circuit (fig. 5.4) is driven by a bank of four paralleled Fairchild NC7WZ04 CMOS inverters. Paralleling ensures the component power dissipation limits are not exceeded and reduces the source resistance. The paralleled inverters are in turn driven by a single-inverter ring oscillator formed by  $U_1$ ,  $R_T$ , and  $C_T$ . The pull-up resistor  $R_1$  ensures that the oscillator does not reach a metastable state at start-up. Diode  $D1$  allows control of the gate drive as a low signal at its cathode pulls  $U_1$ 's input low halting oscillation. The additional parallel MOSFET ensures rapid on-demand collapse of the gate voltage.

The gate drive mated to a  $\Phi_2$  converter allows effective logic-level control of the output. The converter start-up is shown in fig. 5.5. After a logic level command is issued, there is an initial delay of approximately  $42ns$  while the gate drive starts. Once the switch threshold is exceeded, the power stage begins to resonate, reaching steady state in about 7 cycles. Steady state is achieved in approximately  $175ns$ . At the shut-down command, the converter takes longer to ring down, but the total time is still only  $400ns$  which can be seen in fig. 5.6. The total start-up and shut-down time of  $575ns$  suggests that the converter can be modulated above  $1MHz$ . This was tested open-loop by modulating the converter at three different duty ratios and across frequency from  $50kHz$  to  $5MHz$ . The results are plotted in fig. 5.7. The impact of modulation on efficiency is well behaved to about  $1.5MHz$ . The efficiency at each duty ratio drops in a roughly linear fashion. The steepest drop occurs for the 20%



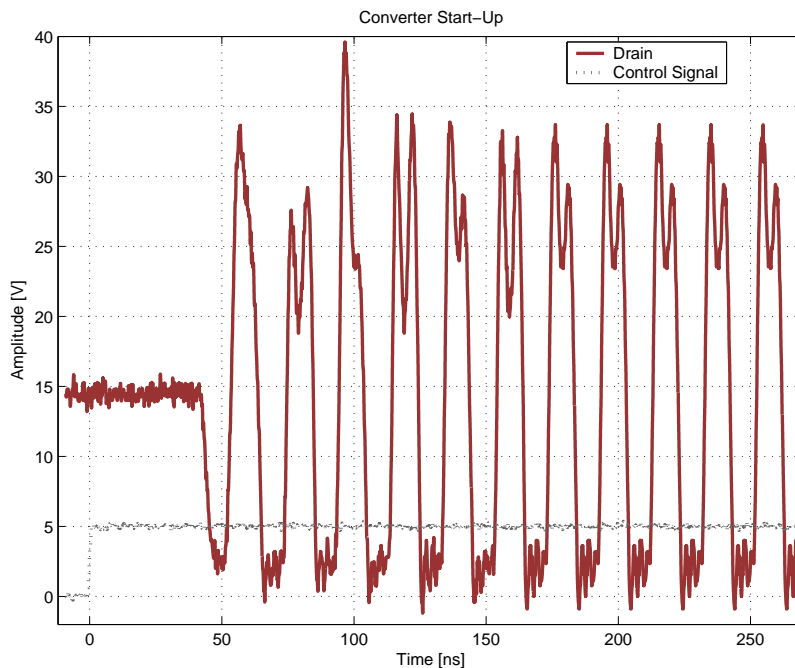


Figure 5.5: **The converter starts rapidly on command. After a  $42\text{ns}$  delay the gate drive turns on the main switch and the converter reaches steady state in about 7 cycles. The total start-up time is  $175\text{ns}$ .**

modulation duty ratio, which is expected because the converter will be in steady-state for the shortest period of time and therefore start-up and shut-down “end effects” are most significant. Likewise, the 80% modulation duty ratio case falls the slowest because the converter spends relatively more time in steady-state. Beyond about  $2.5\text{MHz}$ , the converter never reaches steady-state for any duty ratio, and this gives way to the apparently erratic efficiency numbers. The main conclusion to be drawn from fig. 5.7 is that the converter may be modulated on and off at a rate faster than  $700\text{kHz}$  for about a 1% drop in efficiency.

The gate drive was supplied by a  $5\text{V}$  source for testing and powered from the input via a small buck regulator in the final converter efficiency measurements. Figure 5.8 plots the gate drive power vs. converter output power and input voltage. The gate drive power ranges up to  $600\text{mW}$  at full load where the duty ratio is close to one. This power level is roughly a factor of three larger than the ideal calculation of  $204\text{mW}$ . A major culprit is  $U_1$  the ring oscillator, which uses nearly  $200\text{mW}$ . On closer examination, the output signal of  $U_1$  does not swing over the full voltage range, suggesting that the device spends a significant amount of time in the linear range

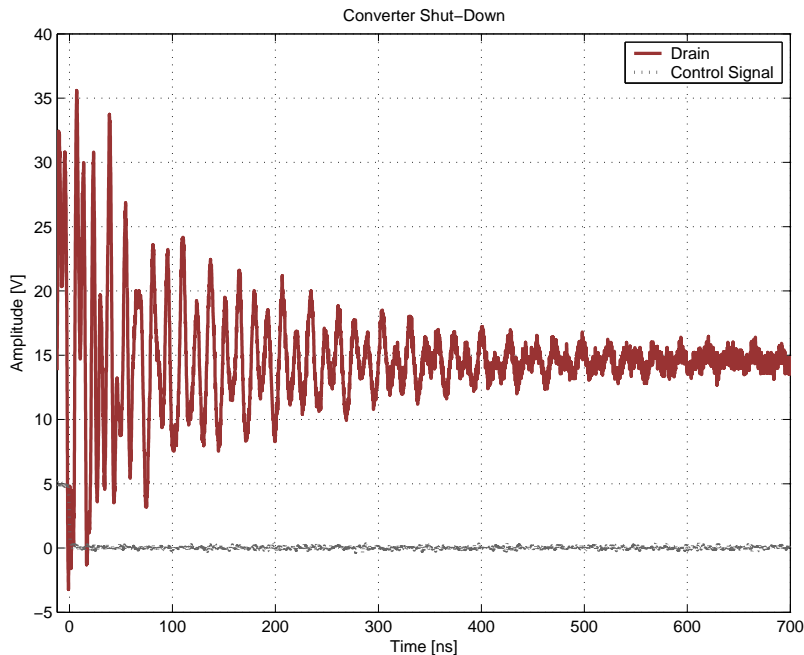


Figure 5.6: **The converter shut-down begins at 0ns when the control signal falls to zero and requires approximately 400ns.**

contributing to direct path loss. Further, because  $U_1$  provides the drive signal for the other inverters, it increases their loss. Running the paralleled inverters directly from a signal generator improves the situation. The total loss is closer to  $260mW$  including the estimated power to drive the inverter gates. A different oscillator scheme, not implemented here, would improve overall gate drive performance significantly. Even the results obtained, however, are better than hard gating. It starts with  $500mW$  of loss in the gate of the main switch alone. Accounting for losses in the driver itself will easily push the total over  $600mW$ .

### 5.3 The Controller

To achieve closed-loop control the simplest controller that fully exploits the capabilities of the converter is desired. A comparator with hysteresis is such a scheme. The controller schematic is presented in fig. 5.9. A classic circuit is used to realize a voltage comparator with hysteresis. The width of the hysteresis band,  $V_H$  is set by the two resistors,  $R_H$  and  $R_F$  using equation 5.1 which is readily found using superposition.

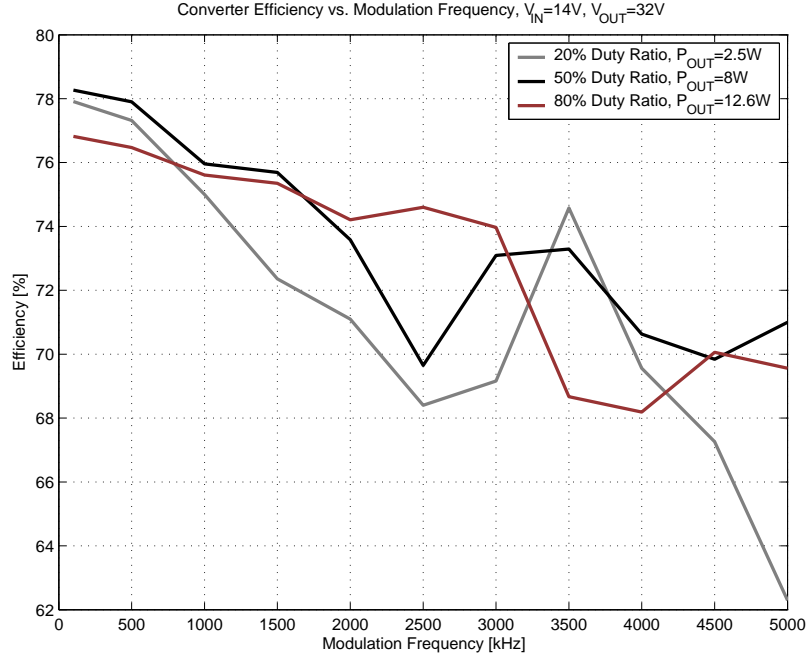


Figure 5.7: As the modulation frequency is increased, efficiency declines. At smaller duty ratios, this effect is more pronounced. Beyond  $1.5\text{MHz}$ , the converter never reaches steady-state, the reason for the erratic efficiency numbers.

$$V_+ = V_{REF} \frac{R_F}{R_H + R_F} + V_{OUT} \frac{R_H}{R_H + R_F} \quad (5.1)$$

$V_+$  is the voltage at the positive input of the comparator. It has a fixed portion due to the reference voltage, and a changing portion that attains two stable values when  $V_{OUT} = V_{dd}$  and  $V_{OUT} = 0$ . Thus  $V_H = V_{dd}R_H/(R_H + R_F)$ .

The circuit design in fig. 5.9 is straight forward. The ADR394 is a  $4.096\text{V}$  precision reference, selected as purposely close to  $V_{dd}$ . This ensures that the attenuation provided through the divider network  $R_1$  and  $R_2$  is not too large. Then the hysteresis at the controller will be as large as possible for a given ripple voltage, a benefit in terms of immunity to pickup and noise. With a desired output voltage of  $32\text{V}$ ,  $R_1$  and  $R_2$  were selected respectively as  $1.5\text{k}\Omega$  and  $10.5\text{k}\Omega$  for a divider ratio of 8. This keeps the voltage at the input of the comparator within the component ratings. The capacitor  $C_{LP}$  forms a low pass filter with  $R_1$  and  $R_2$  and was selected to give a corner frequency of about  $10\text{MHz}$ . The TLV3501 has an internal hysteresis of  $6\text{mV}$ ,

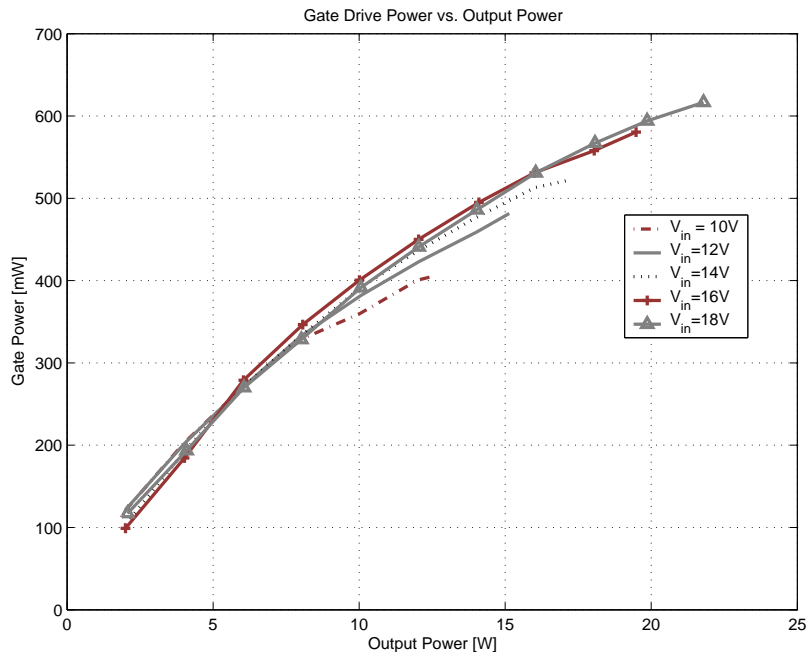


Figure 5.8: Gate drive power increases with converter output power because converter on-time rises.

an additional  $6mV$  was added with the choice of  $R_H$  and  $R_F$  as  $300\Omega$  and  $220k\Omega$  respectively. This results in close to the expected hysteresis of  $100mV$  at the converter output. It was necessary to provide generous bypass to the reference and the comparator to avoid problems during switching.

## 5.4 Closing the Loop

With all the elements in place, closing the loop is simply a matter of connecting the various blocks as illustrated in fig. 5.1. A bulk capacitance of  $40\mu F$  was selected to set the peak modulation frequency at a conservative  $225kHz$ . Figure 5.10 shows the converter waveforms during operation. The output voltage is regulated to about  $30.9V$  rather than  $32V$ , but this could be easily fixed by changing either  $R_1$  or  $R_2$ . The rapid response of the converter drain voltage to the control signal is evident in the top plot. The resulting output voltage ripple is displayed in the bottom plot. At  $V_{IN} = 14V$ , the modulation frequency at this load is approximately  $177kHz$ . Notice that the duty ratio is near 50% and this is the peak frequency for this value of  $V_{IN}$ .

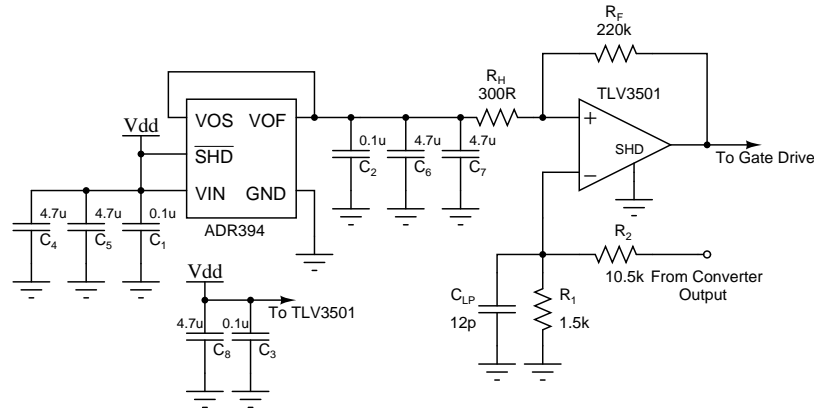
Figure 5.9: **Controller Schematic**

Figure 5.11 plots the modulation frequency of the converter over the input voltage range and load range. As expected, the peak frequency occurs when  $V_{IN} = 18V$  and the converter is operating at about half load. Closed loop efficiency plots with and without gate drive and control losses are plotted in fig. 5.14. Comparing the two plots shows that the gate drive and control losses account for about a 2.5% reduction in efficiency over the load and input voltage ranges. The best overall efficiency is achieved at a converter input of 12V which is where the rectifier operates closest to resistive operation. The efficiency at low output power falls off as a result of the small duty ratio preventing the converter from achieving steady state.

The voltage transient response was tested with a simple load constructed as in fig. 5.12. The resistors are chosen to provide 2W and 12W loads and the MOSFET allows rapid transition between the two. When the load is driven with a signal generator, the converter responds by changing the modulation frequency. The output voltage never leaves the hysteresis band (figs. 5.13(a) and 5.13(b)). The effect on output voltage shows up merely as a slope change in the ripple.

## Closed-Loop Operation

---

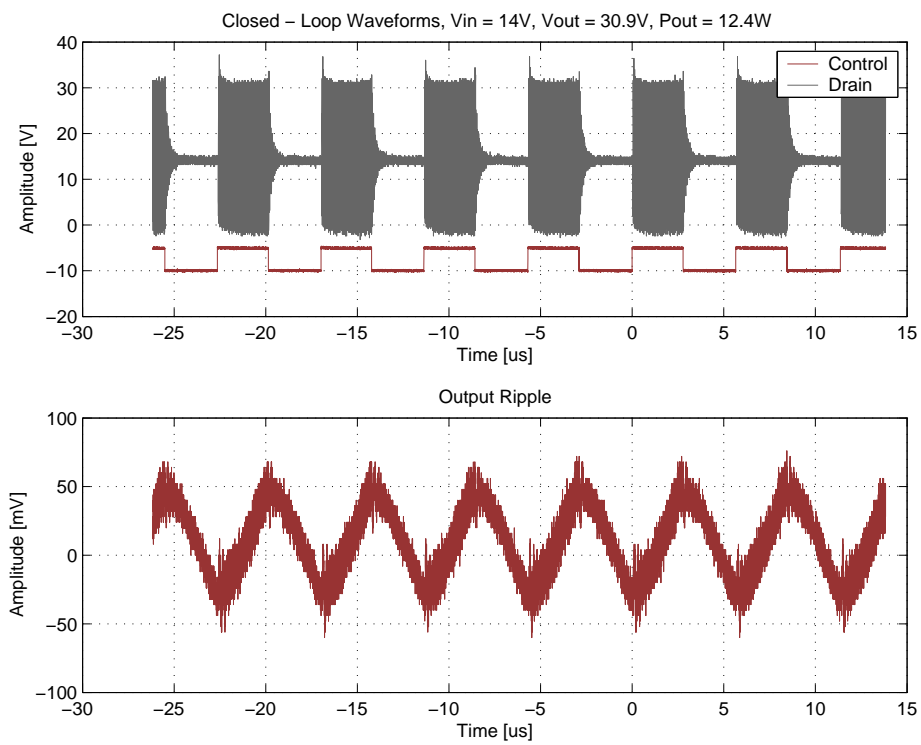


Figure 5.10: Converter under closed-loop control. At  $V_{IN} = 14V$  and a load power of  $12.4W$ ,  $F_{MOD} = 177kHz$ .

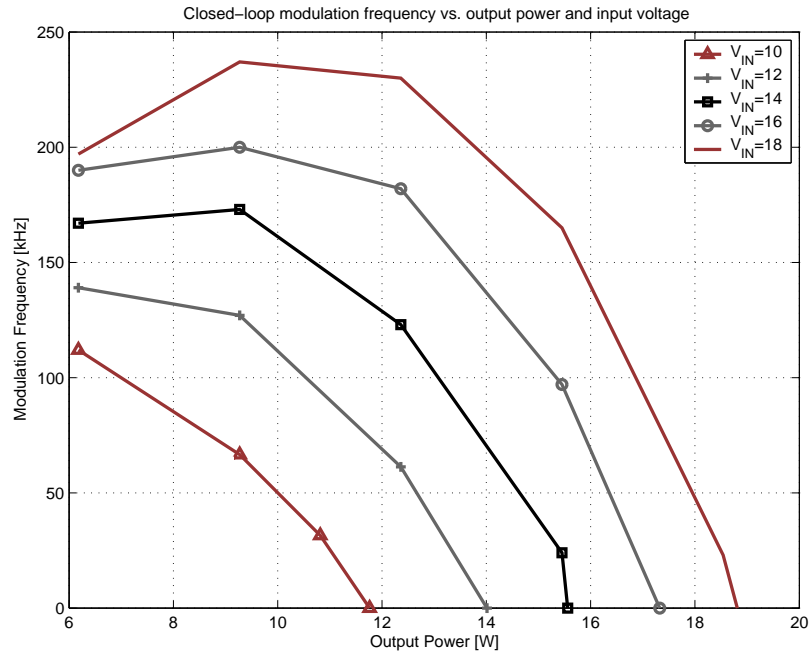


Figure 5.11: Modulation frequency dependence on load and input voltage

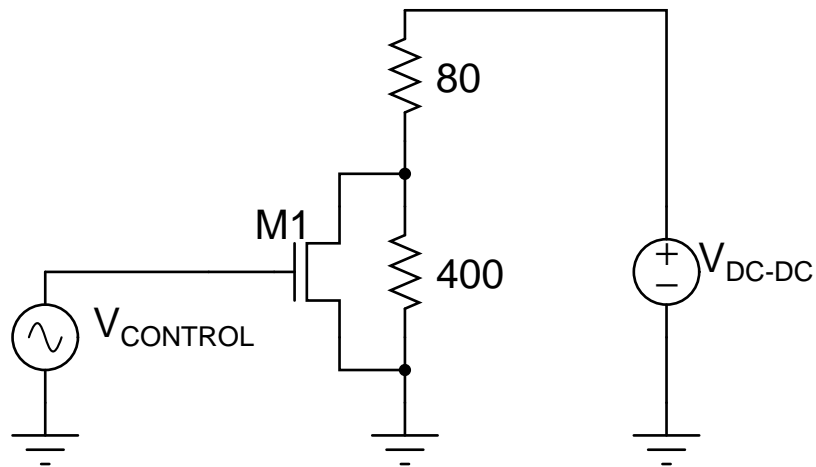
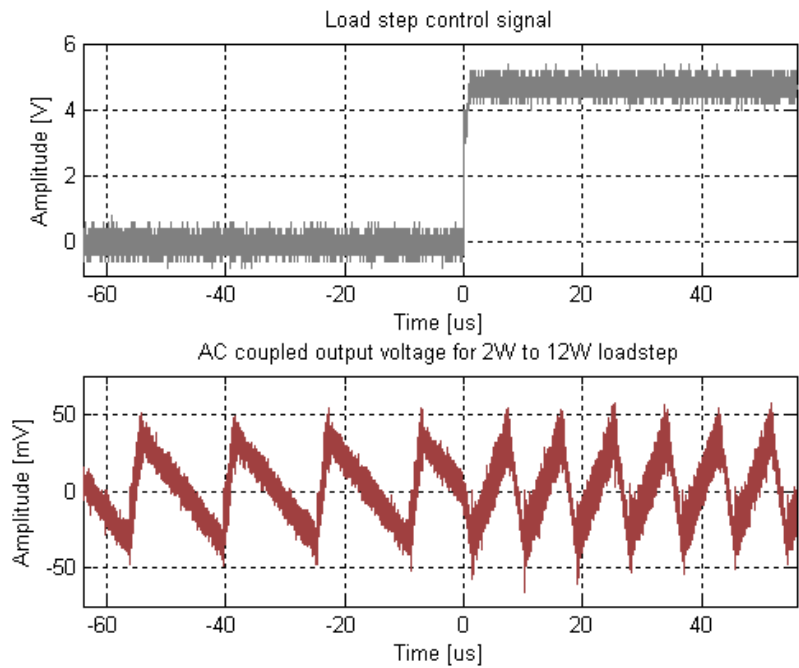
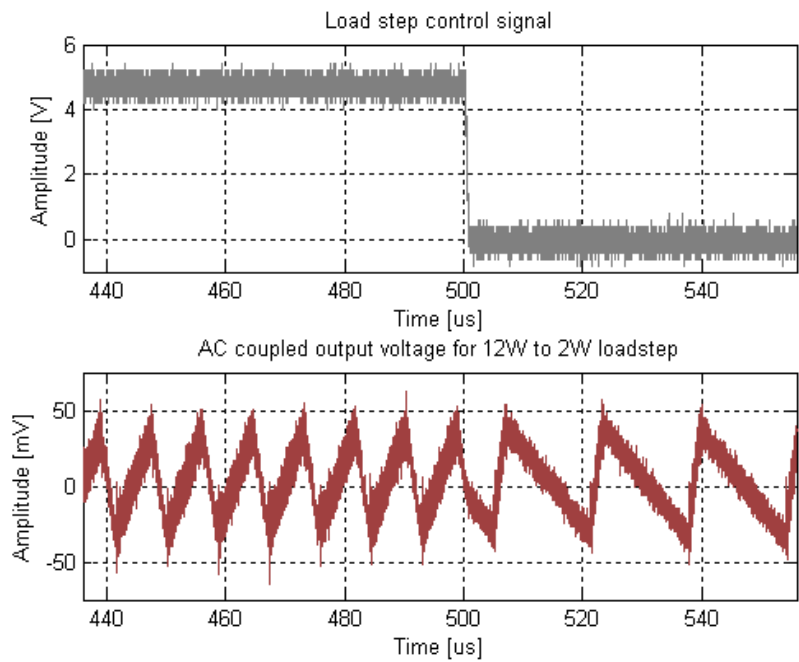


Figure 5.12: Load used for transient measurements



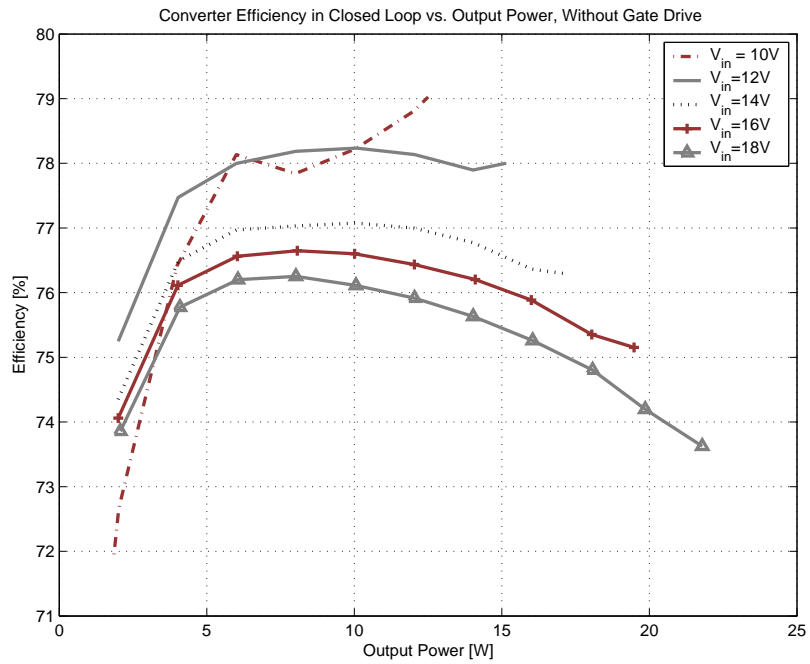
(a) 2W to 12W load step



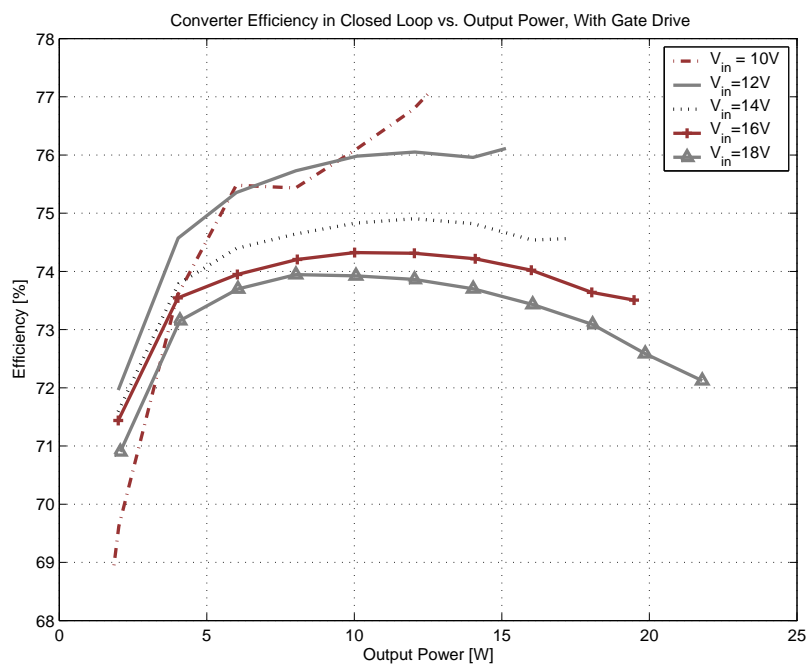
(b) 12W to 2W load step

Figure 5.13: In the transient response to a load step under closed-loop control, the only visible change is in ripple slope during the load change.





(a) Efficiency without gate drive loss



(b) Efficiency including gated drive loss

Figure 5.14: Closed-loop efficiency with and without gate drive loss. Gate drive and control losses account for approximately a 2.5% reduction in efficiency.



# *Conclusion*

---

**T**HIS thesis explores resonant power conversion techniques suitable for VHF resonant dc-dc boost operation using a conventional power process as the main semiconductor switch. At VHF frequencies, energy storage requirements diminish to the point that it becomes possible to use air-core magnetic components. Combined with the ability to use an integrated switch, realization of a fully integrated converter looks ever more tenable.

## **6.1 Thesis Summary**

Chapter 1 introduces the concept of energy storage as a limiting factor in reducing converter volume. Using conventional techniques to increase frequency can reduce energy storage requirements at the cost of efficiency. Resonant conversion techniques offer a way around these problems, but only over a narrow load and input voltage range. Separating the energy storage and control functions largely overcomes this limitation and is the bulwark on which the balance of the thesis proceeds.

Chapter 2 discusses a new resonant inverter topology, the class- $\Phi_2$  inverter. By exploiting waveshaping techniques available in resonant systems, the  $\Phi_2$  inverter can realize efficient switching at much lower peak stress than existing designs such as the class-E inverter (in the ideal case a peak voltage stress of less than two is attainable compared with the class-E inverter's 3.6). Operating characteristics are delineated along with design criteria that fit nicely into the discussion that follows in chapter 3.

Chapter 3 treats the  $\Phi_2$  dc-dc converter. An efficient means of rectification is found and exploited in the series-loaded resonant rectifier. The behavior of the rectifier with input voltage and bias is outlined, emphasizing the relationship between dc bias and

ac amplitude. These determine the ratio of ac and dc power delivered to the load. Ultimately this relationship can be treated as roughly orthogonal for design purposes. This allows a strategy whereby the ac and dc power are considered in the design of the rectifier, but only ac power need be considered for inverter design. When the two are connected, dc power delivered through the rectifier is appropriate to the ac design power. Any deviation is easily corrected using the techniques of magnitude and phase matching developed in chapter 2.

Chapter 4 presents experimental  $\Phi_2$  power stages, one implemented with an off-the-shelf power MOSFET and the other in a standard BCD power process. The flexibility of the  $\Phi_2$  topology is illustrated in the design tradeoffs necessary to accommodate the different sets of switch parameters. The small size of the energy storage components and respectable efficiencies achieved make a case for the  $\Phi_2$  converter as candidate for integration.

Chapter 5 details some ancillary considerations in gate drive and control and presents results for a closed-loop converter. The transient performance of the power stage is more than sufficient to implement a bang-bang architecture with stellar load-step performance. Modulation frequency vs. efficiency is explored revealing that the  $\Phi_2$  converter running at a switching frequency of  $50MHz$  can be modulated at nearly  $1MHz$  for only a 1% efficiency penalty. This allows for relatively small bulk capacitance which can be reduced even further if ultimate efficiency is not a mandate.

## **6.2 Thesis Conclusions**

The  $\Phi_2$  Boost converter topology is a viable means to realize VHF switching frequencies under the constraints imposed by integrated devices. The relatively low peak voltage stress is a key enabler in this respect, squeezing the voltage to within the breakdown limits typical of an integrated process. With some flexibility in determining how the conduction and displacement currents manifest for a given operating point, a range of switches may be accommodated. For a given tuning point, efficiency may be improved by adjusting the characteristic impedance of the network until the total energy stored over a cycle is minimized. Further, component values can be traded off to realize a number of goals. Characteristic impedance can be lowered to decrease component value (i.e. for co-packaging or integrated designs) at the expense of efficiency. Transient performance may be improved by a similar means, though

even a relatively large  $Z_O$  converter performs greatly in excess of most conventional hard-switched converters. The minimal component count and ease of control also count advantageously for the  $\Phi_2$  converter where reduction in size is concerned.

## 6.3 Future Work

The VHF  $\Phi_2$  dc-dc boost converter presented in this thesis represents only the tip of the iceberg with respect to the potential of the  $\Phi_2$ . For that matter, similar resonant schemes operating under the premise of separating energy storage and control may prove ideal under a host of applications.

Where integration is concerned there are many opportunities. To begin with, it remains unclear what constitutes an optimal switch for a given  $\Phi_2$  converter. And as a wider question, given a *process* rather than a pre-fabricated switch, converging on an optimum converter and switch design is even less clear. In both of these cases, one might attack the problem by first establishing the relationships among conduction and displacement current in a  $\Phi_2$  converter for various tuning points, thereby establishing a basis for computing loss. Then by trading off device geometry and process parameters it may be possible to achieve an optimum. Including gating loss, as is essential if frequency is to be further increased, adds yet another dimension. In part, this will depend on the specific on-resistance of the switch, which determines the device area necessary to achieve a given  $R_{DS-ON}$ . However, gate resistance which is affected by geometry also affects specific on-resistance.

Leaving switch considerations behind, integrating inductors, even at VHF, is no small matter. The  $\Phi_2$  depends upon inductors with quality factors in the range of 50, and above. This is perennially hard to do, with on-die  $Q$ s only approaching 20 at  $1GHz$  or better. However, if co-packaging is opened as an option, achievable operating frequencies may be high enough in light of an optimal integrated device. Among the benefits of co-packaging are small form factor and very low parasitic inductance, which can help in achieving some tuning points. For instance, where gate loss is a dominant factor, device area could be reduced for the same tuning point by adding shunt capacitance to the drain. While this is difficult in discrete implementations due to parasitic lead inductances, the much smaller dimensions associated with co-packaging may make it feasible.



*Appendix A*

# *SPICE DECKS AND COMPONENT VALUES*

---

This appendix includes spice files and/or values for the simulations used in each chapter as a demonstration and for the converter designs.

## A.1 Chapter 1 Data

### A.1.1 Fig. 1.4 data:

```
.LIB CLASSE.LIB"

.PARAM
+ PI=3.14159265
+ FS=50MEG      ;SWITCHING FREQUENCY
+ VCC=14.4;270  ;INPUT VOLTAGE
+ POUT=18;100
+ VGATE=5      ;DRIVER GATE VOLTAGE
** FS=50MEG    ;SWITCHING FREQUENCY
** VCC=270     ;INPUT VOLTAGE
** C1=1.9096P
** LRES=4.2778U
** CRES=3.7P
** RLOAD=358.3764
** VGATE=5    ;DRIVER GATE VOLTAGE
.PARAM:
**RLOAD={0.4916*VCC*VCC/POUT}
+RLOAD = 5.663
```

## *SPICE DECKS AND COMPONENT VALUES*

---

```
*+LRES={3.75*RLOAD/(2*PI*FS)}
+LRES = 66n;67.59n
+CRES={0.4166/(2*PI*FS*RLOAD)}
**C1={0.2150/(2*PI*FS*RLOAD)}
+C1 = 124p;128.6p;120.844p

*INPUT VOLTAGE SOURCE
VIN    IN 0  {VCC}

*CHOKE INDUCTOR
XL1 IN DUL1 LCHOKE
+ PARAMS:
+ L=1u;100u
+ QL=1500
+ FQ={FS}
+ RDC=.1M
+ IC=0

VDUL1 DUL1 DRAIN 0

*MOSFET

SMOS1  DRAIN SOURCE GATE 0 SIDEAL
.MODEL SIDEAL VSWITCH(ROFF=100MEG RON=1M  VOFF=2.4 VON=2.6)

VDMOS SOURCE 0 0

VGATE GATE 0 PULSE ( {VGATE} 0 0 1P 1P 10n {1/FS} )

XC1 DRAIN SOURCE CQS
+ PARAMS:
+ C={C1}
+ QC=10K
+ FQ={FS}
+ IC=0

XL2 DRAIN DUL2 LQS
+ PARAMS:
+ L={LRES}
```



```

+ QL=1500
+ FQ={FS}
+ IC=0

VDUL2 DUL2 X 0 ;DUMMY VOLTAGE SOURCE

XC2 X Y CQS
+ PARAMS:
+ C={CRES}
+ QC=3K
+ FQ={FS}
+ IC=0

R2 Y Z 1P

R3 Z DUR3 {RLOAD} ;LOAD RESISTANCE
VLOAD DUR3 0 0

.STEP PARAM RLOAD LIST 2 3 4 5.663 6 7 8 9 10
.TRAN 8P 7U 6.75u 8P UIC
.PROBE

```

## A.2 Chapter 2 Data

### A.2.1 Fig. 2.3 data:

```

*****Ideal phi inverter simulation*****
.PARAM
+ RLOAD = 10
+ PI = 3.14159
+ LSER = {(Q*Rload)/(2*pi*ft)}
+ Cser = {1/(2*pi*ft*Rload*Q)}
+ FT = 48.77MEG
+ Q = 20

V1 in 0 14.4

```

## *SPICE DECKS AND COMPONENT VALUES*

---

```
Vgate gate 0 pulse (0 5 0 1p 1p 6.25n 20n)
```

```
T1 in 0 drain 0 Td=5n Zo=20  
S1 drain 0 gate 0 sw  
L1 drain N1 {LSER}  
C1 N2 load {CSER}  
R1 load 0 {RLOAD}  
C2 drain 0 43.315
```

```
.model SW SW(Ron = 100m Roff=10MEG VT=2)  
.tran 0 10u 9.5u 10p UIC
```

```
****N.B. This simulation was done using LTSPICE. It  
****Will not work in PSPICE or SPICE as is. The switch  
****model must be updated appropriately
```

```
*****End Ideal phi inverter simulation*****
```

### **A.2.2 Fig. 2.4 data:**

```
*****Ideal phi detune inverter simulation*****
```

```
.PARAM  
+ RLOAD = 10  
+ PI = 3.14159  
+ LSER = {(Q*Rload)/(2*pi*ft)}  
+ Cser = {1/(2*pi*ft*Rload*Q)}  
+ FT = 48.77MEG  
+ Q = 20
```

```
V1 in 0 14.4  
Vgate gate 0 pulse (0 5 0 1p 1p 6.25n 20n)
```

```
T1 in 0 drain 0 Td=5n Zo=20  
S1 drain 0 gate 0 sw  
L1 drain N1 {LSER}  
C1 N2 load {CSER}  
R1 load 0 {RLOAD}  
C2 drain 0 43.315
```

```
.model SW SW(Ron = 100m Roff=10MEG VT=2)
.tran 0 10u 9.5u 10p UIC
```

```
****N.B. This simulation was done using LTSPICE. It
****Will not work in PSPICE or SPICE as is. The switch
****model must be updated appropriately
```

```
*****End Ideal phi detune inverter simulation*****
```

### A.2.3 Fig. 2.7 data:

```
***** Phi2 inverter waveforms simulation *****
```

```
.PARAM
+ LF =32.2n
+ CFEXTRA =280p
+ DUTY = .3
+ LDIV = 16.1n
+ FS = 50MEG
+ pi = 3.14159
+ CF = 34.5p
+ RLOAD = 7.91579
+ TON = {DUTY/FS -0.2p}
+ F2S = 100MEG
+ ZO = 49.207;10;49.207
+ L2F = {ZO/(2*PI*F2S)}
+ C2F = {1/(2*PI*F2S*ZO)}
```

```
Vin in 0 12
```

```
LF IN DRAININ1 {LF}
VDLF DRAININ1 DRAININ 0
L2F DRAININ V2F {L2F}
C2F V2F V2Fx {C2F}
VD2F V2Fx 0 0
```

```
VDMR DRAININ DRAIN 0
```

```
CF DRAIN S2 {CF}
VDCF S2 0 0
```

## *SPICE DECKS AND COMPONENT VALUES*

---

```
VDULOAD DRAIN DRAIN2 0

CFEXTRA DRAIN2 S2 {CFEXTRA}
LDIV DRAIN2 VRES {LDIV}
CBLOCK VRES LOADx 50n
VDLOADx LOADx LOAD 0
RLOAD LOAD 0 {RLOAD}

SWITCH DRAIN SOURCE GATE 0 SW1
.model SW1 VSWITCH(RON = 100m ROFF=1MEG VON = 2)
VDSOURCE SOURCE 0 0

VGATE GATE 0 PULSE(0 5 0 .1p .1p {TON} 20n)

.tran 0 5.4u 0.4u 50p uic
.probe
.end
***** Phi2 inverter waveforms simulation *****
```

### **A.2.4 Fig. 2.11 data:**

```
*****INVERTER DAMPING SIMULATION FILE*****
Vin in1 0 12
L1 in1 drain1 33.5n
L2 drain1 v2f1 22n
C1 v2f1 0 115p
S1 drain1 0 control 0 switch
C3 drain1 0 195p
L3 drain1 vres1 16.1n
C2 vres1 load1 50n
R1 load1 0 7.91579

.param
+duty = 0.38
+fs = 50MEG
+TON = {duty/fs-0.2p}
Vcontrol control 0 pulse (0 5 0 .1p .1p {TON} 20n)
.model switch vswitch(Ron = 100m Roff = 1MEG Von = 2)
```

```
V1 in 0 12 ac 1
LF in drain 32n
L2F drain V2F 22n
C2F V2F 0 115p
CF DRAIN 0 195p
LDIV DRAIN VRES 16.1n
CBLOCK VRES LOAD 50n
Rload LOAD 0 7.91579

Vtest 0 test pulse (0 5 0 1p 1p 10n 20n)
Rtest test 0 1
```

```
.ic V(drain) = 360.329m
.ic V(load) = -11.459
.ic V(V2f) = 1.4033
.ic V(Vres) = 467.699m
.ic I(LF) = 2.4658
.ic I(L2F) = 444.717m
.ic I(LDIV) = -1.44776
```

```
V2 inzi 0 0 ac 1
LFzi inzi drainzi 32n
L2Fzi drainzi V2Fzi 22n
C2Fzi V2Fzi 0 115p
CFzi DRAINzi 0 195p
LDIVzi DRAINzi VRESzi 16.1n
CBLOCKzi VRESzi LOADzi 50n
Rloadzi LOADzi 0 7.91579
```

```
.ic V(drainzi) = 360.329m
.ic V(loadzi) = -11.459
.ic V(V2fzi) = 1.4033
.ic V(Vreszi) = 467.699m
.ic I(LFzi) = 2.4658
.ic I(L2Fzi) = 444.717m
.ic I(LDIVzi) = -1.44776
```

## *SPICE DECKS AND COMPONENT VALUES*

---

```
V3 inzs 0 12 ac 1
LFzs inzs drainzs 32n
L2Fzs drainzs V2Fzs 22n
C2Fzs V2Fzs 0 115p
CFzs DRAINzs 0 195p
LDIVzs DRAINzs VRESzs 16.1n
CBLOCKzs VRESzs LOADzs 50n
Rloadzs LOADzs 0 7.91579
```

```
.ic V(drainzs) = 0
.ic V(loadzs) = 0
.ic V(V2fzs) = 0
.ic V(Vreszs) = 0
.ic I(LFzs) = 0
.ic I(L2Fzs) = 0
.ic I(LDIVzs) = 0
```

```
Vt vt 0 12
Rt vt 0 12
```

```
.tran 200p 5u 0u 200p UIC
*.ac dec 1000 10MEG 500MEG
.probe
.end
```

\*\*\*\*\*INVERTER DAMPING SIMULATION FILE\*\*\*\*\*

### **A.2.5 Fig. 2.13 data:**

```
*****Variable impedance transient and bode *****
.PARAM
+ LF =28.5n
*+ CFEXTRA =280p
*+ DUTY = .3
+ LDIV = 16.1n
+ FS = 50MEG
+ pi = 3.14159
+ CF = 34.5p
+ RLOAD = 7.91579
```

```

+ TON = {DUTY/FS -0.2p}
+ F2S = 100MEG
+ ZO = 49.207;10;49.207
+ L2F = {ZO/(2*PI*F2S)}
+ C2F = {1/(2*PI*F2S*ZO)}
+ CFEXTRA = {table(LF,28.5n,320p,32.2n,280p,35.5n,
+ 250p,38n,230p,41.2n,210p,
+ 44.7n,190p,53.5n,150p,63n,120p,66.7267n,110p,71n,
+ 100p,75.3n,90p,80n,80p,82.6n,70p,87n,60p,88n,50p)}
+ DUTY = {table(LF,28.5n,.28,32.2n,.30,35.5n,.32,38n,
+.32,41.2n,.32, 44.7n,.33,53.5n,.35,64n,.37,66.7267n,
+.38,71n,.38,75.3n,.40,80n,.40,82.6n,.42,87n,.44,88n,.46)}

```

Vin in 0 12

```

LF IN DRAININ1 {LF}
VDLF DRAININ1 DRAININ 0
L2F DRAININ V2F {L2F}
C2F V2F V2Fx {C2F}
VD2F V2Fx 0 0

```

VDMR DRAININ DRAIN 0

```

CF DRAIN S2 {CF}
VDCF S2 0 0
VDULOAD DRAIN DRAIN2 0

```

```

CFEXTRA DRAIN2 S2 {CFEXTRA}
LDIV DRAIN2 VRES {LDIV}
CBLOCK VRES LOADx 50n
VDLOADx LOADx LOAD 0
RLOAD LOAD 0 {RLOAD}

```

```

SWITCH DRAIN SOURCE GATE 0 SW1
.model SW1 VSWITCH(ROFF=1MEG VON = 2)
VDSOURCE SOURCE 0 0

```

VGATE GATE 0 PULSE(0 5 0 .1p .1p {TON} 20n)

IBODE 0 DRAIN AC 1

## *SPICE DECKS AND COMPONENT VALUES*

---

```
.step param LF list 28.5n 32.2n 35.5n 38n
+ 41.2n 44.7n 53.5n 63n 66.7267n 71n 75.3n 80n 82.6n
**.tran 0 5.4u 5.3u 50p uic
.ac dec 2000 10MEG 500MEG
.probe
.end
*****Variable impedance transient and bode *****
```

### **A.2.6 Fig. 2.14 data:**

```
***** Phi2 LF CF RETUNE *****
*** Note, the values in paratheses are changed in unison from
*** left to right to achieve the plots in the figure
```

```
.PARAM
+ LF =28.8n (28.8n 28.8n 71n 71n)
+ CFEXTRA =320p (320p 100p 100p 100p)
+ DUTY = .3 (0.3 0.3 0.3 0.38)
+ LDIV = 16.1n
+ FS = 50MEG
+ pi = 3.14159
+ CF = 34.5p
+ RLOAD = 7.91579
+ TON = {DUTY/FS -0.2p}
+ F2S = 100MEG
+ Z0 = 49.207;10;49.207
+ L2F = {Z0/(2*PI*F2S)}
+ C2F = {1/(2*PI*F2S*Z0)}
```

```
Vin in 0 12
```

```
LF IN DRAININ1 {LF}
VDLF DRAININ1 DRAININ 0
L2F DRAININ V2F {L2F}
C2F V2F V2Fx {C2F}
VD2F V2Fx 0 0
```



```

VDMR DRAININ DRAIN 0

CF DRAIN S2 {CF}
VDCF S2 0 0
VDULOAD DRAIN DRAIN2 0

CFEXTRA DRAIN2 S2 {CFEXTRA}
LDIV DRAIN2 VRES {LDIV}
CBLOCK VRES LOADx 50n
VDLOADx LOADx LOAD 0
RLOAD LOAD 0 {RLOAD}

SWITCH DRAIN SOURCE GATE 0 SW1
.model SW1 VSWITCH(ROFF=1MEG VON = 2)
VDSOURCE SOURCE 0 0

VGATE GATE 0 PULSE(0 5 0 .1p .1p {TON} 20n)

IBODE 0 DRAIN AC 1

.tran 0 5.4u 5.3u 50p uic
.probe
.end
***** Phi2 LF CF RETUNE *****

```

### A.2.7 Fig. 2.15 data:

```

*****PHI2 VARIABLE ZO *****
***** 10 Dec 2006 *****

*****
**** OPTIONS FOR BETTER CONVERGENCE
*****
.OPTIONS ABSTOL=1nA
+         GMIN=1p
+         ITL1=6000
+         ITL2=4000
+         ITL4=5000

```

## SPICE DECKS AND COMPONENT VALUES

---

```
+          RELTOL=0.001
+          VNTOL=0.001mV
.OPTION STEPGMIN

***** Libraries
.LIB "CLASSE.LIB"
***** Parameters
.PARAM
+ PI = 3.14159
+ FS = 50MEG
+ QI = 80
+ QC = 5000
+ VIN = 12
+ VOUT = 33
+ DUTY = 0.3
+ TON = {DUTY/FS - 2p}
+ CF = 155p
+ CFEXTRA = 215.9p
+ LDIV = 14.1n
+ RLOAD = 7.91579
+ CS = 50n
+ LEXTRA = 1n
+ F2S = 100MEG
+ L2F = {Z0/(2*PI*F2S)}
+ C2F = {1/(2*PI*F2S*Z0)}

+ Z0 = {table(CFEXTRA,155.17p,160,166.12p,80,
+ 179.93p,49.137,202.7p,30,
+ 231.96p,20,247.815p,16.94,272.5p,13.68,
+ 319.73p,10,495.41p,5,1022.93p,2)}

+ LF = {table(CFEXTRA,155.17p,29.965n,166.12p,
+ 27.941n,179.93p,25.75n,202.7p,22.8n,
+ 231.96p,19.875n,247.815p,18.5832n,272.5p,
+ 16.875n,319.73p,
+ 14.352n,495.41p,9.2228n,1022.93p,4.449n)}

VIN IN 0 {VIN}

XLF IN DRAINX LCHOKE
+ PARAMS:
```

```
+ L = {LF}
+ QL = {QI}
+ FQ = {FS}
+ IC = 0
+ RDC = 10m
```

```
XL2F DRAINX V2FX LQS
```

```
+ PARAMS:
+ L = {L2F}
+ QL = {QI}
+ FQ = {2*FS}
+ IC = 0
```

```
VD2F V2FX V2F 0
```

```
XC2F V2F 0 CQS
```

```
+ PARAMS:
+ C = {C2F}
+ QC = {QC}
+ FQ = {2*FS}
+ IC = 0
```

```
VDMR DRAINX DRAIN 0
```

```
SWITCH DRAIN SOURCE GATE 0 SW
```

```
.model SW VSWITCH (Ron = 0.4 Roff=10MEG VON = 0.2)
```

```
RCOUT DRAIN vcout 0.8
```

```
COUT vcout 0 {CF}
```

```
*Rb Vn101 0 1
```

```
*Rc Igcn1 0 1
```

```
*Rd Isw 0 1
```

```
VDSOURCE SOURCE 0 0
```

```
IBODE 0 DRAIN AC 1
```

```
VDLOAD DRAIN DRAINy 0
```

```
XCEXTRA DRAINy SOURCE CQS
```

## SPICE DECKS AND COMPONENT VALUES

---

```
+ PARAMS:
+ C = {CFEXTRA}
+ QC = {QC}
+ FQ = {FS}
+ IC = 0

XLDIV DRAINy LOAD LQS
+ PARAMS:
+ L = {LDIV}
+ QL = {QI}
+ FQ = {FS}
+ IC = 0

CS LOAD LOAD1 {CS}
RLOAD LOAD2 0 {RLOAD}
VDLOAD1 LOAD1 LOAD2 0

***** GATE DRIVE

VDRIVE GATE 0 PULSE (0 10 0 1p 1p {TON} {1/FS})

*****
***** SIMULATION CONTROL*****
.STEP PARAM CFEXTRA LIST 202.7p 231.96p 247.815p
+ 272.5p 319.73p 495.41p
.TRAN 200p 2U 0U 101p UIC
.ac dec 3000 10MEG 500MEG

*****
*****
.PROBE
.END
*****PHI2 VARIABLE ZO *****
```

### A.2.8 Fig. 2.17 data:

```
***** Vary 1:3, constant power*****
```

```

.PARAM
+ fscale = 1
+ LF =94n
+ FS = {50MEG*Fscale}
+ pi = 3.14159
+ CF = 34.5p
+ RLOAD = 7.91579
+ TON = {DUTY/FS -0.2p}
+ F2S = 100MEG
+ ZO = 49.207;10;49.207
+ L2F = {ZO/(2*PI*F2S)}
+ C2F = {1/(2*PI*F2S*ZO)}

+ LDIV = {table(LF,28.5n,16.1n,48.1n,18.1n,94n,
+ 20.1n,131.3n,21.1n,168n,22.5n,480n,23.1n)}
+ CFEXTRA = {table(LF,28.5n,320p,48.1n,193p,
+ 94n,101.5p,131.3n,73p,168n,59.5p,480n,29p)}
+ DUTY = {table(LF,28.5n,.28,48.1n,.32,
+ 94n,.37,131.3n,.4,168n,.42,480n,0.46)}

Vin in 0 12

LF IN DRAININ1 {LF/fscale}
VDLF DRAININ1 DRAININ 0
L2F DRAININ V2F {L2F/fscale}
C2F V2F V2Fx {C2F/fscale}
VD2F V2Fx 0 0

VDMR DRAININ DRAIN 0

CF DRAIN S2 {CF/fscale}
VDCF S2 0 0
VDULOAD DRAIN DRAIN2 0

CFEXTRA DRAIN2 S2 {CFEXTRA/fscale}
LDIV DRAIN2 VRES {LDIV/fscale}
CBLOCK VRES LOADx 50n
VDLOADx LOADx LOAD 0
RLOAD LOAD 0 {RLOAD}

SWITCH DRAIN SOURCE GATE 0 SW1

```

## *SPICE DECKS AND COMPONENT VALUES*

---

```
.model SW1 VSWITCH(RON = 100m ROFF=1MEG VON = 2)
VDSOURCE SOURCE 0 0

VGATE GATE 0 PULSE(0 5 0 .1p .1p {TON} {1/fs})

IBODE 0 DRAIN AC 1

.probe
.tran 0 15u 14.9u 50p uic
.step param LF list 28.5n 48.1n 94n 131.3n 168n 480n
.end
```

This deck varies the ratio of fundamental and third harmonic while holding the power constant. This shows the effects of making the waveforms less peaky in terms of rms current and loss...at a given 2nd harmonic tank characteristic impedance. Once a desired peakiness is reached, overall  $Z_o$  as described in chapter 2 can be changed. Losses were computed with a MATLAB script based on assumed inductor  $Q = 80$ , and switch  $R_{dson} = 400m\Omega$  and  $R_{oss} = 800m\Omega$ . Dc current was subtracted from LF when computing that loss as it is significant. The assumed dc resistance was  $10m\Omega$

\*\*\*\*\* Vary 1:3, constant power\*\*\*\*\*

### **A.2.9 Fig. 2.19 data:**

\*\*\*\*\*Variable Transient Response\*\*\*\*\*

```
.PARAM
+ LF =480n
+ FS = 50MEG
+ pi = 3.14159
+ CF = 34.5p
+ RLOAD = 7.91579
+ TON = {DUTY/FS -0.2p}
+ F2S = 100MEG
+ ZO = 49.207;10;49.207
+ L2F = {ZO/(2*PI*F2S)}
```

```

+ C2F = {1/(2*PI*F2S*Z0)}

+ LDIV = {table(LF,28.5n,16.1n,48.1n,18.1n,
+ 94n,20.1n,131.3n,21.1n,168n,22.5n)}
+ CFEXTRA = {table(LF,28.5n,320p,48.1n,193p,
+ 94n,101.5p,131.3n,73p,168n,59.5p)}
+ DUTY = {table(LF,28.5n,.28,48.1n,.32,
+ 94n,.37,131.3n,.4,168n,.42)}

Vin in 0 12

LF IN DRAININ1 {LF}
VDLF DRAININ1 DRAININ 0
L2F DRAININ V2F {L2F}
C2F V2F V2Fx {C2F}
VD2F V2Fx 0 0

VDMR DRAININ DRAIN 0

CF DRAIN S2 {CF}
VDCF S2 0 0
VDULOAD DRAIN DRAIN2 0

CFEXTRA DRAIN2 S2 {CFEXTRA}
LDIV DRAIN2 VRES {LDIV}
CBLOCK VRES LOADx 50n
VDLOADx LOADx LOAD 0
RLOAD LOAD 0 {RLOAD}

SWITCH DRAIN SOURCE GATE 0 SW1
.model SW1 VSWITCH(ROFF=1MEG VON = 2)
VDSOURCE SOURCE 0 0

VGATE GATE 0 PULSE(0 5 0 .1p .1p {TON} 20n)

IBODE 0 DRAIN AC 1

.probe

.tran 0 400n 0u 50p uic

```

## *SPICE DECKS AND COMPONENT VALUES*

---

```
.step param LF list 48.1n 168n
.end
***This deck runs two steps demonstrating different
***transient response for different peakiness but
***identical output power
*****Variable Transient Response*****
```

### A.3 Chapter 3 Data

#### A.3.1 Fig. 3.4 data:

```
*****IDEAL RECTIFIER SIMULATION*****

.LIB RECT21.LIB

.PARAM
+ VDC = 12
+ FS = 50MEG
+ PI = 3.14159
+ VF = {VDC}
+ Zo = 23.99427;10;17.204
+ LREC = 59.717n
+ CREC = 98.51p
VIN IN 0 SIN({VDC} {VF} 50MEG)

VOUT OUT 0 33

L1 IN VREC {LREC}
C1 VREC 0 {CREC};{85P+100P}
.MODEL DIODE D(CJO = 267.77p M=0.42044 VJ=0.3654 RS=0.3)

SDIODE VREC OUT VREC OUT SWITCH
.MODEL SWITCH VSWITCH(Ron = 1u Roff = 100MEG Von = 10m Voff = 0)

.TRAN 200P 5U 4.9U 200P UIC
```



```
.PROBE
.END
*****IDEAL RECTIFIER SIMULATION*****
```

### A.3.2 Fig. 3.5 data:

```
*****RECTIFIER AC-DC POWER SIM*****
```

```
.PARAM
+ VDC = 12
+ FS = 50MEG
+ PI = 3.14159
+ VF = {VDC}
+ Zo = 23.99427;10;17.204 (diode switch 34.52,23.99427)
+ LREC = 59.717n ;54.76n;28N
+ FCENTER = 67.33MEG
*+ LREC = {Zo/(2*pi*FCENTER)}
*+ CREC = {1/(Zo*2*pi*FCENTER)}
+ CREC = 98.51p

VIN IN 0 SIN({VDC} {VF} 50MEG)
VOUT OUT 0 33

L1 IN VREC {LREC}
C1 VREC 0 {CREC};{85P+100P}

SDIODE VREC OUT VREC OUT SWITCH
.MODEL SWITCH VSWITCH(Ron = 1u Roff = 100MEG Von = 10m Voff = 0)

.STEP PARAM VDC LIST 8 10 12 14 16 18 20 22 24 26 28 30 32
.TRAN 200P 5U 4.9U 200P UIC
.PROBE
.END
```

```
*****RECTIFIER AC-DC POWER SIM*****
```

## *SPICE DECKS AND COMPONENT VALUES*

---

### **A.3.3 Fig. 3.6 data:**

\*\*\*\*\*RECT FC and ZO SWEEP FOR TUNING\*\*\*\*\*

```
.PARAM
+ VDC = 14
+ FS = 50MEG
+ PI = 3.14159
+ VF = {VDC}
+ Zo = 10;17.204 (diode switch 34.52,23.99427)
+ FCENTER = 72MEG
+ LREC = {Zo/(2*pi*FCENTER)}
+ CREC = {1/(Zo*2*pi*FCENTER)}

VIN IN 0 SIN({VDC} {VF} 50MEG)
*VIN IN 0 SIN(12 {VF} 50MEG)
VOUT OUT 0 33

L1 IN VREC {LREC}
C1 VREC 0 {CREC};{85P+100P}
*D1 VREC OUT DIODE
.MODEL DIODE D(CJO = 267.77p M=0.42044 VJ=0.3654 RS=0.3)

SDIODE VREC OUT VREC OUT SWITCH
.MODEL SWITCH VSWITCH(Ron = 1u Roff = 100MEG Von = 10m Voff = 0)

*XDREC VREC OUT DIODENL
**+ PARAMS:
**+ LDS=.000000001p ;SERIES INDUCTANCE
**+ VDON=0.55 ;DIODE FORWARD DROP
**+ RDS=.3;0.1254 ;SERIES RESISTANCE
**+ CJO=267.77p;{diodecjo}
**+ VJ=0.36521670770030;0.3241
**+ M=0.42044726053532 ;0.4597
**+ RC=.24;.8 ;RESIST. IN SERIES WITH NON-LIN CAPACITOR
**+ FS={FS}
```

```
.STEP PARAM ZO LIST 10 15 20 25
*.STEP PARAM FCENTER LIST 65MEG 70MEG 71MEG
+ 72MEG 73MEG 74MEG 75MEG 80MEG
.TRAN 200P 5U 4.9U 200P UIC
.PROBE
.END
```

```
* First pick a center frequency then sweep Zo to change power
*****RECT FC and ZO SWEEP FOR TUNING*****
```

## A.4 Chapter 4 Data

### A.4.1 ST Converter Final Spice Deck

```
*****
***
*** STdcdc_plus_gatedr.cir
***
*** This simulation includes a basic gate driver along
*** With the dc-dc converter
***
*** 20Jan06
***
***
*****

*****
*** LIST OF LIBRARIES ***
*****

.LIB CLASSE.LIB
.LIB "MOSNL1.LIB"
.LIB "RECT21.LIB"

*****
**** OPTIONS FOR BETTER CONVERGENCE ***
*****
.OPTIONS ABSTOL=1nA
```

## SPICE DECKS AND COMPONENT VALUES

---

```
+          GMIN=1p
+          ITL1=6000
+          ITL2=4000
+          ITL4=5000
+          RELTOL=0.001
+          VNTOL=0.001mV
.OPTION STEPGMIN
```

```
*****
*** OPTIONS TO KEEP A SMALL OUTPUT FILE ***
*****
```

```
.OPTIONS
+ NOPAGE
+ NOBIAS
+ NOECHO
+ NOMOD
+ NUMDGT=8
.WIDTH OUT=132 ;TO PRINT MORE COLUMNS
```

```
*****
*** SPECIAL PARAMETERS AND CONSTANTS ***
*****
```

```
.PARAM
+ PI=3.14159
```

```
*****
* CIRCUIT PARAMETERS *
*****
```

```
*---DESIGN PARAMETERS
```

```
.PARAM:
```

```
+FS=75MEG          ;SWITCHING FREQUENCY
+VIN=14            ;INPUT VOLTAGE
+VOUT=33           ;OUTPUT VOLTAGE
+DUTY=.4;.3       ;DUTY CYCLE
+QC=2k            ;Q CAPACITORS
+QI=100           ;Q INDUCTORS
+TRMULT = 200     ;GATE DRIVE RISE-TIME MULTIPLIER (1/(TRMULT*FS))
```

\*---L2F AND C2F PARAMETRIZED BY Z0 AND F2S  
 .PARAM:

+ F2S = 150MEG  
 + Z0 = 20;10

\*+ L2F = {Z0/(2\*PI\*F2S)}  
 \*+ C2F = {1/(2\*PI\*F2S\*Z0)}

+ L2F = 22n  
 + C2F = 51p

\*---COUT, CEXTRA, LF, LREC, CREC

+ COUTNOM = 50P  
 + CEXTRA = 1p  
 + LF = 130n;169n  
 + LREC = 35.5n;37n;28n;38n  
 + CREC = 81p;85p  
 + RGATE = 195M  
 + CGATE = 106P  
 + LGATE = 21N  
 + CGATESW = 24P  
 + RCGATESW = 3  
 + RGATESW = 0.6  
 + VGBIAS = 5  
 + CJO = 185.52p  
 + LRECP = 2n  
 + LCRECP = 1n  
 + DIODECJO = 3.072E-10

\*\*\*\*\*  
 \*\*\*CIRCUIT DESCRIPTION \*\*\*  
 \*\*\*\*\*

\*---DC source

## *SPICE DECKS AND COMPONENT VALUES*

---

```
VIN IN 0 {VIN}
Rbig IN 0 10g

*---LUMPED MR NETWORK

XLF IN DRAIN LCHOKE          ;MULTIRESONANT ELEMENT
+ PARAMS:
+ L={LF}
+ QL = 80
*+ QL={QI}
+ FQ={FS}
+ IC=0
+ RDC=10m
*+RDC=1.45

XL2F DRAIN V2FX LQS          ;MULTIRESONANT ELEMENT
+ PARAMS:
+ L={L2F}
+ QL=40
+ FQ={FS}
+ IC=0

VD2F V2FX V2F 0              ;DUMMY TO MEASURE CURRENT LMR

XC2F V2F 0 CQS                ;MULTIRESONANT ELEMENT
+ PARAMS:
+ C={C2F}
+ QC={QC}
+ FQ={FS}
+ IC=0

*---NON LINEAR MOSFET MODEL
XSWITCH GATEX DRAIN SOURCE MOSFETNLC
*XSWITCH GATEX DRAIN SOURCE MOSFETNLCRES
+ PARAMS:
+ RDSON = 0.373
+ RG = {RGATE}
+ CGS = {CGATE}
+ RCOUT = 0.655
+ RSHUNT = 12MEG
+ CJO = {CJO}
```

```
+ VJ = 0.168
+ M = 0.2205
+ LDRAIN = 400p
+ LSOURCE = 200p
+ LGATE = 400p
+ CRSS = 10p
VDMOS SOURCE 0 0
VDGATE GATE GATEX 0
```

```
XCEXTRA DRAIN SOURCEX CQS
+ PARAMS:
+ C={CEXTRA}
+ QC={QC}
+ FQ={FS}
+ IC=0
```

```
XLCEXTRAP SOURCEX SOURCE LQS
+ PARAMS:
+ L=1.1n
+ QL=80
+ FQ={FS}
+ IC=0
```

```
ibode 0 drain ac 1
```

```
***** RECTIFIER *****
VDREC DRAIN DRAINX 0
```

```
XLREC DRAINX VREC LQS ; RECTIFIER INDUCTOR
+ PARAMS:
+ L={LREC}
+ QL = 80
+ FQ={FS}
+ IC=0
```

```
XCREC VRECC 0 CQS ; RECTIFIER CAPACITOR
+ PARAMS:
+ C={CREC}
+ QC={QC}
+ FQ={FS}
+ IC=0
```

## *SPICE DECKS AND COMPONENT VALUES*

---

```
XLCRECP VREC VRECC LQS ; PARASITIC INDUCTOR FOR SHUNT CAPACITOR
+ PARAMS:
+ L={LCRECP}
+ QL={QI}
+ FQ={FS}
+ IC=0
```

```
VDIODE VREC VREC1 0
XDREC VREC1 OUT DIODENL
+ PARAMS:
+ LDS={LRECP} ;SERIES INDUCTANCE
+ VDON=0.55 ;DIODE FORWARD DROP
+ RDS=.3;0.1254 ;SERIES RESISTANCE
+ CJO=267.77p;{diodecjo}
+ VJ=0.36521670770030;0.3241
+ M=0.42044726053532 ;0.4597
+ RC=.24;.8 ;RESIST. IN SERIES WITH NON-LIN CAPACITOR
+ FS={FS}
```

```
VLOAD OUT 0 {VOUT}
```

```
***** GATE DRIVER *****
```

```
.PARAM
+ LGATEDRIVE = 42n
+ GATEBIAS = 0
+ CBLOCK = 0.1u
```

```
VBIAS BIAS 0 {GATEBIAS}
RBIAS BIAS GATE 620
```

```
VDRIVE VDRIVE 0 SIN (0 30 {FS})
RDRIVE VDRIVE PREGATE 50
CBLCOCK PREGATE GATE .1u
```

```
.PARAM
+ TR = {1/(20*FS)}
+ PWIDTH = {DUTY/FS - 2*TR}
```

```
*---PARAMETER EXTRACTION
VPLF PLF 0 {LF}
```



```
VPL2F    PL2F    0  {L2F}
VPC2F    PC2F    0  {C2F}
VPLREC   PLREC   0  {LREC}
VPCREC   PCREC   0  {CREC}
VPLGATE  PLGATE  0  {LGATE}
VPRGATE  PRGATE  0  {RGATE}
VPCGATE  PCGATE  0  {CGATE}
```

```
*****
*** SIMULATION CONTROL ***
*****
.TRAN 10p 4.8U 4.7U 50p UIC
* .ac dec 2000 10MEg 500MEG
*.STEP PARAM VIN 8 18 1
.STEP PARAM VOUT 22 33 1
.PROBE
.END
```

## A.4.2 50MHz Converter Final Spice Deck

```
*****
*** LIST OF LIBRARIES ***
*****

.LIB CLASSE.LIB
.LIB RECT21.LIB
.LIB "MOSNL3_nat2.LIB"

*****
**** OPTIONS FOR BETTER CONVERGENCE
*****
.OPTIONS ABSTOL=1nA
+         GMIN=1p
+         ITL1=6000
+         ITL2=4000
+         ITL4=5000
```

## SPICE DECKS AND COMPONENT VALUES

---

```
+          RELTOL=0.001
+          VNTOL=0.001mV
.OPTION STEPGMIN
```

```
*****
*** OPTIONS TO KEEP A SMALL OUTPUT FILE ***
*****
```

```
.OPTIONS
+ NOPAGE
+ NOBIAS
+ NOECHO
+ NOMOD
+ NUMDGT=8
.WIDTH OUT=132 ;TO PRINT MORE COLUMNS
```

```
*****
*** SPECIAL PARAMETERS AND CONSTANTS ***
*****
```

```
.PARAM
+ PI=3.14159      ;GUESS WHAT
```

```
*****
* CIRCUIT PARAMETERS      *
*****
```

```
*---DESIGN PARAMETERS
```

```
.PARAM:
```

```
+FS=50MEG          ;SWITCHING FREQUENCY
+VIN=14            ;INPUT VOLTAGE
+VOUT=32           ;OUTPUT VOLTAGE
+DUTY=.4           ;DUTY CYCLE
+QC=5k             ;Q CAPACITORS
+QI=80             ;Q INDUCTORS
+TRMULT = 200      ;GATE DRIVE RISE-TIME MULTIPLIER (1/(TRMULT*FS))
```

```
*---L2F AND C2F PARAMETRIZED BY ZO AND F2S
```

```
.PARAM:
```

```

+ F2S = 100MEG
+ Z0 = 16.9646

*+ L2F = {Z0/(2*PI*F2S)}
*+ C2F = {1/(2*PI*F2S*Z0)}

+ L2F = 22n
+ C2F = 115p

*---COUT, CEXTRA, LF, LREC, CREC

+ COUTNOM = 50P
+ CEXTRA = 56p
+ LF = 22n
+ LREC = 63n;56n;58n
+ CREC = 47p;53p
+ RGATE = 800M
+ CGATE = 276P
+ LGATE = 1N
+ CGATESW = 24P
+ RCGATESW = 3
+ RGATESW = 0.6
+ VGBIAS = 0
+ LRECP = 1n
+ LCRECP = 1n

*****
***CIRCUIT DESCRIPTION ***
*****

*---DC source
VIN IN 0 {VIN}
Rbig IN 0 10g

*---LUMPED MR NETWORK

XLF IN DRAIN LCHOKE ;MULTIRESONANT ELEMENT
+ PARAMS:

```

## *SPICE DECKS AND COMPONENT VALUES*

---

```
+ L={LF}
+ QL = 80
+ FQ={FS}
+ IC=0
+ RDC=10m
```

```
XL2F DRAIN V2FX LQS ;MULTIRESONANT ELEMENT
+ PARAMS:
+ L={L2F}
+ QL=80
+ FQ={2*FS}
+ IC=0
```

```
VD2F V2FX V2F 0 ;DUMMY TO MEASURE CURRENT L2F
```

```
XC2F V2F 0 CQS ;MULTIRESONANT ELEMENT
+ PARAMS:
+ C={C2F}
+ QC={QC}
+ FQ={FS}
+ IC=0
```

```
*---NON LINEAR MOSFET MODEL
XSWITCH GATEX DRAIN SOURCE MOSFETNLC
+ PARAMS:
+ LDRAIN = 400p
+ LSOURCE = 100p
+ LGATE = 400p
+ KRES = 2
+ KROSS = 2
```

```
VDMOS SOURCE 0 0
VDGATE GATE GATEX 0
```

```
XCEXTRA DRAIN SOURCEX CQS
+ PARAMS:
+ C={CEXTRA}
+ QC={QC}
```

```
+ FQ={FS}
+ IC=0
```

```
XLCEXTRAP SOURCEX SOURCE LQS
+ PARAMS:
+ L=1n
+ QL={QI}
+ FQ={FS}
+ IC=0
```

```
ibode 0 drain ac 1
```

```
***** RECTIFIER *****
VDREC DRAIN DRAINX 0
```

```
XLREC DRAINX VREC LQS ; RECTIFIER INDUCTOR
+ PARAMS:
+ L={LREC}
+ QL = {QI};109
+ FQ={FS}
+ IC=0
```

```
XCREC VRECC 0 CQS ; RECTIFIER CAPACITOR
+ PARAMS:
+ C={CREC}
+ QC={QC}
+ FQ={FS}
+ IC=0
```

```
VVREC VREC VRECD 0 ;current dummy
XLCRECP VRECD VRECC LQS ; PARASITIC INDUCTOR FOR SHUNT CAPACITOR
+ PARAMS:
+ L={LCRECP}
+ QL={QI}
+ FQ={FS}
+ IC=0
```

```
VDIODE VREC VREC1 0
XDREC VREC1 OUT DIODENL
```

## *SPICE DECKS AND COMPONENT VALUES*

---

```
+ PARAMS:
+ LDS={LRECP} ;SERIES INDUCTANCE
+ VDON=0.55 ;DIODE FORWARD DROP
+ RDS=.3;0.1254 ;SERIES RESISTANCE
+ CJO=267.77p;{diodecjo}
+ VJ=0.36521670770030;0.3241
+ M=0.42044726053532 ;0.4597
+ RC=.3;.8 ;RESIST. IN SERIES WITH NON-LIN CAPACITOR
+ FS={FS}
```

```
VLOAD OUT 0 {VOUT}
```

```
***** GATE DRIVER *****
```

```
.PARAM
+ LGATEDRIVE = 42n
+ GATEBIAS = 0
+ CBLOCK = 0.1u

VBIAS BIAS 0 {GATEBIAS}
RBIAS BIAS GATE 620
RDRIVE VDRIVE PREGATE 10;0.5
CBLCOCK PREGATE GATE .1u
```

```
VDRIVE VDRIVE 0 SIN (-1 25 14 {FS})
```

```
.PARAM
+ TR = {1/(20*FS)}
+ PWIDTH = {DUTY/FS - 2*TR}
```

```
*---PARAMETER EXTRACTION
VPLF PLF 0 {LF}
VPL2F PL2F 0 {L2F}
VPC2F PC2F 0 {C2F}
```

```
VPLREC    PLREC  0   {LREC}
VPCREC    PCREC  0   {CREC}
VPLGATE   PLGATE 0   {LGATE}
VPRGATE   PRGATE 0   {RGATE}
VPCGATE   PCGATE 0   {CGATE}
```

```
*****
*** SIMULATION CONTROL ***
*****
.TRAN 200p 5U 4.8U 200p UIC
.STEP PARAM VIN 8 18 1
*.STEP PARAM VOUT 22 33 1
*.ac dec 2000 1MEG 15000MEG
.PROBE
.END
```

### A.4.3 SPICE Model Libraries

NOTE: THE DEFAULT MODEL PARAMETERS ARE NOT CORRECT. THEY ARE ONLY PLACEHOLDERS. WHEN THE MODEL IS PAIRED WITH THE APPROPRIATE SPICE DECK, THE PARAMETERS WILL BE POPULATED CORRECTLY.

```
*****RECT21.LIB*****
```

```
.SUBCKT DIODENL A K
+ PARAMS:
+ LDS=3N ;SERIES INDUCTANCE
+ VDON=0.8 ;DIODE FORWARD DROP
+ RDS=0.12 ;SERIES RESISTANCE
+ CJO=550P
+ VJ=1.80372824438359
+ M=0.44880310087245
+ RC=.05 ;RESIST. IN SERIES WITH NON-LIN CAPACITOR
+ FS=30MEG
```

## *SPICE DECKS AND COMPONENT VALUES*

---

```
*PARASITIC LEAD INDUCTANCE
LDS  A  101  {LDS}  IC=0
```

```
*IDEAL DIODE MODEL
DIDEAL 101 102 IDEAL
.MODEL IDEAL D(N=0.001)
```

```
*FORWARD VOLTAGE DROP MODEL
VDON  102 103  {VDON}
RDS   103 K    {RDS}
```

```
*NONLINEAR CAPACITANCE EVALUATED AS A CONTROLLED CURRENT
*SOURCE
```

```
GCNL  K 104 VALUE={IF((V(K)-V(104))<0,CJO*V(201)*
+ (1/LDER),V(201)*(1/LDER)*(CJO/((1+((V(K)-V(104))/VJ)**M)))}
RC    101 104 {RC}
```

```
****SUBCIRCUIT TO EVALUATE THE DERIVATIVE***
```

```
*PARAMETERS AND DEFINITION FOR THIS SUBCIRCUIT
```

```
.PARAM:
+ LDER=1U      ;INDUCT FOR THE DERIVATIVE SUBCIRCUIT
+ PI=3.14159265
```

```
*FUNC. FOR R OF THE DERIVATIVE SUBCIRCUIT
```

```
.FUNC RDER(LDER,FS) {3000*2*PI*FS*LDER}
GY 0 201 VALUE={V(K)-V(104)}
L1 201 0 {LDER}
R1 201 0 {RDER(LDER,FS)}
```

```
.ENDS DIODENL      ; CSD10060
```

```
*****RECT21.LIB*****
```

```
*****MOSNL3_nat2.LIB*****
```



```
.SUBCKT MOSFETNLC GATE DRAIN SOURCE
+ PARAMS:
+ KRES=1
+ KROSS=1
+ RDSON=0.2
+ RG=1.7
+ CGS=276P
+ RCOUT=0.6
+ RSHUNT=12MEG
+ CJO=425.2P
+ VJ=0.17668879186097
+ M=0.25261528053076
+ LDRAIN = 1p
+ LSOURCE = 1p
+ LGATE = 1p
+ CRSS = 30p
```

```
LDRAIN DRAIN DRAINL {LDRAIN}
RSHUNT DRAINL SOURCEL {RSHUNT}
LSOURCE SOURCEL SOURCE {LSOURCE}
```

```
.PARAM:
+ R1 = 25.917
+ VRD1 = 1
+ R2 = 0.657255
+ VRD2 = 2
+ R3 = 1.5336
+ VRD3 = 3
+ R4 = 2.4671
+ VRD4 = 4
+ R5 = 3.463
+ VRD5 = 5
+ R6 = 4.6861
+ VRD6 = 6
+ R7 = 3.7909
+ VRD7 = 9
+ R8 = 2.1371
+ VRD8 = 18
```

## SPICE DECKS AND COMPONENT VALUES

---

\*\*\*\*\*

```
SW1      DRAINL  SOURCEL  GMAIN  SOURCE  SRD1
.MODEL SRD1 VSWITCH (RON={R1*Kres} ROFF=1MEG VON={VRD1} VOFF={VRD1-1})
```

```
SW2      DRAINL  SOURCEL  GMAIN  SOURCE  SRD2
.MODEL SRD2 VSWITCH (RON={R2*Kres} ROFF=1MEG VON={VRD2} VOFF={VRD1})
```

```
SW3      DRAINL  SOURCEL  GMAIN  SOURCE  SRD3
.MODEL SRD3 VSWITCH (RON={R3*Kres} ROFF=1MEG VON={VRD3} VOFF={VRD2})
```

```
SW4      DRAINL  SOURCEL  GMAIN  SOURCE  SRD4
.MODEL SRD4 VSWITCH (RON={R4*Kres} ROFF=1MEG VON={VRD4} VOFF={VRD3})
```

```
SW5      DRAINL  SOURCEL  GMAIN  SOURCE  SRD5
.MODEL SRD5 VSWITCH (RON={R5*Kres} ROFF=1MEG VON={VRD5} VOFF={VRD4})
```

```
SW6      DRAINL  SOURCEL  GMAIN  SOURCE  SRD6
.MODEL SRD6 VSWITCH (RON={R6*Kres} ROFF=1MEG VON={VRD6} VOFF={VRD5})
```

```
SW7      DRAINL  SOURCEL  GMAIN  SOURCE  SRD7
.MODEL SRD7 VSWITCH (RON={R7*Kres} ROFF=1MEG VON={VRD7} VOFF={VRD6})
```

```
SW8      DRAINL  SOURCEL  GMAIN  SOURCE  SRD8
.MODEL SRD8 VSWITCH (RON={R8*Kres} ROFF=1MEG VON={VRD8} VOFF={VRD7})
```

\*\*\*\*\*

```
*NONLINEAR CAPACITANCE EVALUATED AS A CONTROLLED CURRENT SOURCE
GCNL  N101 DRAINL VALUE={IF((V(DRAINL)-V(N101))<0,CJO*V(201)*(1/LDER)
+,V(201)*(1/LDER)*(CJO/((1+((V(DRAINL)-V(N101))/VJ)**M)))}
```

```
DIDEAL SOURCEL DRAINL DIODE
*.model DIODE D(N=.0001)
.model DIODE D(N=0.5 RS=0.2 TT=5n)
```

```
RCOUT N101  SOURCEL {RCOUT*KROSS}
```

```

LGATE GATE GATEL {LGATE} ;RSER=10m RPAR=1MEG
RG GATEL GMAIN {RG}
CGS GMAIN SOURCEL {CGS} ;RSER=10m RPAR=1MEG
*RRSS DRAINL DRAINR 10
CRSS DRAINL GMAIN {CRSS} ;RSER=30 RPAR=1MEG

```

\*\*\*\*SUBCIRCUIT TO EVALUATE THE DERIVATIVE\*\*\*

\*PARAMETERS AND DEFINITION FOR THIS SUBCIRCUIT

.PARAM:

```

+ LDER=.01U ;INDUCT FOR THE DERIVATIVE SUBCIRCUIT
+ PI=3.1416

```

\*FUNC. FOR R OF THE DERIVATIVE SUBCIRCUIT

.FUNC RDER(LDER,FS) {1000\*2\*PI\*FS\*LDER}

GY 0 201 VALUE={V(N101)-V(DRAINL)}

L1 201 0 {LDER}

R1 201 0 {RDER(LDER,FS)}

.ENDS MOSFETNLC

\*\*\*\*\*MOSNL3\_nat2.LIB\*\*\*\*\*

\*\*\*\*\*CLASSE.LIB\*\*\*\*\*

.SUBCKT LQS LSI LSO

+ PARAMS:

+ L=1U

+ QL=300

+ FQ=60MEG

+ IC=0

.PARAM: PI=3.1416

.FUNC ESR(L,QL,FQ) {2\*PI\*FQ\*L/QL}

## *SPICE DECKS AND COMPONENT VALUES*

---

```
R1 LSI 101 {ESR(L,QL,FQ)} ;SERIES RESISTANCE
L1 101 LSO {L} IC={IC} ;SERIES INDUCTANCE
```

```
.ENDS LQS
```

```
.SUBCKT LCHOKE LSI LSO
```

```
+ PARAMS:
```

```
+ L=1U
```

```
+ QL=300
```

```
+ FQ=60MEG
```

```
+ RDC=1M
```

```
+ IC=0
```

```
.PARAM:
```

```
+ PI=3.1416
```

```
+ OMEGA_0={2*PI*FQ/100}
```

```
.FUNC ESR(L,QL,FQ) {2*PI*FQ*L/QL}
```

```
*DC RESISTANCE AND BYPASS CAPACITOR
```

```
RDC LSI 101 {RDC} ;DC RESISTANCE
```

```
CBP LSI 101 {1/(RDC*OMEGA_0)} IC={IC};BYPASS CAP
```

```
*AC RESISTANCE AND BYPASS INDUCTOR
```

```
RAC 101 102 {ESR(L,QL,FQ)} ;AC RESISTANCE
```

```
LBP 101 102 {ESR(L,QL,FQ)/OMEGA_0} IC={IC}
```

```
L1 102 LSO {L} IC={IC} ;CHOKE INDUCTANCE
```

```
.ENDS LCHOKE
```

```
.SUBCKT CQS CSP CSN
```

```
+ PARAMS:
```

```
+ C=1U
```

```
+ QC=10K
```

```
+ FQ=60MEG
```

```

+ IC=0

.PARAM PI=3.1416

.FUNC ESR(C,QC,FQ) {1/(2*PI*FQ*C*QC)}

C1 CSP 101 {C} IC={IC} ;SERIES RESISTANCE
R1 101 CSN {ESR(C,QC,FQ)} ;SERIES CAPACITANCE

.ENDS CQS

*****CLASSE.LIB*****

*****MOSNL1.LIB*****

.SUBCKT MOSFETNLC GATE DRAIN SOURCE
+ PARAMS:
+ RDSON=0.04
+ RG=0.3
+ CGS=1750P
+ RCOUT=0.08
+ RSHUNT=12MEG
+ CJO=1450P
+ VJ=0.818366
+ M=0.5049
+ LDRAIN = 1p
+ LSOURCE = 1p
+ LGATE = 1p
+ CRSS = 10p

LDRAIN DRAIN DRAINL {LDRAIN}
RSHUNT DRAINL SOURCEL {RSHUNT}
LSOURCE SOURCEL SOURCE {LSOURCE}

SW DRAINL SOURCEL GMAIN SOURCE SWIDEAL
.MODEL SWIDEAL VSWITCH (RON={RDSON} ROFF=1MEG VON=2.5 VOFF=1.5); ILIMIT=50)

```

## *SPICE DECKS AND COMPONENT VALUES*

---

```
DSWITCH N101 DRAINL DIODE
.model DIODE D (CJO = 185.52p, VJ = 0.16803565837623,
+ M = 0.22055813533587, TT = 0)
```

```
RCOUT N101 SOURCEL {RCOUT}
```

```
LGATE GATE GATEL {LGATE} ;RSER=10m RPAR=1MEG
RG GATEL GMAIN {RG}
CGS GMAIN SOURCEL {CGS} ;RSER=10m RPAR=1MEG
*RRSS DRAINL DRAINR 10
CRSS DRAINL GMAIN {CRSS} ;RSER=10m RPAR=1MEG
```

```
.ENDS
```

```
*****MOSNL1.LIB*****
```

*Appendix B*

# *PCB Layout Masks and Schematics*

---

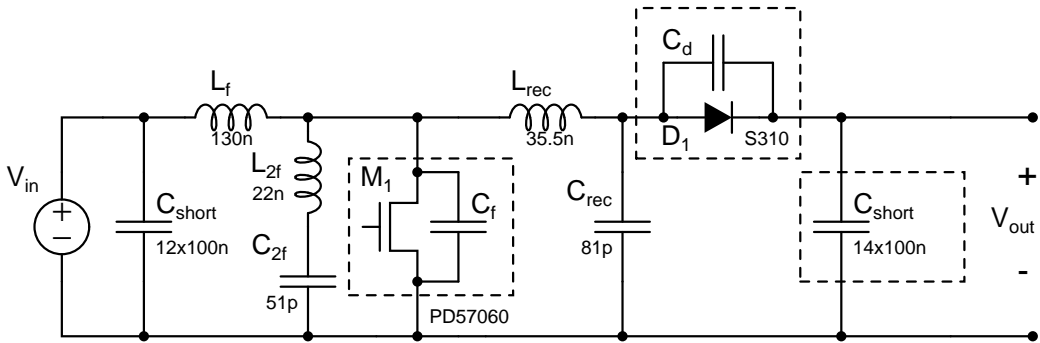


Figure B.1: Final schematic of  $\Phi_2$  converter implemented with ST PD57060.

Component	Value	Package	Part No.	Manufacturer
$L_F$	$130nH$	Coilcraft	132-11SM L	Coilcraft
$C_F$	junction cap	N/A	N/A	ST Microelectronics
$L_{2F}$	$22nH$	Coilcraft	B07T L	Coilcraft
$C_{2F}$	$51pF$	0805	MC08FA510J	Cornell Dubilier
$L_{REC}$	$35.5nH$	Coilcraft	B09T L	Coilcraft
$C_{REC}$	$81pF$	0805	MC08FA820J	Cornell Dubilier
$C_{SHORT}$	$100nF$	0805	C0805C104M5RACTU	Kemet
$D_1$	100V, 3A	SMC	S310	Fairchild
$M_1$	70V $V_{(BR)DSS}$	POWERSO-10RF	ST PD57060	ST Microelectronics

Table B.1: Component values and part numbers for ST-based  $\Phi_2$  boost converter

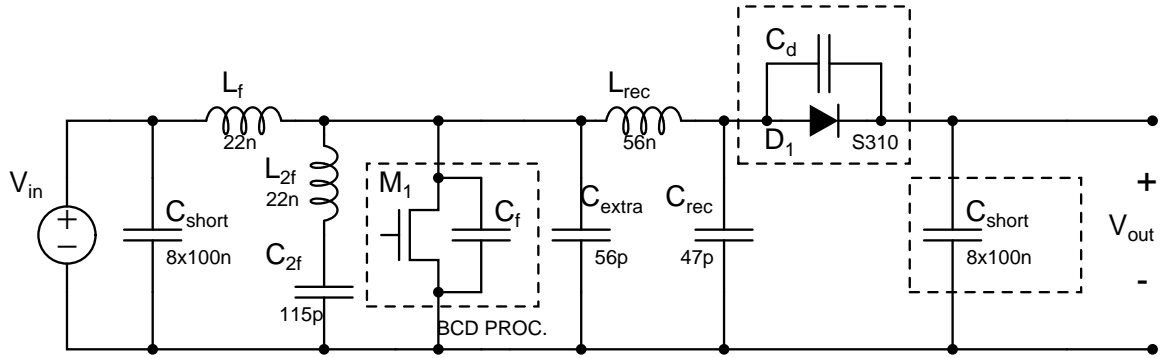


Figure B.2: Final schematic of  $\Phi_2$  inverter implemented with the integrated power process device.

Component	Value	Package	Part No.	Manufacturer
$L_F$	$22nH$	Coilcraft	B07T L	Coilcraft
$C_F$	$56pF, 150V$	0505	ATC100A560G	ATC
$L_{2F}$	$22nH$	Coilcraft	B07T L	Coilcraft
$C_{2F}$	$115pF$	2x 0505	ATC100A(101G/150G)	ATC
$L_{REC}$	$56nH$	Coilcraft	1812SMS-56N L	Coilcraft
$C_{REC}$	$47pF$	0505	ATC100A470G	ATC
$C_{SHORT}$	$100nF$	0805	C0805C104M5RACTU	Kemet
$D_1$	100V, 3A	SMC	S310	Fairchild
$M_1$	50V $V_{(BR)DSS}$	TSSOP-20	2	N/A

Table B.2: Component values and part numbers for Custom-MOSFET-based  $\Phi_2$  boost converter



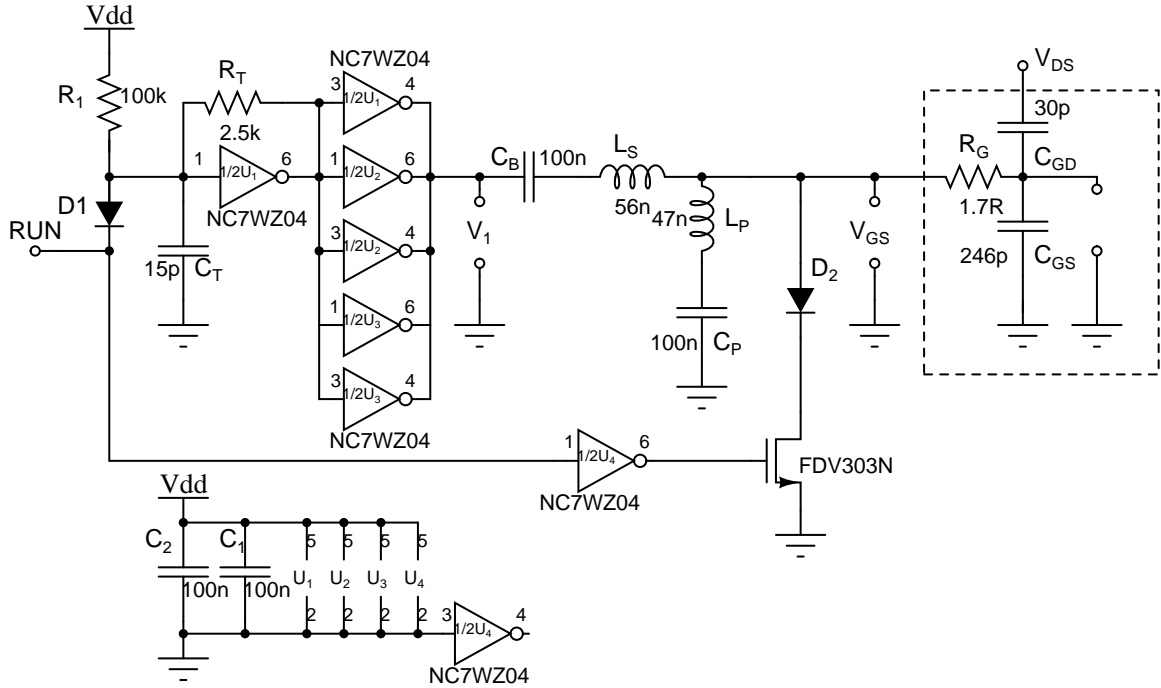


Figure B.3: Complete gate drive schematic.

Component	Value	Package	Part No.	Manufacturer
$U_1-U_4$	CMOS inverter	SC70-6	NC7WZ04	Fairchild
$D_1, D_2$	20V, 100mA	SSSMINI2	MA27D27	Panasonic
$M_1$	25V, 680mA	SOT-23	FDV303N	Fairchild
$C_{1,2,B,P}$	100nF	0603	UMK107BJ104KA-T	Taiyo Yuden
$C_T$	15p	0402	C1005C0G1H150J	TDK
$L_S$	56nH	0603	0603CS-56NG L	Coilcraft
$L_P$	47nH	0603	0603CS-47NG L	Coilcraft
$R_T$	2.5k $\Omega$	0402	Q230182	Panasonic
$R_1$	100k $\Omega$	0402	Q230182	Panasonic

Table B.3: Component values and part numbers for gate drive circuit

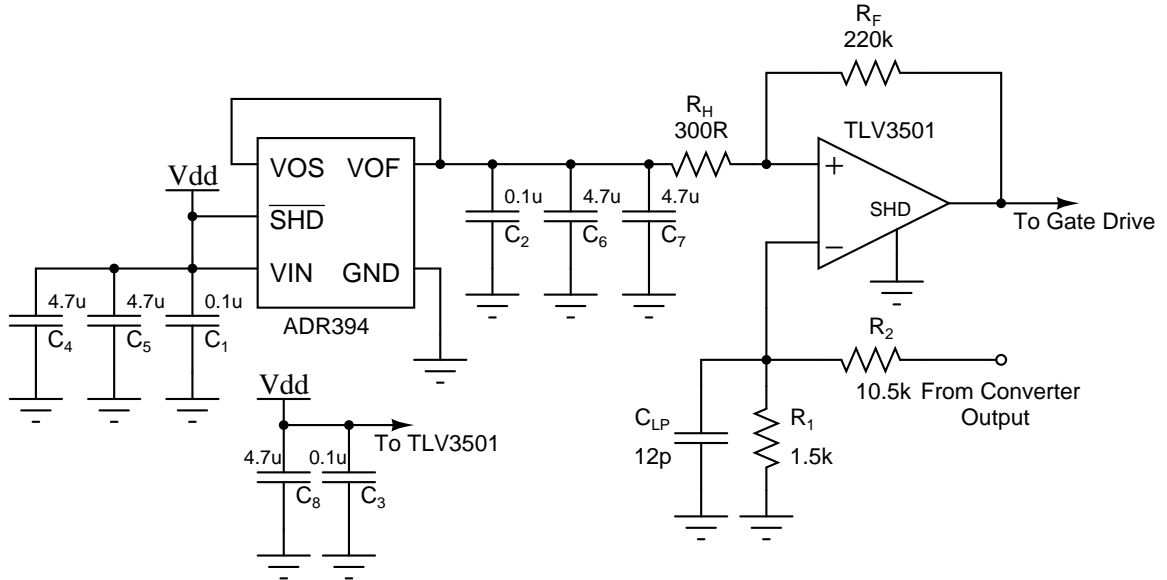
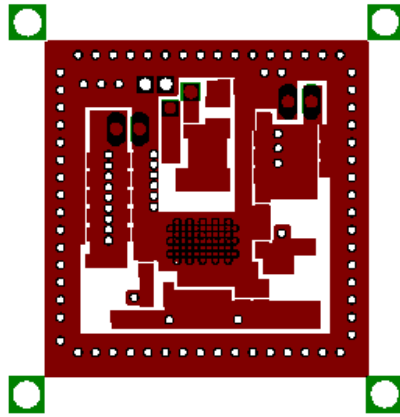


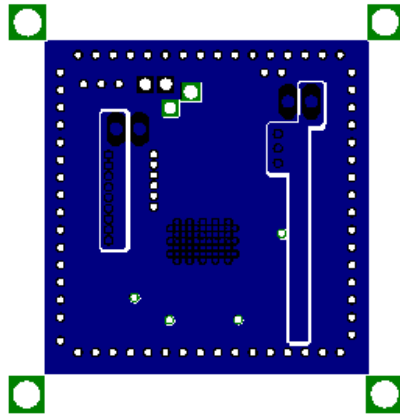
Figure B.4: Complete controller schematic

Component	Value	Package	Part No.	Manufacturer
$U_1$	4.096V ref	5-lead TSOT	ADR392	Analog Devices
$U_2$	4.5ns comp	6SOT-23	TLV3501	Texas Instruments
$C_{1,2,3}$	100nF	0603	UMK107BJ104KA-T	Taiyo Yuden
$C_{4,5,6,7,8}$	4.7u	0603	C1608X5R0J475M	TDK
$C_{LP}$	12pF	0402	C1005C0G1H120J	TDK
$R_F$	220k $\Omega$	0402	Q230182	Panasonic
$R_H$	300 $\Omega$	0402	Q230182	Panasonic
$R_1$	1.5k $\Omega$	0402	Q230182	Panasonic
$R_2$	10.5k $\Omega$	0402	Q230182	Panasonic

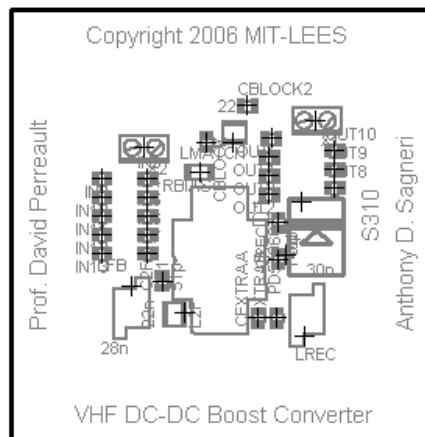
Table B.4: Component values and part numbers for controller circuit



(a) ST Top copper

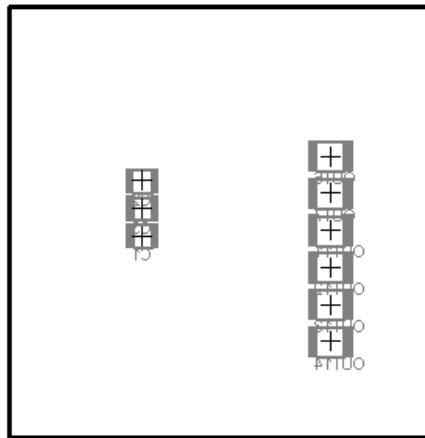


(b) ST Bottom copper

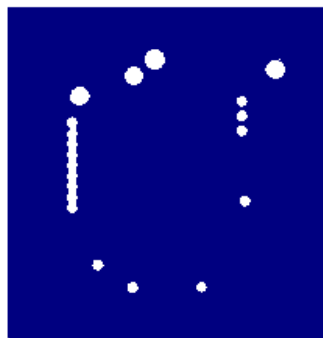


(c) ST Top silkscreen

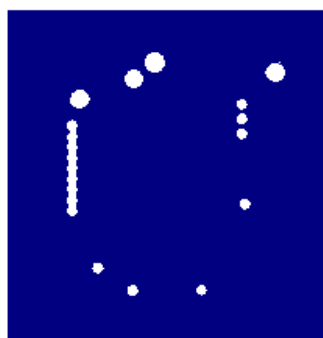
Figure B.5: ST board layout masks



(a) ST bottom silkscreen

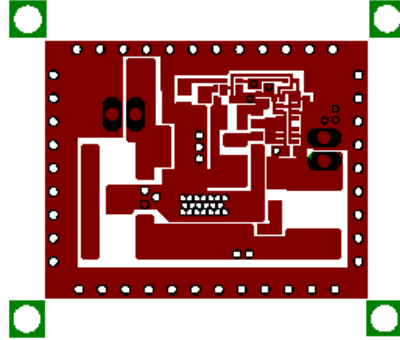


(b) ST Route2

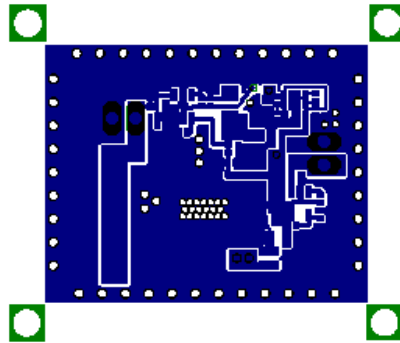


(c) ST Route3

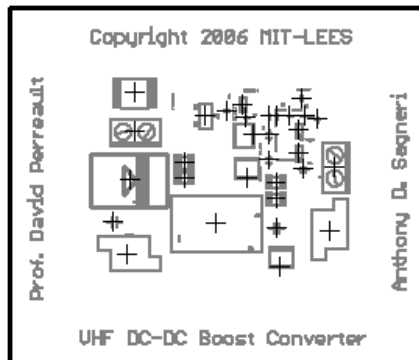
Figure B.6: **ST board** layout masks



(a) BCD Top copper

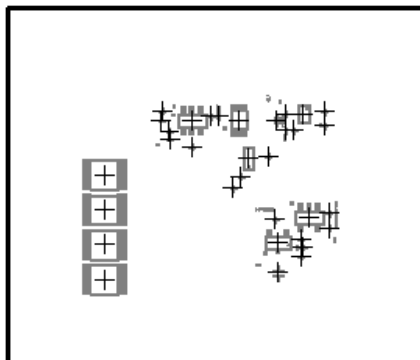


(b) BCD Bottom copper

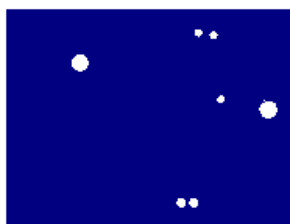


(c) BCD Top silkscreen

Figure B.7: BCD board layout masks



(a) BCD Bottom silkscreen



(b) BCD Route2



(c) BCD Route3

Figure B.8: BCD board layout masks

# Bibliography

---

- [1] J.G. Kassakian, M.F. Schlecht, and G.C. Verghese. *Principles of Power Electronics*. (Addison-Wesley), NY, 1991.
- [2] Joshua W. Phinney. *Multi-resonant Passive Components for Power Conversion*. Ph.D. Thesis, Dept. of Electrical Engineering and Computer Science, Massachusetts Institute of Technology, Cambridge, MA., June 2005.
- [3] Francis Grover. *Inductance Calculations*. New York: Dover, 1946.
- [4] *Improved Calculation of Core Loss with Nonsinusoidal Waveforms*, 4 Oct 2001.
- [5] Duncan A. Grant and John Gowar. *Power Mosfets: Theory and Applications*. John Wiley & Sons, 1989.
- [6] Joshua W. Phinney. Filters with active tuning for power applications. Master's thesis, Massachusetts Institute of Technology, 2001.
- [7] N.O. Sokal and A.D. Sokal. Class E—a new class of high-efficiency tuned single-ended switching power amplifiers. *IEEE Journal of Solid-State Circuits*, SC-10(3):168–176, June 1975.
- [8] Nathan O. Sokal. Class-E RF Power Amplifiers. *QEX*, pages 9–20, Jan/Feb 2001.
- [9] R. Redl and N.O. Sokal. A new class-e dc/dc converter family with reduced parts count: Derivation, topologies, and design considerations. In *Technical Papers of the Fourth International High Frequency Power Conversion Conference*, pages 395–415, 1989.
- [10] R. Redl and N.O. Sokal. A 14 MHz 100 Watt class E resonant converter: Principles, design considerations, and measured performance. In *17<sup>th</sup> Annual IEEE Power Electronics Specialists Conference Proceedings*, pages 68–77, June 1986.
- [11] R.J. Gutmann. Application of RF circuit design principles to distributed power converters. *IEEE Transactions on Industrial Electronics and Control Instrumentation*, IEC127(3):156–164, 1980.

## BIBLIOGRAPHY

---

- [12] M. Iwadare, S. Mori, and K. Ikeda. Even harmonic resonant class e tuned power amplifier without rf choke. In *Electronics and Communications in Japan*, volume 79, pages 23–30, Jan. 1996.
- [13] J.J. Jozwik and M.K. Kazimierczuk. Analysis and design of class-edc/dc converter. *Industrial Electronics, IEEE Transactions on*, 37(2):173–183, April 1990.
- [14] H. Koizumi, Iwadare M., and Mori S. Class  $e^2$  dc/dc converter with second harmonic resonant class e inverter and class e rectifier. In *Thirs Annual Applied Power Electronics Conference Proceedings*, pages 1012–1018, 1994.
- [15] H. Koizumi, H. Sekiya, M. Matsuo, S. Mori, and I. Sasae. Resonant dc/dc converter with class de inverter and class e rectifier using thinned-out method (deleting some of the pulses to the rectifier). *Circuits and Systems I: Fundamental Theory and Applications, IEEE Transactions on [see also Circuits and Systems I: Regular Papers, IEEE Transactions on]*, 48(1):123–126, Jan. 2001.
- [16] Michael J. Chudobiak. The use or parasitic nonlinear capacitors in class e amplifiers. *IEEE Transactions on Circuits and Systems I: Fundamental Theory and Applications*, 41(12):941–944, December 1994.
- [17] J.M. Rivas, J. Shafran, R.S. Wahby, and D.J. Perreault. New architectures for radio-frequency dc/dc power conversion. In *35<sup>th</sup> Annual IEEE Power Electronics Specialists Conference Proceedings*, pages 4074–4084, June 2004.
- [18] J.M. Rivas, R.S. Wahby, J.S. Shafran, and D.J. Perreault. New architectures for radio-frequency dc/dc power conversion. In *Power Electronics Specialists Conference, 2004. PESC 04. 2004 IEEE 35th Annual*, volume 5, pages 4074–4084 Vol.5, 20–25 June 2004.
- [19] Juan M. Rivas. *Radio Frequency dc-dc Power Conversion*. PhD thesis, Massachusetts Institute of Technology, September 2006.
- [20] Thomas H. Lee. *The Design of CMOS Radio-Frequency Integrated Circuits*. (Cambridge University Press), Cambridge, UK, second edition edition, 2004.
- [21] T.H. Lee. *Planar Microwave Engineering*. (Cambridge University Press), 2004.
- [22] F.H. Raab. Maximum efficiency and output of class-f power amplifiers. *Microwave Theory and Techniques, IEEE Transactions on*, 49(6):1162–1166, June 2001.
- [23] F.H. Raab. Class-f power amplifiers with maximally flat waveforms. *Microwave Theory and Techniques, IEEE Transactions on*, 45(11):2007–2012, Nov. 1997.



- [24] J.W. Phinney, D.J. Perreault, and J.H. Lang. Radio-frequency inverters with transmission-line input networks. In *Power Electronics Specialists Conference, 2006. PESC '06. 37th IEEE*, pages 1–9, 18-22 June 2006.
- [25] David C. Hamill. Class DE inverters and rectifiers for DC-DC conversion. In *27<sup>th</sup> Annual IEEE Power Electronics Specialists Conference Proceedings*, pages 854–860, June 1996.
- [26] David A. Jackson. Design and characterization of a radio-frequency dc/dc power converter. M. Eng., Dept. of Electrical Engineering and Computer Science, Massachusetts Institute of Technology, Cambridge, MA., June 2005.
- [27] M.K. Kazimierczuk, B. Tomescu, and A. Ivascu. Class e resonant rectifier with a series capacitor. *Circuits and Systems I: Fundamental Theory and Applications, IEEE Transactions on [see also Circuits and Systems I: Regular Papers, IEEE Transactions on]*, 41(12):885–890, Dec. 1994.
- [28] W.A. Nitz, W.C. Bowman, F.T. Dickens, F.M. Magalhaes, W. Strauss, W.B. Suiter, and N.G. Zeisse. A new family of resonant rectifier circuits for high frequency DC-DC converter applications. In *Third Annual Applied Power Electronics Conference Proceedings*, pages 12–22, 1988.
- [29] M.S. Nakhla and J. Vlach. A piecewise harmonic balance technique for determination of periodic response of nonlinear systems. *IEEE Transactions on Power Electronics*, CAS-23, No.2:85–91, 1976.
- [30] J.M. Rivas, D. Jackson, O. Leitermann, A.D. Sagneri, Yehui Han, and D.J. Perreault. Design considerations for very high frequency dc-dc converters. In *Power Electronics Specialists Conference, 2006. PESC '06. 37th IEEE*, pages 1–11, 18-22 June 2006.
- [31] D. J. Perreault. Evaluation of MOS Transistors for Very High Frequency Power Conversion. *Internal Memorandum*, Laboratory for Electromagnetic and Electronic Systems, Massachusetts Institute of Technology, June 2005.
- [32] James Warren, III. Cell-modulated resonant dc/dc power converter. M. Eng. Thesis, Dept. of Electrical Engineering and Computer Science, Massachusetts Institute of Technology, Cambridge, MA., August 2005.